The Pennsylvania State University

The Graduate School

DEVELOPMENT OF AN ACOUSTIC PREDICTION SYSTEM FOR CONCEPTUAL DESIGN AND ANALYSIS OF ROTORCRAFT

A Thesis in

Aerospace Engineering

by

Thomas Jaworski

Submitted in Partial Fulfillment
of the Requirements
for the Degree of

Master of Science

December 2020

The thesis of Thomas Jaworski was reviewed and approved by the following:

Kenneth S. Brentner
Professor of Aerospace Engineering
Thesis Advisor

Eric Greenwood
Professor of Aerospace Engineering

Amy R. Pritchett
Professor of Aerospace Engineering
Department Head of Aerospace Engineering

ABSTRACT

This thesis describes the development of a noise prediction system (NPS) for conceptual design of rotorcraft. The system is designed to model five noise sources: loading noise, thickness noise, high-speed-impulsive noise, broadband noise, and blade-vortex interaction noise in a manner that is consistent with computational design. The system is composed of four main parts: 1) The conceptual design software NASA Design and Analysis of Rotorcraft (NDARC) that will supply all necessary flight conditions, as well as aircraft configurations and parameters; 2) WOPIt the intermediate tool that will read NDARC's aircraft data, then model blade loading, wake geometry, and unsteady interactions; 3) The acoustic prediction tool PSU-WOPWOP; and 4) A post-processing tool ShearIt that mimics the nonlinear effects of high-speed-impulsive noise. Models were implemented for each noise source to provide accurate enough noise prediction for a conceptual designer while remaining simple enough that computation time is low.

To model thickness noise, the dual-compact loading model is used. By superimposing a pressure distribution on two compact lines, the thickness noise can be modeled without the need for blade geometry details. To calculate blade loading, a blade element theory model was implemented using the compact lifting line assumption. A three-step trim algorithm is used to ensure that each rotor matches the flight conditions. The Beddoes wake model is used to model the wake geometry trailing behind each rotor. The wake is represented by tip-vortex geometry that is discretized along a three dimensional curve. The Vatistas model is used to calculate the unsteady influence on the blade caused by the wake. The semi-empirical Pegg model is used to calculate broadband noise. Acoustic pressure signals are post-processed using empirical relations to mimic the effects of nonlinear propagation. Acoustic theory for each noise source is discussed in detail. The development, theory, validation, and results for each noise source model implemented into the NPS are explored.

Table of Contents

LIST OF FIGURES

LIST OF TABLES

LIST OF SYMBOLS AND ABBREVIATIONS

English Symbols

A, B, C, D	Wake skew parameters
A_b	Blade area (m^2)
AMP	HSI amplification factor
c	Speed of sound (m/s)
c	Chord (m)
C_L	Coefficient of lift
C_T	Thrust force coefficient
C_d	Section coefficient of drag
F_x, F_y, F_z	Forces acting on a blade element (N)
f	Implicit function defining the acoustic data surface ($f = 0$) in the FW-H equation
$H(s)$	Heaviside function
M	Mach number
M_r	Mach number in radiation direction of the observer, $\vec{M} \cdot \hat{r}$
M_x, M_y, M_z	Moments acting on rotor (Nm)
p'	Acoustic pressure (Pa)
R	Rotor radius (m)
r	Radiation distance to the observer (m)
r	Non-dimensional spanwise location
T, H, Y	Rotor thrust force, side force, drag force (N)
t	Observer time (s)
U_P, U_T	Velocity parallel/perpendicular to the rotor plane (m/s)
V_{ind}	Induced velocity on blade segment (m/s)
V_{tip}	Rotor tip speed (m/s)
r_c	Vortex core size (m)
r_r	Non-dimensional tip vortex rollup radius
r_v	Non-dimensional radial location of vortex element
$\vec{x}$	Observer position vector
$\tilde{x}, \tilde{y}, \tilde{z}$	Non-dimensional tip-vortex geometry location

Greek Symbols

α_{eff}	Effective angle of attack (rad)
γ_s	HSI shear angle (rad)
$\theta_0, \theta_{1s}, \theta_{1c}$	Control variables (collective, lateral, and longitudinal cyclic pitch) (rad)
θ_{tw}	Blade twist (rad)

λ_0	Mean induced inflow
λ_c	Climb inflow
λ_i	Induced inflow ratio
μ_x, μ_z	Advance ratio parallel/perpendicular to rotor plane
ρ_0	Density (kg/m^3)
ψ_v, ψ_b	Tip-vortex angle, blade angle
Γ	Circulation strength (m^2/s)
Ω	Rotor rotation speed (rad/s)
β	Blade flapping angle (rad)
$\delta()$	Dirac delta function
δt	Sheared time (s)
τ	Observer time (s)
χ	Wake skew angle (rad)
ψ	Azimuth angle (rad)
ϕ	Wake age (rad)

Other Symbols

$\bar{\Box}^2$	Wave operator $\bar{\Box}^2 = \frac{1}{c^2}\frac{\partial^2}{\partial t^2} - \nabla^2$

Abbreviations

BET	Blade element theory
BVI	Blade-vortex interaction
BVISPL	BVI sound pressure level
BWI	Blade-wake interaction
CFD	Computational fluid dynamics
dB, dBA	Decibel, decibel A-weighting
DEP	Distributed electric propulsion
eVTOL	Electric vertical takeoff and landing
FFT	Fast Fourier transform
FW-H	Ffowcs Williams and Hawkings
HAI	Helicopter Association International
HSI	High-speed-impulsive noise
NDARC	NASA Design and Analysis of Rotorcraft
NPS	Noise Prediction System
OASPL	Overall sound pressure level
ROC	Rate of climb (m/s, ft/min)
SPL	Sound pressure level
UAM	Urban air mobility
PSU-WOPWOP	(Not an acronym) acoustic prediction tool created at Penn State University

ACKNOWLEDGEMENTS

First, I would like to thank my labmates Ryan McConnell, Kalki Sharma, Bhaskar Mukherjee, Ted Gan, Mrunali Botre, and Demi Zachos for making long days and late nights of both research work and class work more enjoyable. Having a team of other aeroacousticians (and friends) was a valuable experience at Penn State.

Next, I would like to thank Dr. Eric Greenwood for being a reviewer of this thesis, but also for helping answer technical questions about the project along the way. Finally I would like to thank my adviser Dr. Kenneth Brentner for giving me the opportunity to conduct aeroacoustic research at Penn State University, and for devoting plenty of time to help along every step of the way.

This research was partially funded by the Government under Agreement No. W911W6-17-2-0003. The U.S. Government is authorized to reproduce and distribute reprints for Government purposes notwithstanding any copyright notation thereon.

The views and conclusions contained in this document are those of the authors and should not be interpreted as representing the official policies, either expressed or implied, of the US Army Aviation Development Directorate or the U.S Government.

Chapter 1

Introduction

Rotorcraft are versatile vehicles that can be used for many tasks in both civilian and military missions. After the 1940s large scale commercialization of the helicopter began. Much of their usefulness stems from the ability to hover, and unlike any other aircraft they can quickly maneuver. Rotorcraft can rotate or translate freely in any direction [1]. Helicopters are widely used daily to accomplish many tasks including transportation, emergency response, aerial filming, and military combat.

The conventional helicopter configuration consists of a main rotor that provides lift with a tail rotor rotated 90° out of plane to provide anti-torque. Many unique designs have emerged over time to fulfill different purposes. Tandem configurations use two counter-rotating rotors that are separated from each other and operate approximately in the same plane. The counter-rotation provides anti-torque and negates the need for a tail rotor. Having two rotors increases the disk area and provides additional lift. Coaxial configurations use two rotors stacked on top of each other that rotate about the same hub axis in opposite directions. This configuration can be very compact, because there is no need for a tail rotor, and both rotors are located at the same place on the airframe. Tiltrotor configurations mount rotors at or near wing tips. Tiltrotor rotors transition from lifting rotors tilted up in hover to a propeller position providing thrust for forward flight [2]. In recent times, a new push for innovation of smaller aircraft with many propellers has arisen. These multicopters can be used to solve a wide array of problems. Drones have become a staple in both civilian and commercial life; they are often used for recreational purposes, as well as professional photography and videography. Soon these designs could change the future of personal travel in the form of urban air mobility (UAM). Uber Elevate is a project planning to use eVTOL vehicles that act as reliable transportation across cities. Uber plans to use distributed electric propulsion (DEP) technology to provide lift while being safe, energy efficient, and quiet [3]. Advancements in rotorcraft technology have and will continue to make meaningful changes in society.

Helicopters have very complex rotor systems. The engines, and more importantly, rotor blade motion generates loud noise signals. These loud noise signals can propagate for a long range in many directions. This can be very annoying for observers on the ground, and can even render the vehicle unsuitable to fly in some areas. Rotorcraft cannot benefit from noise reduction technique such as duct liners like some fixed wing aircraft can. This forces a rotorcraft designer to control noise by reducing it directly from the source [4]. For this reason, rotorcraft noise reduction is more challenging than for other aerospace vehicles.

The process of designing a rotorcraft requires tradeoff analysis for vehicle parameters. Cost, weight, performance, among many other things need to be balanced to complete the design. One very important factor that can limit the usability of a rotorcraft is its noise footprint. Because of the high-speed rotating blades, rotorcraft can be very loud and very annoying at both long and short range. As the use of rotorcraft became more common, this became a bigger problem for the public. In the USA, the FAA has strict regulations for how much noise an aircraft can emit at different times and in different places [5]. If the aircraft cannot meet these regulations (e.g., noise certification), then it will not be allowed to fly. Politicians in some cities like New York [6] and London [7] have pushed for strict regulations to helicopter flyovers citing “incessant noise pollution” as a serious community issue. These regulations would limit the use of helicopters in certain areas and times, or even ban them entirely. The Helicopter Association International (HAI) developed a voluntary noise reduction program called Fly Neighborly [5]. This training program teaches pilots noise mitigation techniques that can reduce noise while flying. HAI hopes that these noise abatement procedures can help improve the relationships between communities and helicopter operators. Noise mitigation can also be achieved during the design phase of aircraft development as well. A combination of in-flight techniques, as well as helicopters designed to minimize noise would be ideal for controlling the noise footprint. Many applications, including military missions, would benefit from minimizing the noise created by the vehicle. If new eVTOL technology like is going to make large advancements in personal air travel, the noise must be carefully controlled.

Many studies and experiments have focused on understanding and minimizing the noise output from moving rotor blades. Many advancements have been made in the field of aeroacoustics, and software tools are readily available to predict aircraft noise. However, in the early stages of conceptual design, noise is rarely considered. An early conceptual design often does not have sufficient detail to undergo a detailed analysis, such as using computational fluid dynamics (CFD), to study the noise output. Even if there were sufficient detail for a CFD analysis on the noise, it would not be practical to run detailed CFD analysis for an early design due to computation speed. A designer may run hundreds of conceptual designs through analysis before choosing a few to move forward. If noise output relies on analysis that has a high computation time, it can be a bottle-neck in the conceptual design process. These factors result in a lack of tools that can be used at the conceptual level to study the noise of potential designs.

A tool that can predict noise early in the design stage, even if the results are only reasonable estimates, would be valuable to a designer developing a noise critical aircraft. The ability to predict noise for varying flight conditions and rotor configurations can lead to innovation in many different missions. If noise prediction is present in the design cycle from the very start of the conceptual design process, it will prevent noise from being an afterthought. Rather than mitigate noise on an aircraft that was designed without acoustic consideration, designers can make decisions for each aircraft detail along the way while controlling noise output. Incorporating noise prediction into the early stages of the development process is essential in the development of noise-conscious vehicles.

Thesis Objective

This project aims to provide a validated noise prediction system for conceptual design. The noise prediction system (NPS) was designed with the scope of conceptual design in mind. Because a conceptual designer may want to test a wide variety of early stage designs, computation speed was a key priority. The system was built to provide an accurate estimate of the noise output as quickly as possible. Since the early stage designs may have little detail, simple models were used to calculate the blade loading, wake geometry, blade-vortex interaction (BVI) effects, and high-speed-impulsive (HSI) effects, and noise output. The NPS should be helpful in allowing a designer to narrow down the list of potential designs. This will allow noise output to be present in early stage trade-off analysis. The designs chosen at this stage of development can be followed up with higher fidelity tools to get more accurate acoustic results once more details are known later in the design process.

In 2016 a project was completed by Sharma and Brentner [8-9] at Penn State University that created a Noise Prediction System for conceptual design using aircraft and flight data based on NASA's Design and Analysis of Rotorcraft (NDARC) [10] and noise prediction from PSU-WOPWOP [11]. That project used simple models for loading and thickness noise calculations. This project builds upon that earlier work, and implemented models that allowed more accurate results and wider capabilities. It was important that this iteration of the NPS could incorporate various noise sources into the acoustic prediction. Loading noise, thickness noise, blade-vortex-interaction noise, high-speed-impulsive noise, and broadband noise are discussed in this thesis.

The blade loading model was replaced with a model that could incorporate complex interactions into the calculations. The loading noise model calculates the blade loads at a high resolution using blade element theory and uses a trim model to ensure that the conditions are being satisfied. To model interactions, NPS uses a distorted prescribed wake model to map the geometry of the tip-vortex path behind the rotor. These tip vortices interact with the rotor, and these interactions are included in the blade loading model.

High-speed-impulsive noise is calculated using a post processing model. This ad-hoc model uses the Mach number in the radiation direction to amplify, shear, and shock the signal where necessary. These adjustments mimic the physics of nonlinear propagation to provide a more accurate estimate of the noise output of an aircraft in an HSI condition.

Contributions

The major contributions of this thesis include the implementation of multiple models to calculate impact of different noise sources, as well as adding new output capabilities to the NPS to visualize some of these models. The models introduced into the NPS are:

- **Blade loading and trim model**

  This blade element theory model calculates the loading distribution on a rotor disk. It also trims to match the value of thrust and moments computed in NDARC. This model is built to be adjusted by unsteady interactions

- **Wake modeling**

  The Beddoes wake model is used to map the tip vortex geometry trailing behind the rotor blades as they spin. This geometry is key for blade-vortex-interaction calculation

- **Blade-vortex-interaction modeling**

  The discretized wake segments behind each blade induce a velocity onto the blade. This changes the loading distribution on the blade, and thus affects the loading noise output. The blade loading model accounts for blade-vortex-interactions

- **High-speed-impulsive noise modeling**

  A post-processing model adjusts the noise signal based on the tip speed of the rotor to mimic the effects of nonlinear propagation. This model adjusts the signal for each rotor, allowing for analysis of a full aircraft for many different observer locations

Reader's Guide

This thesis describes the NPS developed for conceptual design. Before the results are discussed, the necessary background is described in detail. First aeroacoustic theory is discussed at length. The Noise Prediction System itself is described in detail as well. Next the models used to calculate each individual noise source are discussed. Finally, the system is demonstrated through a series of mission segments for different aircraft. The organization of this content is as follows:

- Chapter 2 outlines aeroacoustic theory and background. The equations that form the basis of the acoustic prediction are discussed. Each noise source is that is modeled in this project is described.
- Chapter 3 provides background of the noise prediction system. It explains why it was built, and explains each individual piece of the larger system. This chapter will cover the models that were put in place in 2016, as well as the deficiencies that this project has addressed.
- Chapter 4 discusses loading noise modeling at length. It describes the blade loading and trim models that were developed for the NPS. Results from each model are shown, and some validation is discussed as well.
- Chapter 5 discusses the blade-vortex-interaction model. The models used to describe the trailing wake geometry, as well as its impact on the rotor loads are shown. Results from each model are shown as well with a validation case.

- Chapter 6 discusses the development of the high-speed-impulsive noise model. The equations used to post-process the signal are discussed. Results are compared to the CFD data that was used to develop the model.
- Chapter 7 demonstrates the capabilities of the NPS. Multiple NDARC configuration simulations are performed for the same multi-segment mission. The mission segments and acoustic results are discussed. This incorporates all of the noise source models previously discussed.
- Chapter 8 wraps up the thesis with a summary of all of the works discussed. It suggests models that could be used in future work to expand the capabilities of the system.

Chapter 2

Aeroacoustic Theory and Background

Introduction to Acoustic Theory

Aeroacoustics studies the generation and propagation of soundwaves in the atmosphere. The foundation of aeroacoustics can be attributed to Sir James Lighthill. In 1952 he developed a theory that estimates sound radiating from a fluid using the equations of motion of a gas [12]. Lighthill compared the fluctuation of a real fluid with an ideal fluid at rest. By rearranging the conservation of mass and momentum equations, Lighthill was able to describe the fluctuations in a real fluid with an acoustic analogy. This method predicted the noise from fictitious quadrupole sources.

Lighthill's methods were extended to develop the noise prediction that is used today. In 1955 Curle [13] expanded upon Lighthill's work by adding solid boundaries to the medium. This would result in noise being dependent on both dipole and quadrupole sources. In 1969 Ffowcs Williams and Hawkings extended Lighthill's acoustic analogy to work on moving surfaces [14]. The moving surface introduced a third source, the monopole source, caused by the air displaced by the surface in motion. Inclusion of moving surfaces was key in the study of rotorcraft acoustics. Previously jet noise, wings, and other stationary sources like musical instruments were modeled. With the work of Ffowcs Williams and Hawkings, the rotating blades can be modeled as moving surfaces and the noise from rotorcraft can be predicted. Farassat developed an integral form of the Ffowcs Williams and Hawkings (FW-H) equation by neglecting the quadrupole source term [15-19]. This widely used tool is the basis of many acoustic predictions tools currently in use, including PSU-WOPWOP [11], which is used for this project. This section describes the FW-H equation and

Farassat's integral formulation 1A [15] before discussing each individual noise source that results from the monopole, dipole, and quadrupole sources.

Ffowcs Williams and Hawkings Equation

In the study of fluid mechanics, the Navier-Stokes equations are partial differential equations that govern the conservation of momentum of a fluid. They are extensions of the Euler equations to include viscous effects [20]. Combined with the continuity equation for conservation of mass, the FW-H is derived. Ffowcs Williams and Hawkings rearranged the conservation of mass and Navier Stokes equations into an inhomogeneous wave equation. The FW-H may be written as,

$$\bar{\Box}^2 p'(\vec{x}, t) = \frac{\partial}{\partial t}\{\rho_0 v_n \delta(f)\} - \frac{\partial}{\partial x_i}\{P_{ij}\hat{n}_j \delta(f)\} + \frac{\partial^2}{\partial x_i \partial x_j}\{T_{ij} H(f)\} \tag{2.1}$$

where p' is the acoustic pressure and $\vec{x}$ and t are observer location and time, respectively. P_{ij} is the perturbation form of the compressive stress tensor, and $\hat{n}_j$ is a unit normal vector on the surface $f = 0$ pointing towards the fluid. The $P_{ij}\hat{n}_j$ term represents the local force on the fluid applied by the body, ρ_0 is the density of undisturbed air, v_n is the normal velocity of the body defined by $f = 0$, and T_{ij} is the Lighthill stress tensor. The wave operator is defined as $\bar{\Box}^2 = \frac{1}{c^2}\frac{\partial^2}{\partial t^2} - \nabla^2$, and $\delta(f)$ and $H(f)$ are the Dirac delta and Heaviside functions respectively. The FW-H equation is the basis for most aeroacoustic prediction tools. The right-hand side is often divided into 3 parts: a monopole term, a dipole term, and a quadrupole term, as shown in equation 2.1. Each term is responsible for a specific noise source that will be further explored in section 2.2.

Farassat's Formulation 1A

Farassat's Formulation 1A [15] is an integral form of the solution to the FW-H equation that neglects the quadrupole term and is written as

$$p'(\vec{x},t) = p'_T(\vec{x},t) + p'_L(\vec{x},t), \tag{2.2}$$

where p'_T and p'_L are thickness and loading acoustic pressure terms. Thickness noise is defined as

$$4\pi p'_T(\vec{x},t) = \int_{f=0} \left[\frac{\rho_0(\dot{v}_n + v_{\dot{n}})}{r\,|1-M_r|^2}\right]_{ret} dS + \int_{f=0} \left[\frac{\rho_0 v_n\left(r\dot{M}_r + c\left(M_r - M^2\right)\right)}{r^2\,|1-M_r|^3}\right]_{ret} dS\,, \tag{2.3}$$

while loading noise is defined as

$$4\pi p'_L(\vec{x},t) = \frac{1}{c}\int_{f=0} \left[\frac{\dot{\ell}_r}{r\,|1-M_r|^2}\right]_{ret} dS + \int_{f=0} \left[\frac{\ell_r - \ell_M}{r|1-M_r|^2}\right]_{ret} dS + \tag{2.4}$$

$$\frac{1}{c}\int_{f=0} \left[\frac{\ell_r\left(r\dot{M}_r + cM_r - cM^2\right)}{r^2|1-M_r|^3}\right]_{ret} dS.$$

In these equations a dot over a variable represents the source time derivative of that variable, while a subscript of r, n, or M implies the dot product with the radiation, normal, or Mach number vector, respectively. The radiation distance $r = |\vec{x} - \vec{y}|$, is the distance between the source ($\vec{y}$ i.e., the blade) and the receiver (observer or $\vec{x}$). $\vec{M}$ is the Mach number (surface velocity normalized by the speed of sound of the undisturbed fluid), and $\vec{\ell}$ represents the loading per unit area acting on the fluid caused by the surface. The integrands are marked with a subscript "ret" to denote that they are calculated at the retarded time. It takes time for the sound wave to physically travel to the observer, which is taken into account in the retarded time relation:

$$\tau = t - \frac{r}{c_0}. \tag{2.5}$$

The time when the sound was emitted from the source, τ, is calculated by subtracting the time it takes the wave to travel from the source to the observer $\left(\frac{r}{c_0}\right)$ from the desired observer time (reception time) t. As distance increases, the terms that are dependent on 1/r dominate the equation.

These terms are called far-field terms because at large distances the other terms are less important to the equation. The terms have a $\frac{1}{r^2}$ dependency are called near-field terms because they are more important at shorter distances.

Farassat's Formulation 1A describes the pressure fluctuation created by a moving surface. This is the basis for most of the acoustic predictions in this project. The blades are modeled as moving surfaces and PSU-WOPWOP uses Formulation 1A to numerically calculate the acoustic pressure results. The surface is discretized and the resulting noise signal is calculated by summing the value at each portion of the surface evaluated at the proper retarded time. Each term in the FW-H equation results in individual noise sources. The next section describes the theory behind each noise source in detail.

Noise Sources

A rotorcraft generates noise from several components, including the spinning blades, gearbox, engine and transmission. However, the noise generated by the rotors typically dominate the acoustic field; therefore, rotor noise is the sole focus of the NPS developed in this project. There are three source terms in the FW-H equation: the monopole, dipole, and quadrupole sources. Different types of noise can be categorized by which source term in the FW-H equation that is associated with that type of noise. Each noise source typically propagates in a particular direction, as shown in Figure 2.1.

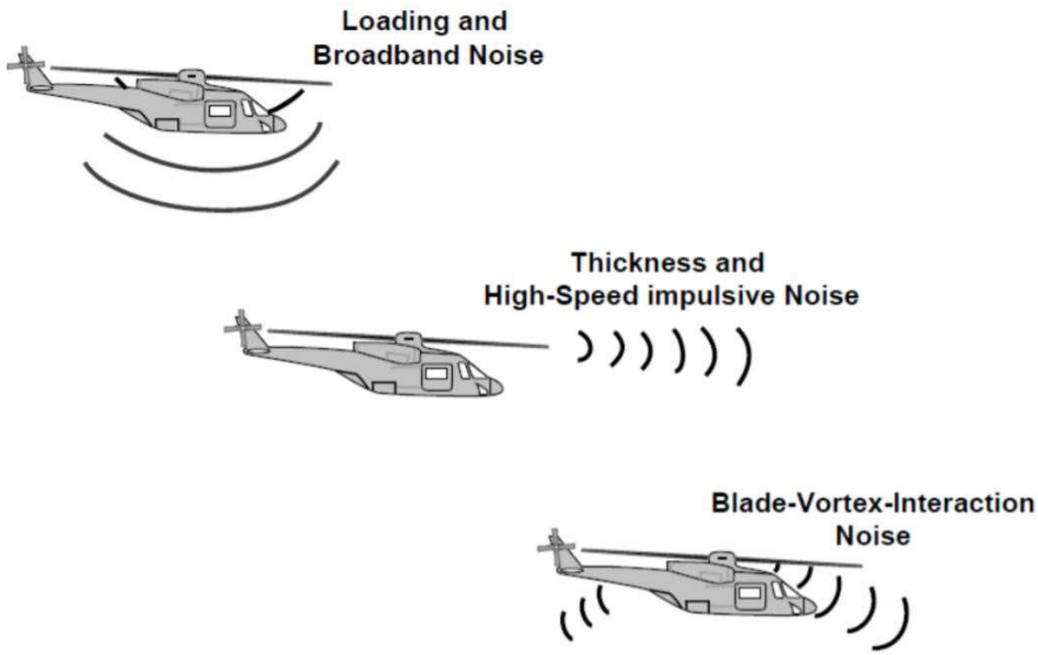

Figure 2.1: Noise propagation directions of different noise sources [4].

Loading Noise

Loading noise originates from the dipole term in the FW-H equation which is the second term on the right side of equation 2.1. Loading noise is created by the airloads on the rotor blades, and the acceleration of the force distribution on the blades. Because the blades are rotating, the force distribution will always be changing direction in an external reference frame fixed to the stationary fluid. This leads to an acceleration term even for the case of a hovering rotor. The acceleration creates a fluctuating pressure signal that propagates away from the blade in the form of loading noise.

Because loading noise is dependent on the blade loading, the noise output is directly proportional to the magnitude and direction of the loads on the blade. The loading vectors normal to the rotor in the thrust direction typically have the highest magnitudes because it acts as the lifting force for the vehicle. Consequently, loading noise is loudest below the plane of the rotor, as seen in Figure 2.1. Loading noise is also dependent on the time rate of change of the blade loads (i.e., the $\dot{\ell}_r$ term). This means that a highly impulsive loading can lead to more severe loading noise than a steady loading, even if the steady loading is at a high magnitude. Unsteady loading is often a result of maneuvers and aerodynamic interactions. Blades interacting with tip vortices can lead to highly impulsive loading which is why blade-vortex-interaction (BVI) noise is a dominant type of loading noise. Turbulent loading is highly unsteady and stochastic, which is why broadband noise is also an important type of loading noise. The term $\frac{1}{1-M_r}$ is the Doppler factor. The loading noise increases as the blade velocity approaches $M_r = 1$.

Thickness Noise

Thickness noise originates from the monopole term in the FW-H equation, which is the first term on the right-hand side of equation 2.1, and originates from the displacement of air due to the blade passage. For this reason, thickness noise is dependent on the size and shape (volume) of the rotor blades, and the blade motion. Equation 2.3 shows that the thickness noise term is proportional to the Mach number in the radiation direction. This means that thickness noise is loudest in the plane of the rotor, in front of the aircraft where M_r and Doppler amplification are the highest. In a hover condition, peak thickness noise is equal for any equidistant observer in the plane of the rotor, because the Mach number in the radiation direction is the same during the peak noise level. In forward flight, the advancing side of the rotor has the highest Mach number for the rotor blade, therefore the maximum thickness noise is found ahead of the helicopter rotor on the advancing side.

Thickness noise is dependent on the amount of air displaced by the blade as it moves through the fluid. Therefore a thicker blade results in a higher noise signal because it displaces more air. Equation 2.3 also shows that thickness noise is dependent on v_n (the local velocity of the blade surface acting in the direction normal to the blade surface). This term is greatest at the leading edge of an airfoil. Both v_n and M_r terms decrease significantly out of the plane of the rotor. Therefore, the major directivity of thickness noise is in the plane of the rotor in front of the aircraft, as shown in Figure 2.1.

Blade-Vortex-Interaction

Blade-vortex-interaction (BVI) noise is highly impulsive, so its presence can drastically increase the overall noise level of a rotor. BVI noise occurs when rotor blades interact with tip vortices that are shed from preceding blades. A blade can experience self BVI, where it operates in its own wake, or it can be influenced from the wake shed from another blade, or wakes shed from an upstream rotor.

Blade-vortex interactions are not present in all flight conditions. Some conditions have little to no interactions with the wake at all. In hover, for example, the wake is convected directly below the rotor and never interferes with subsequent rotor blades. If the advance ratio is very high, there are also less opportunities for interactions, since the helical shape of the wake is more spread out, as shown in Figure 2.2. The most common and impulsive type of BVI found in helicopters is when the helicopter is operating in a moderate speed descent (e.g., 6° descent). This is often a "sweet spot" for the rotor to operate entirely in its own wake. This condition sees many interactions on the blades, which leads to a very dominant impact on the total noise. Figure 2.3 shows a model of the trailing tip vortex geometry behind a helicopter rotor for several descent conditions. In this case, a 6° descent brings the tip-vortices closest to the rotor blades. This increases the number of possible interactions, and the magnitude of these blade-vortex interactions. In forward flight the wake travels below the rotor and does not interact with the blade. In a 6° descent the tip-vortices are pulled into the rotor disk, leading to many unsteady interactions. When the rotor is descending at a steeper angle, the tip vortices travel above the rotor and do not interact with the rotor blades. BVI noise tends to propagate forward and below the rotor for and advancing-side interaction, and rearward and below the rotor for a retreating-side interaction, as seen in Figure 2.1. The annoyance caused by BVI is significant because it is a very loud impulsive sound that is strongest where observers tend to be on the ground.

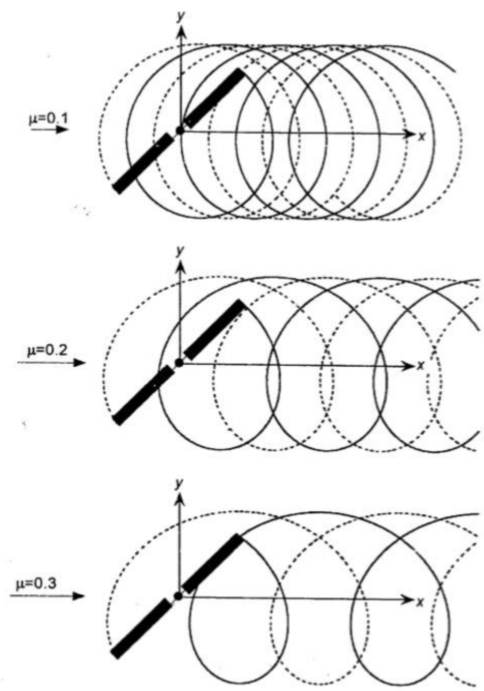

Figure 2.2: Top-view of trailing tip vortices for rotors at varying advance ratios [1].

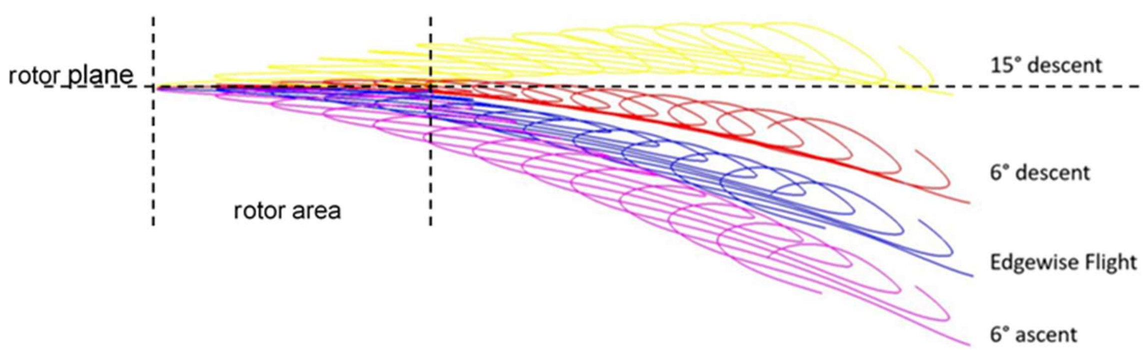

Figure 2.3: Side-view of trailing tip vortices for a rotor at varying descent conditions.

As a rotating blade moves through the air, a wake is shed behind it. High velocity flow moves around the blade and rolls up to produce a vortex at the trailing edge of the blade tip. The tip of the blade has a high pressure difference, so the vortices have high circulation around tight viscous cores [1]. These vortices are inherently three dimensional due to the rapid rotation. When a blade gets close to these vortices, a velocity is induced on it. This induced velocity directly affects the loading along the blade. Because the BVI creates rapid changes in the blade loading, it has a significant impact on the loading noise through the dipole term in the FW-H equation.

The impact of the interaction depends on multiple factors including the strength of the tip vortex and the distance between it and the blade. The strength of the vortex is dependent on the angular velocity, or vorticity, that the fluid particles have. A vortex with high angular momentum will produce a larger influence on the blade. The strength of the vortices diminishes with time (often called wake age), so the longer it takes a vortex to reach the blade, the less impactful it will be. Finally, the distance to the blade, or miss distance, is very important because the induced velocity is inversely proportional to the miss distance [21]. The tangential velocity is strongest at the edge of the vortex core, and diminishes with distance. The miss distance is a three dimensional quantity, so if the vortex is far enough away from the blade in any direction, the resulting induced velocity could be negligible.

Highly impulsive changes in loading due to wake interactions cause the most drastic changes to noise output. Very rapid changes in loading in a short period of time lead to the most annoying noise outputs. When the blade and the tip vortex interact in a near parallel manner, BVI is the strongest. This is because as the blade passes over the tip-vortex, the interaction occurs over the length of the entire blade span in an instant, which is highly impulsive. Figure 2.4 shows a comparison between a parallel interaction and an oblique interaction that is less impulsive. Oblique interactions are less impulsive interactions because as the blade rotates, the interaction occurs over a longer period of time.

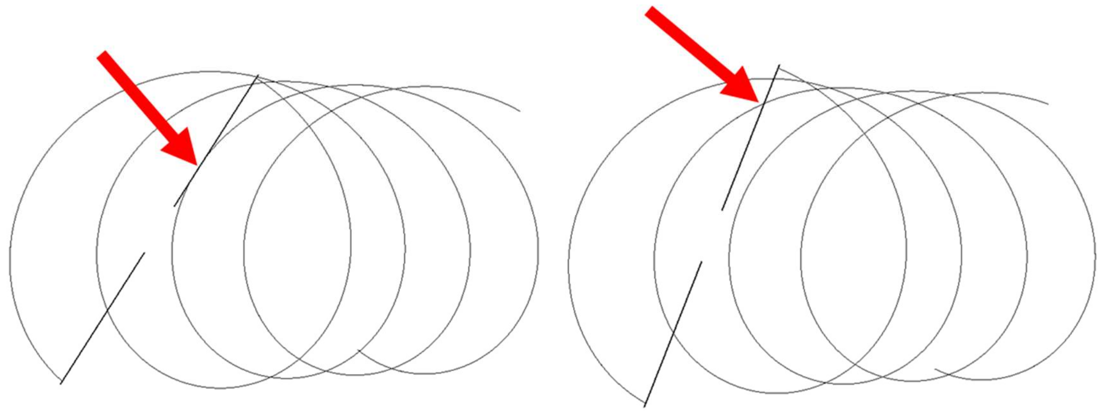

Figure 2.4: Comparison of a rotor experiencing a parallel interaction (left) with an oblique interaction (right).

High-Speed-Impulsive Noise

High-Speed-Impulsive (HSI) noise is a dominant noise source that occurs when the blades are operating in the transonic regime. When it occurs, HSI noise is a very loud and annoying noise source. Rotor tip speeds in the transonic regime can produce shockwaves in the flow around the rotor which can drastically affect the overall noise output of the aircraft. The quadrupole source in the FW-H equation account for these nonlinearities near the rotor blade. Lighthill [12] describes these nonlinearities as: 1) a non-constant local speed of sound due to particle acceleration; and 2) changes in the velocity of sound propagation velocity due to particle velocity near the blade [22]. HSI signals often have visible shocks and wave steepening. The signals have much higher peak amplitudes, and the shockwaves lead to a saw-tooth shaped acoustic pressure time history. These impulsive signals lead to an increased magnitude of noise output.

HSI noise is calculated by the quadrupole term in the FW-H equation. However, the quadrupole is a volume source term, which is more computationally expensive. Computational Fluid Dynamics (CFD) software is often used to provide the input for the quadrupole. To accurately model HSI effects, the quadrupole source needs to be modeled all the way to the observer location to compute the nonlinear propagation effects. Thus it is often very computationally expensive to predict. This level of complexity is not ideal for this conceptual design level system, so the NPS HSI model will use ad-hoc methods to mimic the nonlinear physics.

Broadband Noise

The previous noise sources are known as deterministic noise sources because they are ultimately determined by external causes without the influence of randomness. Given identical inputs, the system would output exact results. However, broadband noise is a non-deterministic source because it relies on random variables such as turbulence. Broadband noise is especially important when the aircraft is overhead of the observer, as shown in Figure 2.1.

Turbulence interacting with the rotor can come from an outside source such as the atmosphere, upstream wakes, or can come from the blade itself. Blade-self noise occurs when the turbulence is coming from the blade itself. Airfoil self-noise occurs when the airfoil of a blade interacts with the turbulence produced in its own boundary layer [23]. Turbulence arises from vortex shedding, boundary layers, and flow around the trailing edge. External broadband sources are categorized into turbulence ingestion noise, and blade wake interaction (BWI).

When broadband noise occurs, it often generates frequencies that the human ear is most sensitive to (2-5 kHz) [24]. This makes it an important area of study because it can be a very annoying sound for humans to hear. Casper and Farassat [25] derived a second solution to the FW-H equation that can be used to predict broadband noise. However, broadband noise was not a focus for this project, so it will not be discussed in great detail. A semi-empirical model was developed by Pegg [26] to model broadband noise. This broadband noise model included in PSU-WOPWOP is discussed in chapter 3.

Chapter 3

Noise Prediction System Overview

Noise prediction is not routinely available during conceptual design. The noise prediction system (NPS) was originally developed in 2016 to add acoustic prediction capabilities to NASA's conceptual design code NDARC [10]. This project has expanded upon the NPS by replacing models and adding new capabilities to the system. Models for blade loading, blade-vortex interaction (BVI) noise, and high-speed-impulsive (HSI) noise were implemented. This chapter will provide a detailed background of the system that was designed in 2016, and address the deficiencies that led to the new capabilities that this project has added. It also discusses areas that the system could be expanded upon in future work.

NPS is built to provide acoustic prediction to a conceptual design program. At the conceptual design level, many variables that are needed to accurately predict noise are not available. The models included in NPS were chosen to work in a manner that is consistent with conceptual design, but accurate enough to provide a designer with acoustic guidance. The NPS combines conceptual design software with an acoustic prediction tool together with an intermediate program to provide the necessary fidelity for each noise source model and provide the input that is needed for the acoustic prediction tool.

NPS Background

The system is comprised of multiple programs linked together (NDARC, WOPIt, and PSU-WOPWOP). The conceptual rotorcraft designs and flight conditions are provided by NDARC.

PSU-WOPWOP is used to compute the acoustic predictions for these aircraft. WOPIt serves as the intermediate program that performs the calculations needed to provide the sufficient fidelity for each noise source. Each of these components are discussed in detail in the following sections.

The entire system is run sequentially using a single BASH script, for the ease of the user. Figure 3.1 shows the interactions between each piece of the system. The script also moves files, and ensures that inputs are correct, so the user needs only to interact with the NPS input itself. This is by design, so that a user who is not very familiar with any of the individual pieces of the system does not need to learn how to run each part independently (with the possible exception of NDARC). The NPS input utilizes a Fortran namelist file. This file enables the user to control desired outputs, as well as adjust parameters such as resolution and noise sources to analyze.

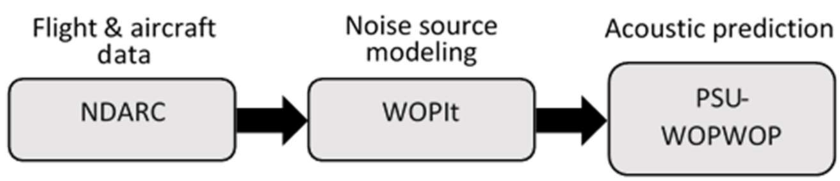

Figure 3.1: Diagram of the programs executed by the Noise Prediction System.

NDARC

The first piece of NPS that is executed is NDARC [10]. NDARC is a standalone code developed by Dr. Wayne Johnson and his team at NASA to analyze generic rotorcraft for conceptual design and technology impact assessments. It can be used to design or size a rotorcraft configuration and then estimate its performance [10]. In addition to using predefined configurations, NDARC can size rotorcraft configurations based on constraints by adjusting the dimensions, power, weight, etc. It can also analyze the performance of an aircraft in off-design missions and flight conditions.

An NDARC mission is split into segments. Each segment can operate a piece of an overall mission in succession such as takeoff, climb, cruise, max speed, descend, and landing. Fuel burn, altitude, and other conditions are correctly transferred from segment to segment. Standalone flight conditions can also be analyzed individually. NDARC can iterate variables to maximize certain characteristics that the user desires. For example, best endurance, best range, best power margin, and maximum climb are all conditions that NDARC can determine for a given flight segment. To reach these conditions, variables such as speed, rate of climb, tip speed, altitude, acceleration, and angular rates can be optimized. For each flight segment, the user can select one condition to maximize and up to two variables to iterate.

NDARC supplies the NPS with the necessary parameters for the conceptual aircraft design including rotor configurations and flight parameters. NDARC outputs a solution file that contains all of the variables used inside that run, which completely defines the aircraft and the operating conditions. WOPIt reads in this solution file and extracts all of the necessary variables from NDARC. Figure 3.2 shows a block diagram for the input that is passed in NDARC, and the output which is passed to WOPIt.

Figure 3.2: Diagram showing the information passed into and out of NDARC.

WOPIt

WOPIt is the second stage of NPS, where the modeling for noise prediction is done. This was designed as the bridge between conceptual design and acoustic prediction. It takes data from

NDARC, and eventually provides the necessary input for PSU-WOPWOP. Before this output can be created, blade geometry and loading data has to be computed. First, it reads the solution file output by NDARC to get all of the necessary information about the aircraft, as well as the flight conditions for each case. It also uses a Fortran namelist that the user inputs into NPS. This input can control which aircrafts, missions, rotors, and noise sources are performed, as well as the desired final output. This namelist is the only input that the user needs to provide to use the system. The system is built with default values for each setting. This offers a balance between giving the user full control over everything they want to model, while also not requiring the user to enter every possible setting, which would make the input too complicated.

Using the information gained from the user and NDARC, WOPIt then models the physics for the rotorcraft necessary to predict the noise. This includes modeling the blade geometry as lifting lines, as well as calculating the blade loading. NPS must be fast so that many conceptual design cases can be executed quickly. But NPS must also have sufficient accuracy to model the critical physics relevant to noise generation so that the noise results give the designer an accurate understanding of the noise generated by the design. To achieve this, simple models are used when appropriate, while extra details are modeled to capture the relevant physics.

One key assumption is the compact loading model [27]. Instead of modeling the blade as a three dimensional grid, WOPIt assumes that the blade is acoustically compact in both the thickness and chordwise directions. The blade is modeled as a lifting line along the quarter-chord. This approach cuts down on computation time significantly by limiting the total number of integration nodes with a very small effect on the overall accuracy. Figure 3.3 shows a comparison between a full blade geometry model and the lifting line model. In this example, the full blade has 17 spanwise stations 36 chordwise stations, resulting in 612 total integration nodes per blade. By comparison, the compact assumption only needs the spanwise nodes so there are only 17, a 97% reduction of integration nodes (and similar reduction in computation time) for the noise prediction alone. WOPIt needs to compute loading at each node, and PSU-WOPWOP needs to compute the acoustic contribution at each node at each point in time. This reduction in total nodes drastically reduces the computational cost. Blade loading is calculated using the loading term in Farassat's formulation 1A; hence, the acoustically compact assumption reduced the surface integral to a line integral.

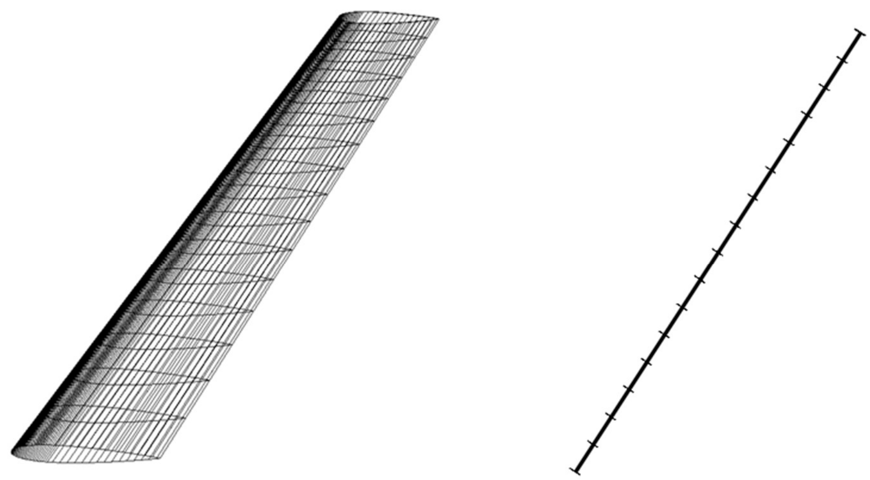

Figure 3.3: Total node comparison for a discretized 3D blade (left) with a 2D lifting line (right).

Typically thickness noise is computed with a surface integral of the thickness term in Farassat's formulation 1A. However, WOPIt uses the dual compact thickness model [28] to reduce the computation cost, similar to the compact assumption used for loading noise. In this model the blade is modeled as two compact lifting lines along the span of the blades. These two lines are typically positioned at 13 percent and 87 percent of the chord, as shown in Figure 3.4. These locations were chosen by an empirical fit used to best match the thickness noise calculated from a full geometric description of the blade [28]. The chordwise locations can be adjusted for a better fit, depending on the blade geometry. This model does not need detailed information about the distributed blade geometry – just the blade chord and the thickness as a function of span. This makes the model ideal for conceptual design because it is much faster than using the full geometry for acoustic prediction.

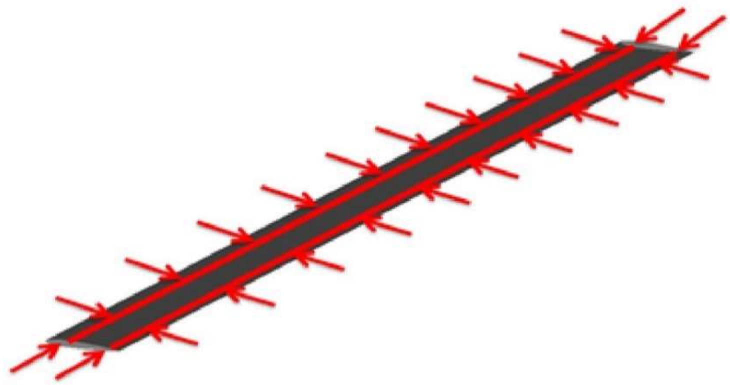

Figure 3.4: Placement of dual compact lifting lines along the blade [9].

This model utilizes Isom's thickness noise calculation. Isom applies a uniform pressure distribution of $\rho_0 c^2$ to a rotor blade and then uses the dipole (loading noise) term to compute thickness noise. This computation is equivalent to the values of traditional thickness noise computation. Therefore, by superimposing a uniform pressure distribution onto two acoustically compact lines, thickness noise can be calculated in the same general manner as loading noise. However, the uniform pressure distribution results in a net force of zero if a single lifting line is used to integrate over the surface. Therefore, to apply Isom's calculation with an acoustically compact assumption, two lifting lines are needed. The blade is divided into two pieces at the chordwise location of maximum thickness. All of the loads that act between the leading edge and the division are superimposed on the first line, while the loads that act between the division and the trailing edge act on the second line. This process is shown in Figure 3.5. The dual compact thickness noise model uses two simple line integrals of equation 2.3 to compute thickness noise with Isom's calculation.

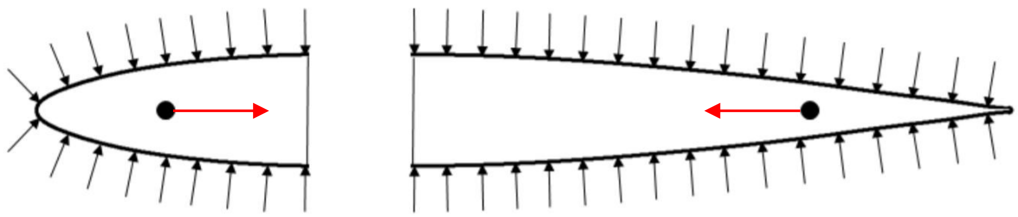

Figure 3.5: Process of superimposing loads around the airfoil onto two compact lifting lines [9].

Once WOPIt is finished modeling all of the noise sources, it creates PSU-WOPWOP input files. Each case gets a namelist that correctly includes the rotors, observers, and acoustic prediction settings from the user's input through the NPS input namelist. It also outputs a file that lists every case that was run in NDARC, as well as the global file path so PSU-WOPWOP can run acoustic prediction for each case.

PSU-WOPWOP

PSU-WOPWOP is a standalone program that was developed at Penn State University. PSU-WOPWOP is widely-used throughout academia, research, and industry for predicting rotorcraft acoustics for many configuration and maneuvers. Students at Penn State University have been heavily involved in its development, and it has been used to complete many research projects. For acoustic pressure time history computations, PSU-WOPWOP uses the Farassat's Formulation 1A [15] that was discussed in chapter 2.

PSU-WOPWOP is executed after WOPIt, and computes all of the acoustic predictions. The user has a wide range of control over the data that PSU-WOPWOP will output. PSU-WOPWOP requires a description of the aircraft, flight data, and observer system used for the acoustic prediction. WOPIt automatically creates all input files needed for PSU-WOPWOP as a part of the NPS run. The observer system (where the noise is computed) can be described as a single point, as a planar grid, or as a spherical grid. These observers can be stationary, moving along as if they are attached to the aircraft, or in some arbitrarily prescribed motion. Figure 3.6 shows a block diagram of the information that is passed to PSU-WOPWOP by WOPIt, and the acoustic prediction output that it provides.

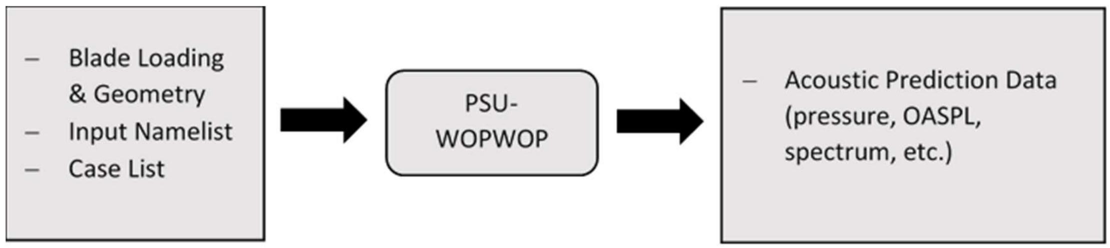

Figure 3.6: Block diagram of information passed into and out of PSU-WOPWOP.

PSU-WOPWOP Models

PSU-WOPWOP has multiple broadband noise models implemented. The simplest and most relevant to the conceptual design of helicopters is the Pegg model [26]. The Pegg model is a semi-empirical model that uses rotor parameters to predict the 1/3rd octave spectrum of the broadband noise. This model uses rotor parameters to predict the broadband noise contribution for each rotor. This model does not need information about each individual blade, except for tip speed. Because of this, it may not be appropriate for rapid maneuvers. Broadband noise is known to be a significant component of helicopter noise for civil noise certification. It tends to be important during flyover and when the helicopter is downrange from the observer - consistent with the fact that broadband noise is a particular type of unsteady loading noise. Using this model has been shown to fill in the missing gaps when modeling broadband noise [29].

The Pegg model calculates broadband noise in four steps. First, the peak broadband frequency is calculated by

$$f_p = -240 \log T + 2.448 V_{tip} + 942 \tag{3.1}$$

where T is the rotor thrust in Newtons and V_{tip} is the hover tip speed in meters per second. Next, the 1/3rd octave band that contains the peak frequency is found. Then, the peak sound pressure level for that octave band is found using

$$SPL_{1/3} = 20 \log \left(\frac{V_{tip}}{c_0}\right)^3 + 10 log \left[\frac{A_b}{r^2} (\cos^2 \theta_{HO} + .1)\right] + S_{1/3} + f(\bar{C}_L) + 130 \tag{3.2}$$

where tip speed is normalized by the speed of sound, A_b is the rotor disk blade area, and θ_{HO} is the angle between the negative thrust axis and the radiation vector that points from the hub to the observer. $S_{1/3}$ is the normalized spectrum function, which is an empirical value dependent on which 1/3rd octave band contained the peak frequency. The lift coefficient is determined by the piecewise function

$$f(\bar{C}_L) = \begin{cases} 10 \log(\bar{C}_L/0.4) & \text{if } \bar{C}_L \leq 0.48 \\ 0.8 + 80 \log(\bar{C}_L/0.48) & \text{if } \bar{C}_L > 0.48 \end{cases} \tag{3.3}$$

where $\bar{C}_L$ is the average blade lift coefficient. Finally, the SPL can be calculated for all other 1/3rd octave bands using the spectrum shape prescribed by Pegg and shown in Figure 3.7. Figure 3.8 shows an example of OASPL calculated for a Bell 430 flyover at 80 knots with and without the broadband model compared to flight test data. The grouping of thin lines is a set of housekeeping runs of a flight test flyover, all at nominally the same flight condition as the prediction. These show the scatter between what is requested and what was actually flown. The thicker lines show the acoustic prediction calculated by NPS. The total noise prediction in the left figure does not include broadband noise, and it under-predicts the OASPL when compared to flight data. The right image shows that when including broadband noise, the peak total noise signal increases by around 5 decibels (dB) and matches the flight test data much more smoothly.

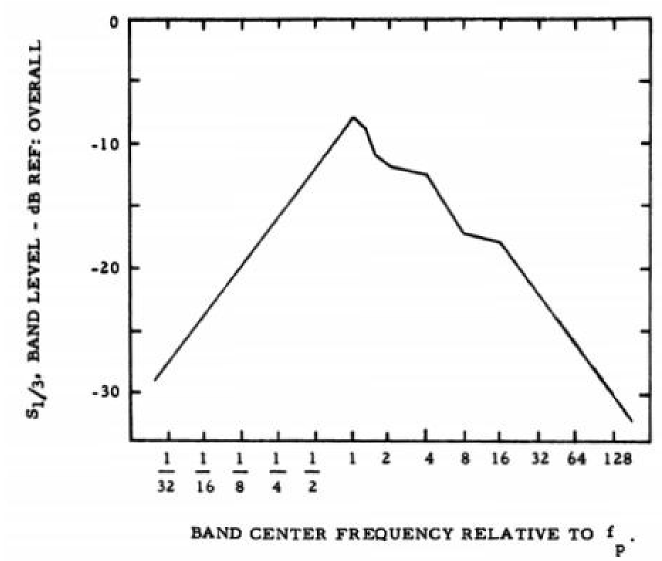

BAND CENTER FREQUENCY, BAND LEVEL

1/32 = -29.0	2 = -11.5
1/16 = -24.5	4 = -12.1
1/8 = -19.5	8 = -16.5
1/4 = -15.3	16 = -17.0
1/2 - -11.7	32 = -21.8
1 = -7.5	64 = -26.4
	128 = -30.0

Figure 3.7: Normalized rotor broadband noise empirically determined spectrum shape [26].

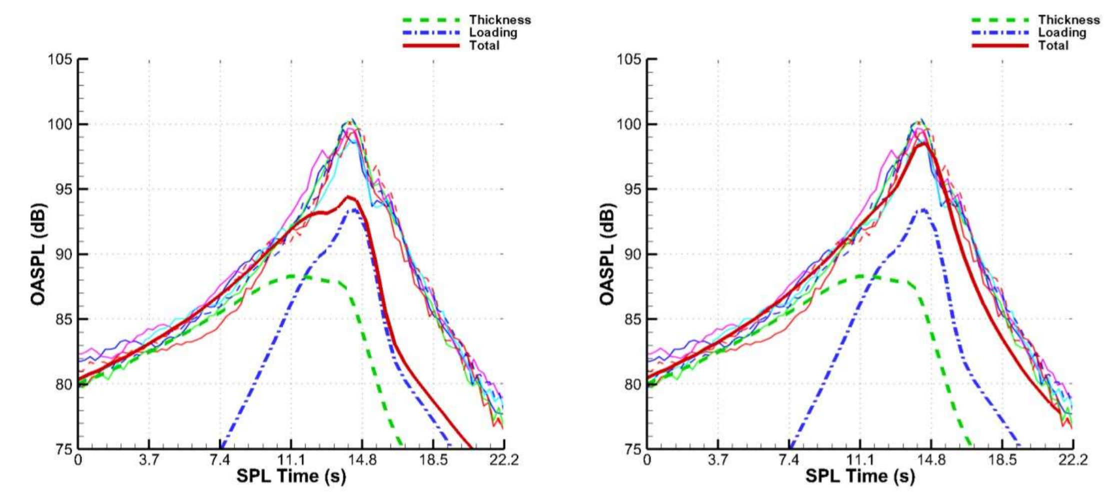

Figure 3.8: Comparison of Overall Sound Pressure Level for a Bell 430 flyover at 80 knots ignoring broadband effects (left) and including broadband effects (right) [9].

As a noise signal propagates across distance it attenuates into the atmosphere. The dissipation can be attributed to viscous losses, heat conduction losses, or losses due to internal molecular processes [24]. Attenuation causes the sound waves to decrease in amplitude over time. PSU-WOPWOP adjusts the dB level of the signal using

$$\Delta dB = -10 \log \mathrm{e}^{2\alpha r} \tag{3.4}$$

where r is the radiation distance and α is the atmospheric attenuation coefficient. The atmospheric attenuation coefficient is determined using the frequency of the signal, the air temperature, relative humidity, and relaxation frequency values of oxygen and nitrogen. The decrease in dB of the signal is converted back into pressure and frequency, resulting in a signal that includes losses caused by dissipation into the atmosphere.

PSU-WOPWOP Output Capabilities

PSU-WOPWOP can output many various acoustic prediction plots including acoustic pressure time history, OASPL, PNL, PNLT, SEL, EPNL, and spectrum data [11]. The user also has the option of using the A-weighted dB scale, including atmospheric attenuation, or applying acoustic filters. The A-weighted dB scale is a weighted curve that represents the loudness of a signal in dBA based on the sensitivities of the human ear. The human ear is most sensitive in the 2-5 kHz range, and unable to detect sounds below 20 Hz or above 20 kHz. The A-weighting scale assigns each frequency a weight based on these ranges, and uses them to compute a modified dB level [24]. This can be very useful when studying annoyance metrics for civilian flights.

Post processing options are also available. These include adding high-pass and low-pass filters to the noise signal. This can be used to isolate certain frequency ranges to study a specific metric. Windowing functions can be applied to address discontinuities at the ends of a data window for acoustic signals that are not periodic at the selected window length. The fast Fourier transform

(FFT) assumes an infinitely repeatable, periodic signal. If the signal is not periodic, a window function can "taper" the ends to zero to ensure that the series will not have any discontinuities.

PSU-WOPWOP also has the capability to output visual debugging plots called sigma surface plots. These present a visual representation of the positioning and motion of rotors and observers. It also allows the user to choose individual variables and vectors that are plotted on the rotor blades. This is very useful to confirm, that the rotor configuration and observers are being modeled correctly and to help diagnose the noise sources. Sigma surface plots are also useful to visualize vector functions (blade loading, blade velocity, M_r, etc.) on rotating blades.

The user does not need to be familiar with all of the capabilities of PSU-WOPWOP to run simple cases. WOPIt creates the input files for PSU-WOPWOP, so an NPS user can control the models, predictions, and outputs performed. Generally a designer will not need to access these input files, but all of the details are accessible if they want to understand what is being performed and explore the noise results.

ShearIt

When HSI noise occurs, it is a very significant source that tends to dominate the noise signal. While it is unadvisable to operate in HSI flight conditions, it is important that the NPS can account for the HSI effects and warn a designer. ShearIt is a post-processing model that modifies the signal from PSU-WOPWOP to mimic the effects of HSI noise. It used uses empirical formulas based on CFD computations [30] that are dependent on the tip Mach number to amplify and shear the entire signal. If this sheared signal becomes triple valued, a shock-fitting algorithm is used to make the acoustic pressure signal single valued with a shock-like jump. Figure 3.9 shows an example of the three steps that ShearIt uses to modify a signal.

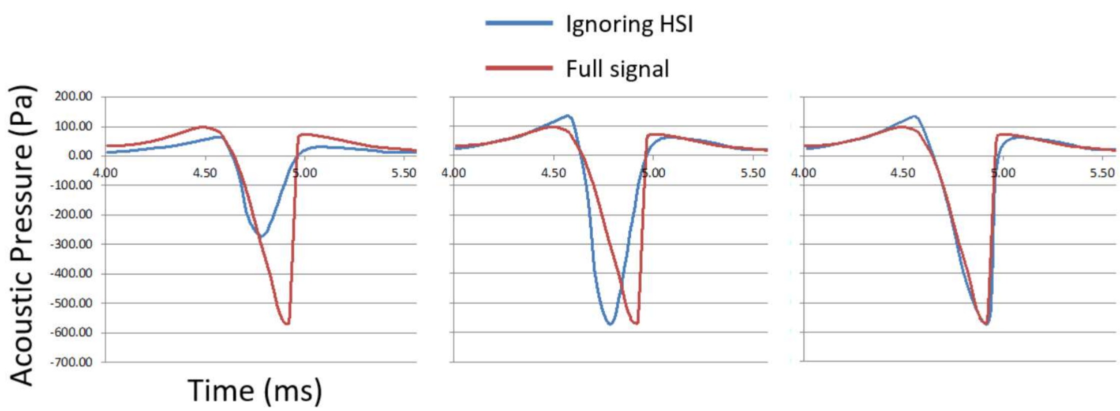

Figure 3.9: The signal adjustment process for HSI post-processing. The original signal (left) is amplified (middle) then sheared (right) to match the full signal.

Post processing was chosen because it is simple and fast. The system does not need to know about the vehicle's specifications or any parameters about the flight condition. No expensive modeling of the flowfield or shockwaves are needed to model the HSI noise with this tool. This is consistent with the level of conceptual design, because many of the parameters are not known. To accurately compute HSI noise, a detailed CFD computation of the flow field is needed. Modeling the transonic flow around the blade and the nonlinear propagation to the observer would require a large CFD computation, which is not consistent with conceptual design. A simple model that mimics the physics is used at a very small computational cost. Even if the results are not perfectly accurate, this is ideal for conceptual design. In the 2016 project, ShearIt was successful as a proof-of-concept for a post processing HSI model. However, it wasn't completed or user friendly, and was never implemented into the NPS. The next section describes the changes that were made to ShearIt in the current model.

Enhancements to the 2016 NPS

This project took full advantage of the work that was completed in 2016, and improved upon the system in many ways. The dual compact thickness noise model, as well as the broadband noise models were untouched, because they were completed in 2016. The noise prediction capabilities were expanded upon with new models in this work. Wake modeling and BVI noise models were developed and added to WOPIt as well. ShearIt was overhauled and included into the NPS. The overall structure of NPS was left relatively unchanged, so user input remained consistent with the conventions of the 2016 NPS. Slight changes were also made to system to fix bugs and increase efficiency and consistency.

Blade Loading and Blade-Vortex Interaction

The blade loading model in 2016 was a simple model. This model was not compatible with unsteady loading caused by interactions. The blade loading model was replaced with a blade element theory (BET) model that is capable of predicting unsteady interactions. This model uses inflow around the azimuth to calculate unsteady blade loads. This model calculates the forces and moments acting on the blades one rotor at a time. The blade loads for each rotor are trimmed to ensure that the calculated loading matches the thrust and moments that were determined for the rotor in NDARC. This ensures that WOPIt is modeling the flight condition the same as NDARC. This trim model is simple and can be applied to each rotor. The inflow, loading, and trim models are all explained in chapter 4.

This project added BVI noise modeling capabilities to NPS. A blade element theory model was chosen because the loads are calculated at each station around the rotor disk. If an interaction changes the inflow at a specific location on the rotor disk, the BET calculation can be adjusted at that station. This capability is necessary to model the unsteady effects caused by interactions. The Beddoes wake model was also added to WOPIt. This maps the geometry of the tip-vortices that trail behind the rotor. The tip-vortices mapped out in this model induce a velocity on the blade as it comes near. This induced velocity increments the blade loading to model BVI noise. The wake model and BVI loading model are described in chapter 5.

WOPIt now has the option to output additional plots if the user desires. These plots help the user visualize the data calculated by the noise source models. Disk plots can plot key blade parameters around the blade azimuth for each rotor including blade loading, moments, induced velocity, and inflow. Tip-vortex plots show the distorted tip-vortex path behind each rotor. These are in plot3D format, and can be animated though time. Configuration plots show the blades and wakes from multiple rotors all in the same file to show the global orientation of the aircraft. Figure 3.10 shows the input and output that is passed through the updated WOPIt.

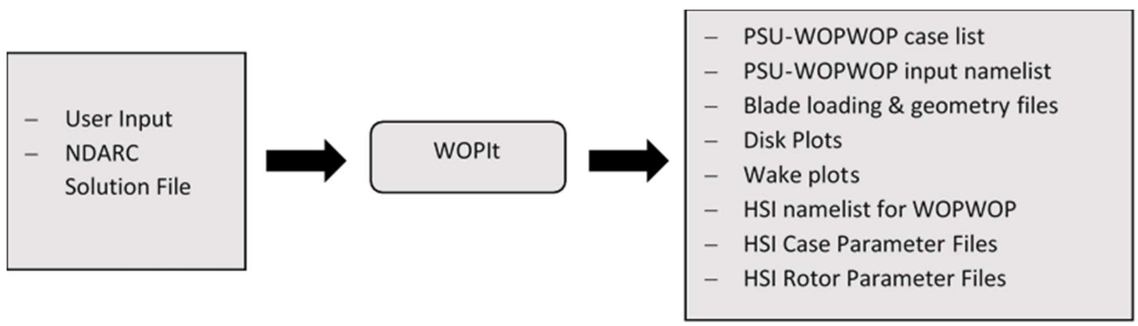

Figure 3.10: Diagram showing the information passed into and out of WOPIt. Files are passed to PSU-WOPWOP, but the user can also output additional plots.

High-Speed-Impulsive Noise Modeling

This project replaced the HSI model that was created in 2016. The old HSI model had limited functionality. It only worked for a single rotor with an observer in the plane of the rotor in front of the aircraft. This proof-of-concept program was not completed, or included in the NPS. The old HSI model was completely re-written to expand upon its capabilities, to provide results that are more accurate and robust, and to optimize its process. ShearIt was built into the NPS, so that all of the necessary input is generated, and ShearIt is executed after PSU-WOPWOP.

The new HSI model uses Mach number in the radiation direction (M_r) of the observer to amplify and shear the signal. This allows the system to predict HSI effects for any observer location. The ad hoc model is described in detail in chapter 6. ShearIt was also redesigned to work for multiple rotors and multiple cases. This allows an entire aircraft's noise signal to be predicted with HSI effects. The new model that ShearIt uses to shear the signal now takes radiation distance into account. This mimics nonlinear propagation on the basis that given a large enough distance, even smaller signals will shock.

PSU-WOPWOP has the capability to read in an acoustic pressure time history and to perform acoustic post-processing, such as OASPL and spectrum computation. ShearIt now produces the necessary input for PSU-WOPWOP to read in the acoustic pressure time history that was amplified, sheared, and shock fit to model HSI noise. This includes a list of all cases, as well as the modified list of acoustic pressure time histories. This allows the HSI effects modeled by ShearIt to be included in the acoustic post-processing capabilities that PSU-WOPWOP can offer.

ShearIt outputs the acoustic pressure time history that now includes HSI noise effects for each case. It also has the capability to output other files if the user wishes. To model HSI noise, the signal is amplified, sheared, and then shocked sequentially. The user can tell ShearIt to output the signal for each step along the way for each rotor. This allows the user to see an amplified signal that has not been sheared, as well as a signal that has been amplified and sheared but has not yet been shock fit. The latter results in the triple-valued signal that curves back on itself as described in chapter 6. Figure 3.11 shows the data that is passed into and out of ShearIt.

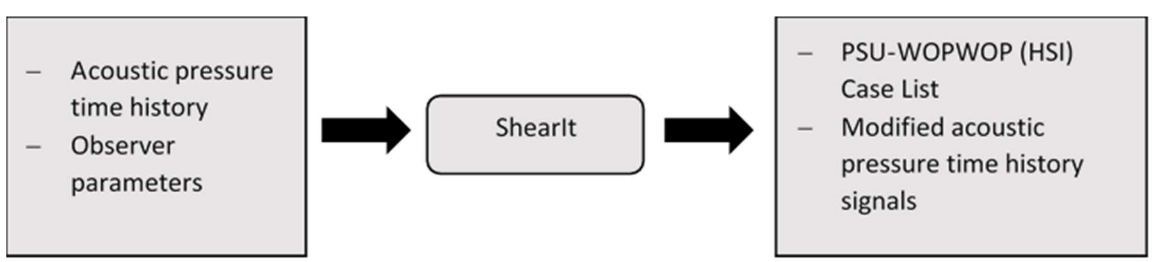

Figure 3.11: Diagram of the information passed into and out of ShearIt.

The ability to predict HSI noise without using computationally expensive methods (such as CFD) to examine shockwaves is very useful. Ultimately, this capability should be placed inside of PSU-WOPWOP. This would cut down on the need to pass so many parameter files from program to program, and ultimately simplify NPS. The inclusion of ShearIt inside PSU-WOPWOP would also eliminate the need to run PSU-WOPWOP a second time using the capability to read in acoustic pressure files. Furthermore, this capability would also enable the HSI model to be used by PSU-WOPWOP users that run cases not dependent on NDARC or the NPS at all. For this reason, ShearIt was built in a modular way that it could fit into PSU-WOPWOP without a major re-write.

ShearIt was added to the NPS, so now the user can model HSI noise without any extra steps to complete. If the user is modeling HSI noise, ShearIt is executed after PSU-WOPWOP has finished calculating the acoustic prediction for all cases. After ShearIt has finished adjusting the acoustic pressure time history for each case, NPS will run PSU-WOPWOP one last time. This will predict the noise for teach case with the effects of HSI included. Figure 3.12 shows the final flow chart of the execution order of NPS. Note that in this new graphic, the additional outputs that WOPIt and ShearIt can provide are included. Examples of these WOPIt outputs are shown in chapters 4 and 5, while the ShearIt outputs are shown in chapter 6.

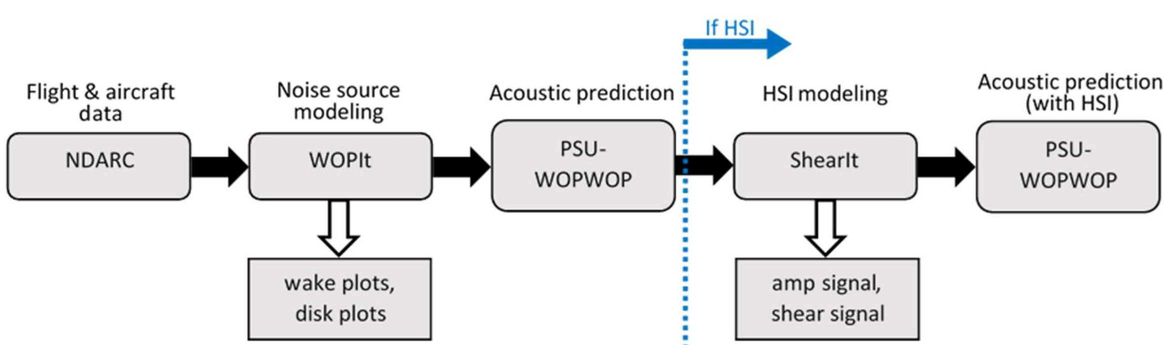

Figure 3.12: Updated diagram of the programs executed by the Noise Prediction System.

Aerodynamic Interaction Modeling

Any upstream disturbance can cause unsteady loading on the rotor disk. This project focused on blades interacting with their own trailed wakes; however, there are other sources of aerodynamic interactions as well. To completely model aerodynamic interaction noise, the model needs to be expanded. Interactions coming from other rotors as well as any upstream structure should be accounted for.

The BVI model implemented in NPS calculates the impact that a rotor's wake has on its blades. It does not, however, calculate the effect that a wake trailing behind a rotor may interact with a different rotor. Depending on the configuration this could be a significant source of noise due to the unsteady effects on the blade loads. With some modifications the model that is used to track the wake geometry and adjust the blade loads could be used to model interactions with a downstream rotor. This is addressed in chapter 5.

Any upstream component of an aircraft can impact a downstream rotor. Currently, the NPS does not model any aerodynamic interactions due to upstream components. Just like the rotor-rotor interactions, this could be a significant source of noise. The original project in 2016 proposed a prototype for interaction noise, however it was never completed. This iteration of the project also did the same. A model that projects the basic geometry of an aircraft component downstream is proposed for future work. Such a model could mimic the loss of lift and adjust the blade loads in the same way the BVI model does. This is discussed in chapter 5.

Chapter 4

Loading Noise

This chapter describes the models that are used in WOPIt to calculate blade loading. These loads are used by PSU-WOPWOP to compute loading noise. First the model used to calculate blade loading are discussed. Blade loads are calculated on a discretized rotor disk. These loads are trimmed to ensure that the rotor matches the conditions that were computed in NDARC. The trim model iterates the blade loading equations so the rotor's thrust force and moments are equal to the values in NDARC.

After introducing these models, results are discussed. First, the blade loading model is validated by comparing results to another model in identical conditions. Next two cases, hover and forward flight, are discussed. The blade loading (and other key variables used in the blade loading model) are plotted on a discretized rotor disk. Finally, the loading noise calculated by PSU-WOPWOP is shown for both cases. The acoustic pressure time histories are plotted for varying observer positions, and the OASPL is plotted for a hemisphere of observers for both cases.

Loading Noise Models

PSU-WOPWOP calculates the loading noise from the dipole term in the FW-H equation as discussed in chapter 2. To do so, it requires inputs of time-dependent loading distributed spanwise along the blade as it rotates. The needed input is created in WOPIt using the models described below. These models are used to calculate the base loading. The base loading does not include localized unsteady or impulsive effects. Periodic loading or slowly varying loading on the rotor disk are accounted for in the base loading model. Unsteady interactions that affect the blade loads such as BVI also affect loading and are important for loading noise computation. These unsteady interaction effects are calculated separately then added to the base loading. This method allows for noise modeling of BVI and other interactions with reduced computational effort. These interactions are discussed at length in chapter 5.

Blade Load Model

The blade loading model is based on the blade element analysis of forward flight described by Leishman [1]. Blade element theory (BET) divides the rotor into radial stations and tracks the loading at discrete azimuth angles around one rotor revolution. It assumes that each blade station can be represented as a quasi-steady 2D airfoil, and analyzes the resulting aerodynamic forces and moments. Each blade element is assumed independent, and the blade loads from that element are integrated over all azimuthal steps for one rotor revolution to calculate the rotor performance. BET is used in modern helicopter analysis because the two dimensional approximation for each blade element is appropriate for the long slender blades typically used on rotorcraft. Furthermore, BET works well in design and performance computations because the blade section aerodynamics can be extracted from look-up tables or simple models (as is done in this work). Blade element theory was chosen in this work to model the blade loads because it is computationally simple while also yielding accurate results. It is compatible with the details that are readily available at the conceptual design phase, and can provide loading at a sufficient resolution for PSU-WOPWOP to calculate the acoustic results. Unsteady effects can also be modeled by adjusting the steady loading. Unsteady effects will be addressed in detail in chapter 5. For all of these reasons, BET was ideal for the NPS.

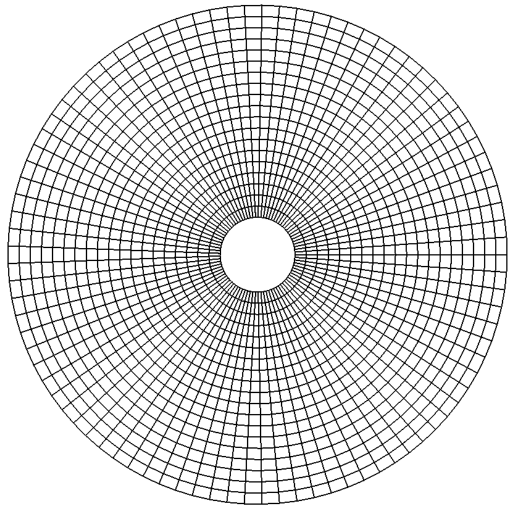

Figure 4.1: Discretized rotor disk with 20 equally spaced spanwise stations and 90 equally spaced azimuthal stations.

The rotor disk is discretized in to radial and azimuthal stations, as shown in Figure 4.1. The blade is assumed to be acoustically compact, as described in chapter 3, so it is modeled as a lifting line. To calculate the overall thrust provided by the rotor, the lift and drag forces are calculated at each blade element at each azimuth, and then integrated both over the span and around the azimuth. The differential forces acting perpendicular and parallel to the rotor are calculated using

$$dF_z = \frac{1}{2}\rho c C_{l_\alpha}(\theta U_T^2 - U_P U_T)dr \tag{4.1}$$

and

$$dF_x = \frac{1}{2}\rho c C_{l_\alpha}\left(\theta U_P U_T - U_P^2 + \frac{C_d}{C_{l_\alpha}}U_T^2\right)dr \tag{4.2}$$

where the subscripts x and z represent the directions perpendicular and parallel to the rotor disk, c is the local blade chord, θ is the local blade twist angle, C_{l_α} is the local lift curve slope, C_d is the local drag coefficient, and U_P and U_T are the velocities perpendicular and tangential to the blade element. It is assumed that the radial force acting in the spanwise direction is zero. Figure 4.2 shows the resulting forces and moments acting on a blade element.

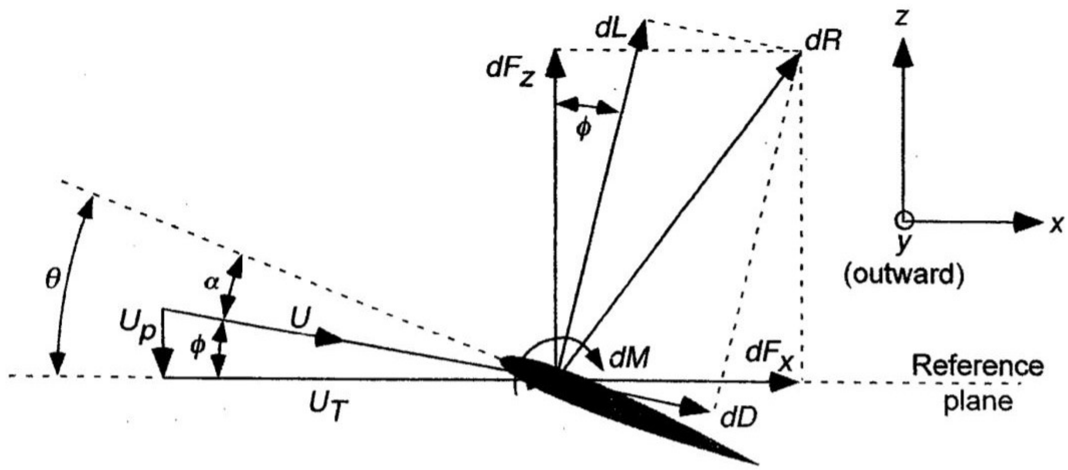

Figure 4.2: Forces and moments acting on a blade element [1].

To calculate the net thrust and power the induced inflow distribution across the rotor is necessary. For the steady loading calculations, a linear inflow is assumed. A modified version of Glauert's inflow model as described by Leishman was used for the inflow ratio. The inflow ratio is calculated for each blade element using

$$\lambda_i = \lambda_0\left(1 + k_x r\cos\psi + k_y r\sin\psi\right) \tag{4.3}$$

where k_x and k_x are weighting factors that control lateral and longitudinal inflow. The weighting factors chosen were used by Coleman et al. [1] where $k_x = \tan\frac{\chi}{2}$ and $k_y = 0$. The wake skew angle χ is defined as

$$\chi = \tan^{-1}\left(\frac{\mu_x}{\mu_z + \lambda_i}\right) \tag{4.4}$$

where μ_x and μ_z represent the advance ratio parallel and perpendicular to the rotor disk, respectively. The mean induced inflow ratio is calculated by

$$\lambda_i = \lambda_0 = \frac{C_T}{2\sqrt{\mu_x + \lambda_i}} \tag{4.5}$$

which requires numerical convergence with equation 4.3. The mean induced inflow ratio and inflow ratio equations are dependent on each other, and converge through numerical iterations. The linear inflow model is used in the calculation of the base loading, and should not be confused with the Beddoes inflow model that is used to calculate the trailing wake trajectory, which is described in chapter 5.

The in-plane velocity component is comprised of a rotation term and a translation term. It can be calculated by

$$U_T = \Omega \mathrm{R}(r + \mu \sin(\psi)) \tag{4.6}$$

where R is the blade radius, Ω is the angular rate of rotation, and r is the local non-dimensional radius of the spanwise station. The azimuthal angle is denoted by ψ. By convention, $\psi = 0$ is the direction that points to the tail rotor, $\psi = 180°$ points in front of the aircraft, and positive rotation is counterclockwise. The advance ratio of the aircraft, μ, is the forward velocity of the aircraft non-dimensionalized by the tip speed i.e., $\mu = \frac{V_f}{\Omega R}$. The out-of-plane component is comprised of a term for inflow velocity and two terms that are caused by blade flapping motions. It is calculated using

$$U_P = \Omega \mathrm{R}\left((\lambda_c + \lambda_i)r + r\dot{\beta} + \mu\beta\cos\psi\right) \tag{4.7}$$

where λ_c is the inflow due to climb, and β is the blade flapping angle. The dot above a variable denotes a time rate of change. The middle term accounts for the flapping velocity, while the third term accounts for velocity caused by the blade coning.

Once the differential forces have been calculated for every spanwise station, an integration is performed. The forces along the blade are calculated using

$$F_Z = \int_0^R dF_z\, dr \tag{4.8}$$

and

$$F_X = \int_0^R dF_x\, dr \tag{4.9}$$

again assuming that $F_y = 0$. Then blade forces are calculated for every azimuthal station. The net rotor forces are calculated by finding the time average of the forces over one rotor revolution. The net thrust, side force, and drag force are calculated with

$$T = \frac{1}{2\pi}\int_0^{2\pi} F_z \, d\psi \tag{4.10}$$

$$H = \frac{1}{2\pi}\int_0^{2\pi} F_x \sin\psi \, d\psi \tag{4.11}$$

$$Y = \frac{1}{2\pi}\int_0^{2\pi} F_x \cos\psi \, d\psi \tag{4.12}$$

by integrating across the azimuth. The rotor is trimmed through a procedure to ensure that the BET forces and moments match NDARC for the flight condition. The trim model, control variables, and convergence algorithm are explained in the next section.

Rotor Trim Model

To ensure that WOPIt is modeling the same conditions as NDARC, the blade load equations (4.1-4.12) are inside of a trim loop. WOPIt trims the rotor to match NDARC's prescribed thrust and moments about the x and y axes by changing the control variables. These controls are the collective pitch, lateral cyclic pitch, and longitudinal cyclic pitch (θ_0, θ_{1c}, and θ_{1s}). The control variables affect the terms in the blade loading equations. The blade pitch of the spanwise station, θ, is calculated by

$$\theta = \theta_0 + \theta_{1s} + \theta_{1c} + \theta_{tw} \tag{4.13}$$

where θ_{tw} is the local twist of the blade geometry. Blade flapping motion is also dependent on the control variables.

The iterative trim algorithm matches each control variable to a target variable. Thrust is trimmed with collective pitch, M_x is trimmed with longitudinal cyclic pitch, and M_y is trimmed with lateral cyclic pitch. The system trims each variable independently. In other words, while M_x is trimmed, the thrust force may no longer match the NDARC target because that was not the focus of this specific iteration. The entire trim algorithm is in a loop. Each iteration takes control variable information from the last iteration while trimming to a specific variable. This only concludes when all three trim conditions are met. First, θ_0 is adjusted until the calculated thrust matches NDARC's target thrust. θ_{1s} and θ_{1c} are not changed during the thrust interactions, so they are initialized to zero. Next, θ_{1s} is adjusted until the calculated M_x matches NDARC's M_x. For this trim iteration, the value of θ_0 is held fixed, but θ_{1c} is still zero. Then θ_{1c} is adjusted until the calculated M_y matches NDARC's M_y. The values of θ_0 and θ_{1s} are held fixed throughout the θ_{1c} iteration. At this point all three control variables have been used to trim to their target value. However, since each trim was independent, the values of thrust and M_x may not be trimmed after the M_y calculation completes. To ensure that the rotor is fully trimmed, the trim algorithm checks to see if all three trimmed values (T, M_x, M_y) match NDARC. If they do not, the three-step process is repeated. Thrust is trimmed by iterating θ_0 again, but this time θ_{1s} and θ_{1c} have values from the previous loop. This three-step algorithm is repeated until all three values match NDARC's target values, which indicates the rotor is trimmed. Figure 4.3 is a schematic of the trim loop algorithm. WOPIt trims each individual rotor to match the values that were calculated in NDARC. Isolating each individual rotor in WOPIt is sufficient, because the entire aircraft is trimmed in NDARC.

Trim Loop

1) Trim to **thrust** using $\boldsymbol{\theta_0}$
2) Trim to $\boldsymbol{M_x}$ using $\boldsymbol{\theta_{1s}}$
3) Trim to $\boldsymbol{M_y}$ using $\boldsymbol{\theta_{1c}}$

If all 3 trim conditions are not met, restart from 1)

Figure 4.3: Algorithm used for rotor trim model.

This trim process may not be the most conventional way of trimming a rotor, but the process is relatively fast – it typically converges to within 0.1 percent of the target value in two or three iterations of the three-step process – and is computationally inexpensive. It was easily implemented with the BET model of loading. This makes it suitable for NPS because it fits the goal of simple modeling that is fast and accurate. The rotor typically trims in just a few loops; an example trim convergence is shown in Figure 4.4. Iteration 1-1 trims the thrust value but M_x and M_y are not trimmed. Iteration 1-2 trims M_x, which causes thrust to fall out of trim. Iteration 1-3 trims M_y, which causes M_x to be slightly out of trim, while thrust is not trimmed at all. In iteration 2-1 thrust is trimmed again, and the moments are closer to trim than they were the previous time thrust was trimmed (1-1) thanks to the control inputs carrying over from each iteration. This continues until all three approach target trim at the same time. Once the rotor is trimmed, the blade loads can be used to calculate the loading noise for the aircraft. NDARC trims the aircraft for each flight condition. NPS uses the trimmed rotor information from NDARC, and must match that trim. Therefore, WOPIt can trim each individual rotor to match the conditions provided by NDARC. The following section shows the results of the blade load computations in WOPIt as well as loading noise calculated by PSU-WOPWOP.

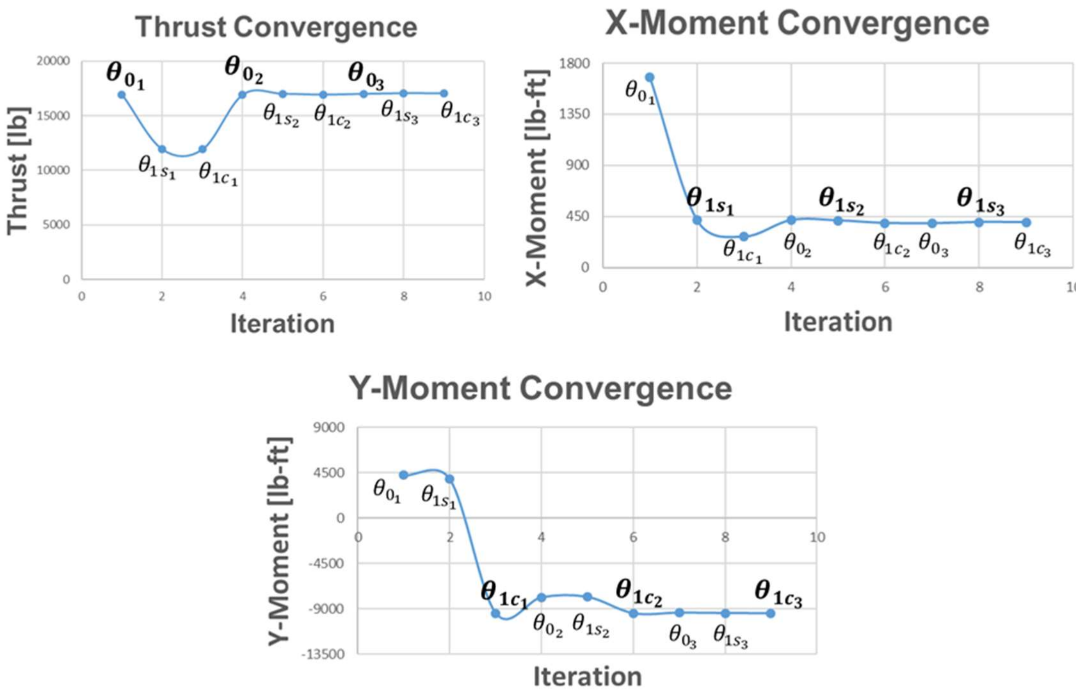

Figure 4.4: Convergence of the trim variables. The subscript number denotes number of cycles through the loop. A bolded term denotes that the algorithm is directly trimming for that variable.

Loading Results

This section shows the results of the blade loading where a hover case is compared with a forward flight case. Disk plots are used to plot key variables from the BET model, including thrust force, moments, inflow ratio, and parallel and perpendicular velocities, over the rotor disk. Validation for the loading model was performed and is shown in this section. Finally, acoustic results calculated with the blade loading model are discussed.

Blade Loading Validation

To validate the loading model, results were compared to another blade element theory study completed by Yaakub et al [31]. Yaakub et al. used helicopter data from Prouty [32] as a comparison for the angle of attack distribution across the rotor disk. In BET, the angle of attack is directly proportional to the lift force, so it can be used to validate loading. The Prouty helicopter was modeled in the exact same manner as Yaakub et al. The description of the rotor and flight condition is listed in Table 4.1 below.

Table 4.1: Helicopter specifications and flight conditions

Helicopter Specs	
Number of blades	2
Blade radius	9.144 m
Chord	0.61 m
Root cutout	0.15
Airfoil	NACA 0012
Azimuthal resolution	50 stations
Radial resolution	50 stations
Flight Conditions	
Flight speed	59.16 m/s
Tip speed	197 m/s
Collective pitch	15.8°
Lateral cyclic pitch	-2.3°
Longitudinal cyclic pitch	4.9°

These specifications and conditions were recreated identically in the BET model that is included in NPS. The angle of attack was plotted across the rotor disk in the same orientation and scale as Yaakub et al. The comparison between WOPIt results and Yaakub et al. are shown in Figure 4.5. The agreement between the WOPIt results and those computed by Yaakub et al. are nearly identical. From the results, it is clear that the helicopter is flying towards the top of the page and the blades are rotating counterclockwise. Thus the advancing side is on the right side of this figure. A reverse flow region is present on the retreating side of this blade. This validation provides confidence that the BET loading model in WOPIt was implemented correctly. More results are shown and discussed in the next section.

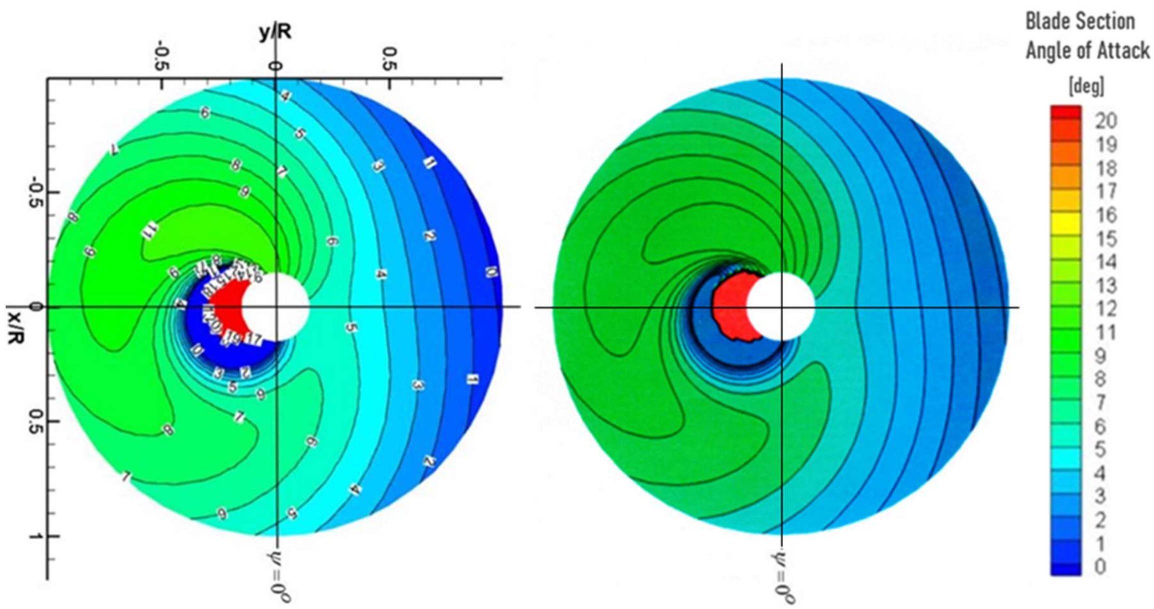

Figure 4.5: Comparison of blade sectional angle of attack computed for the Prouty helicopter by Yaakub et al. (left) [31] and WOPIt (right).

Blade Loading Results

This section displays the results produced by the BET model in WOPIt for an example helicopter case designed in NDARC. Two flight conditions are shown, one in hover and the other forward flight. The specifications for this helicopter are shown in Table 4.2. The blade loads discussed here are used by PSU-WOPWOP to calculate the acoustic results for loading noise. The acoustic results are discussed in the next section.

Table 4.2: NDARC Helicopter main rotor specifications

Helicopter Specs	
Number of blades	4
Blade radius	7.62 m
Chord	0.1754 m
Root cutout	0.15
Azimuthal resolution	180 stations
Radial resolution	30 stations

The first flight condition is a hover case. The helicopter is operating with a tip speed of 213 m/s, or a revolution speed of 267 RPM. The blade loading perpendicular to the rotor disk (thrust direction) is shown in Figure 4.6. This disk plot models the loading at each span position along the discretized blade, as well as each azimuthal station. In this case, the rotor is not translating and the blades are rotating counterclockwise. Since the rotor is in hover, the loading is balanced because the flow is axisymmetric. The loading values are smallest near the hub of the rotor, and highest towards the tip. The tip of the rotor does not produce high lift because the loading model must go to zero at the tip. The contributions of each span station to the net moment of the rotor are plotted in Figure 4.7. A force that would cause the rotor to rotate counterclockwise about the respective axis results in a positive moment. A balanced rotor disk is achieved when the sum of all moment contributions results in a net zero moment. These moments are balanced during the rotor trim algorithm. Since the loading is equal in all directions, the contributions to the net moments are balanced on each side of the rotor. In hover, the inflow model returns the hover solution of uniform inflow, and the perpendicular and tangential components of velocity are also balanced.

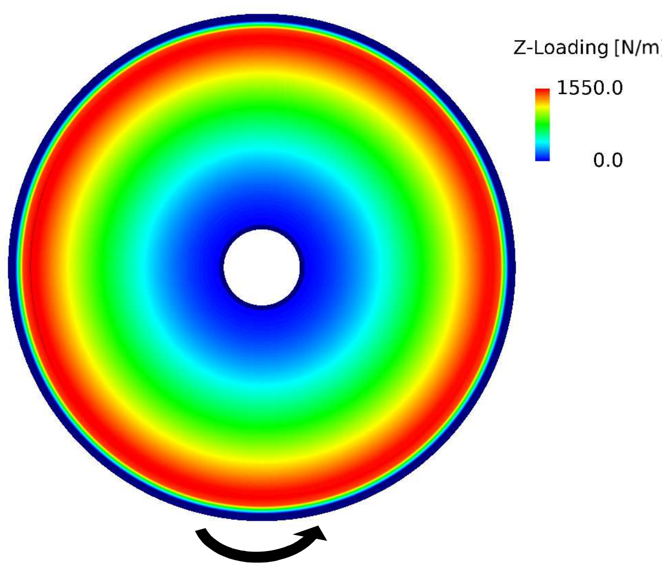

Figure 4.6: Z-Loading on the main rotor in hover flight condition.

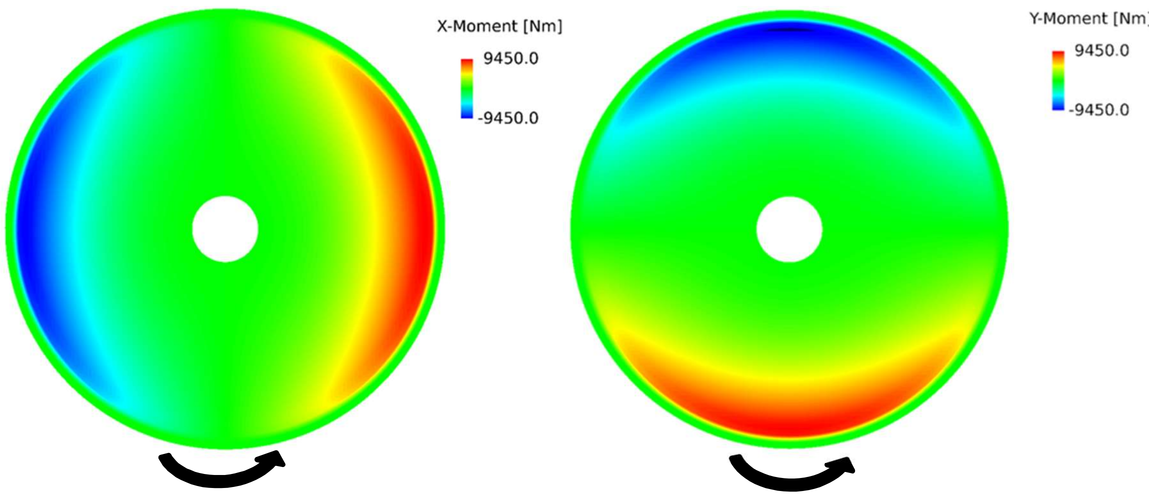

Figure 4.7: Moments acting on the helicopter main rotor in hover. (Left: roll moment, Right: pitch moment).

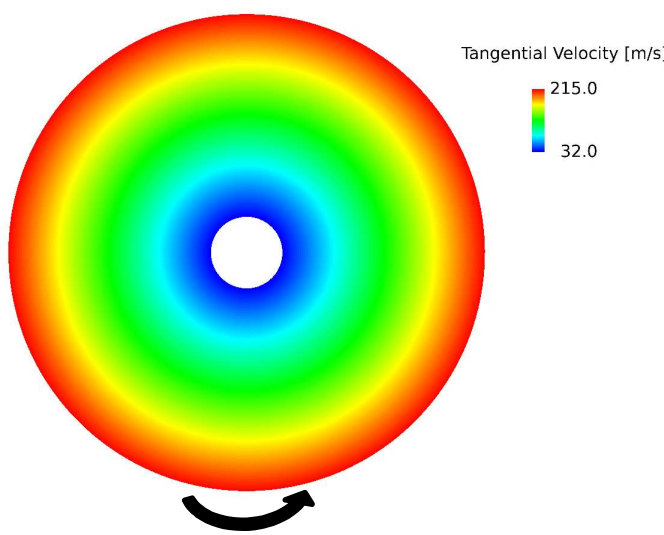

Figure 4.8: Tangential velocity on the main rotor blade in the hover condition.

Results were also generated for the same helicopter rotor in forward flight. The rotor was operating with a forward flight speed of 100 knots, with an advance ratio of 0.241. The blade loading perpendicular to the rotor for this case is plotted in

Figure 4.9. The rotor moments are plotted in Figure 4.10, while inflow ratio, and blade velocities are plotted in Figure 4.11. In these plots, the helicopter is flying towards the top of the

page, while the blades are rotating counterclockwise. On the retreating side of the blade there is a clear reverse flow region. In this region, the blade produces little lift, or in this case a small force in the opposite direction. On the advancing side, lift is smallest at the hub and increases towards the tip. The linear nature of the inflow ratio is clearly seen in figure 4.11. Inflow ratio is highest on the side that is opposite of the flight direction ($\psi = 0$), and linearly decreases as the stations get closer to the front of the aircraft ($\psi = 180$). The advancing side of the blade is moving much faster than the retreating side, which is clear in the tangential velocity profile in figure 4.11. The advancing blade has much higher tangential velocity magnitudes than the retreating sides. The offset in speeds on each side of the blade change the blade parameters when compared to a hover case. The forward flight case is not axisymmetric, and the velocity profiles of the advancing and retreating sides differ. More area on the advancing side contributes to the roll moment, so a larger angle of attack on the retreating side compensates for it. The pitch moment is fairly balanced, but skews towards the retreating side.

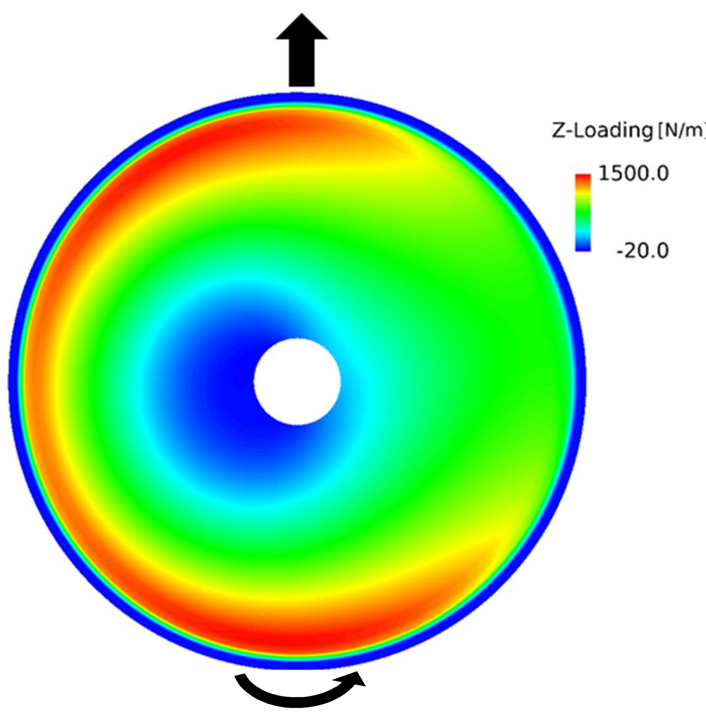

Figure 4.9: Z-Loading on the main rotor in forward flight condition.

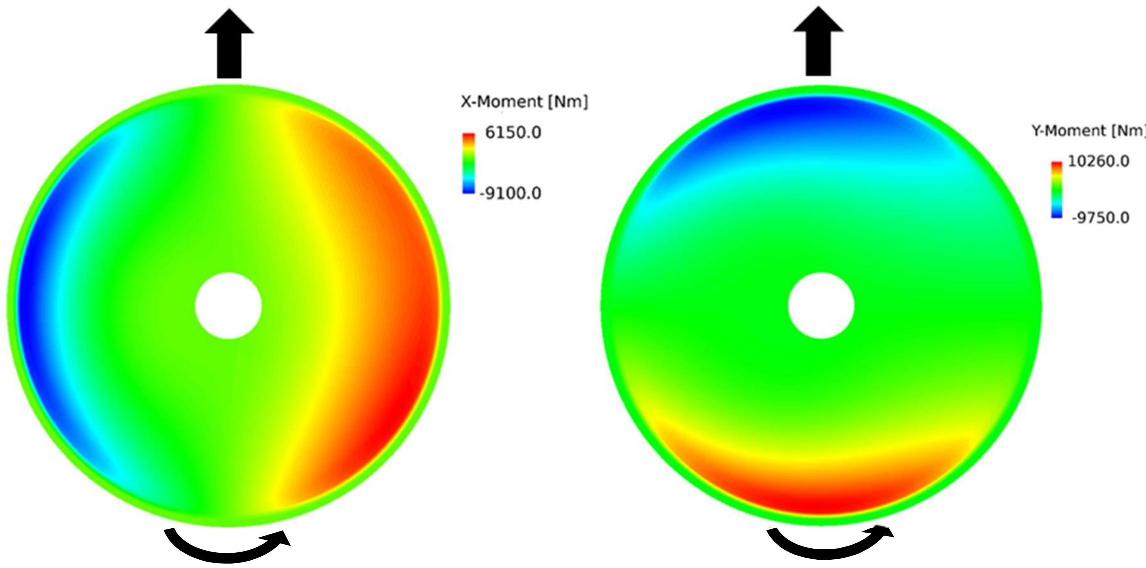

Figure 4.10: Moments acting on the helicopter main rotor in forward flight. (Left: roll moment, Right: pitch moment).

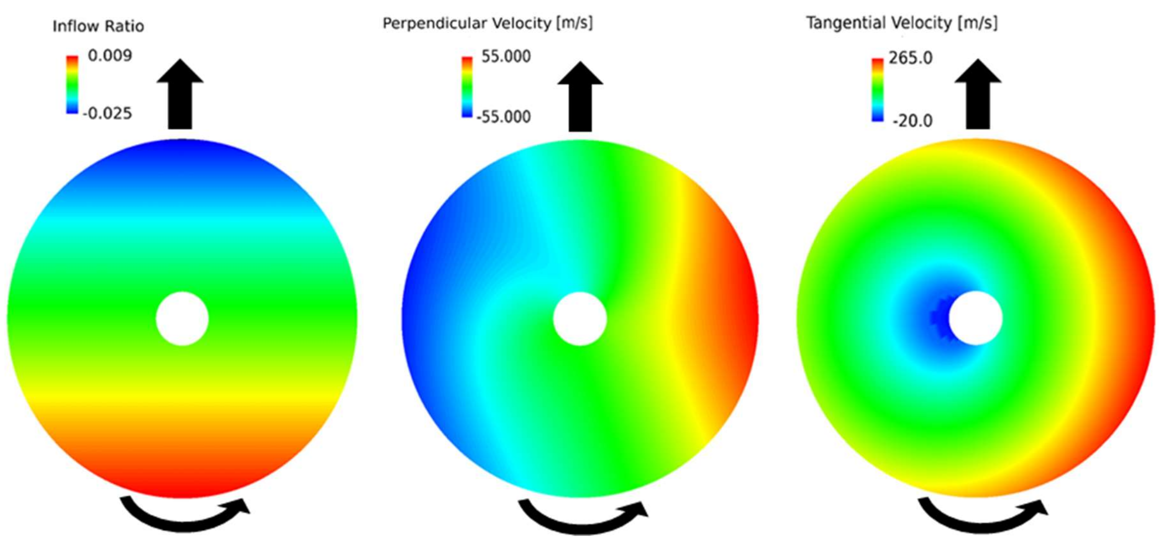

Figure 4.11: Inflow ratio (left), perpendicular velocity (center), and tangential velocity (right) for the main rotor disk in forward flight.

Loading Noise Results

The trimmed blade loads calculated by WOPIt are used by PSU-WOPWOP to calculate the acoustic output. The loading from the hover and forward flight cases are used to find the acoustic pressure time history for an array of observers at different points around the helicopter. The loading noise directivity and magnitudes are compared between the two cases. Finally, OASPL is computed on a hemisphere of observers below the aircraft.

Five observers were places around the aircraft to demonstrate the directivity of the loading noise. Observers were placed directly in front of and behind the aircraft in the plane of the rotor, as well as three out-of-plane observers placed directly below and at elevations of 45° below the rotor disk. The resulting acoustic pressure time histories of one rotor revolution are plotted for each observer in Figure 4.12 and Figure 4.14 for hover and forward flight, respectively. These observers are “attached to” the aircraft, which means that while the aircraft is moving, the observer moves in an identical way so that the relative observer distance is identical throughout the entire plot. The OASPL was also computed for an observer hemisphere. This hemisphere was constructed of 225 observers – 15 observers equally spaced in the elevation direction and 15 observers equally spaced around the azimuth. These plots show the dB level of the loading noise at that location in space. These plots are shown in Figure 4.13 and Figure 4.15 for hover and forward flight respectively.

In the hover case, the acoustic pressure time history values are fairly low. Since the loading is not time dependent around the azimuth, and there is no propulsive thrust needed, the magnitude of the loading noise is lower. In-plane pressure disturbance is very low. This is expected for in-plane steady loading. There is no advancing or retreating side, the pressure is equal for each azimuth station. For this reason, the observers at equal distances in front of or behind the rotor yield identical results for any elevation. Directly below the rotor there is essentially no pressure fluctuation. This occurs because in hover, there is no loading change in any direction around the hub axis. In a real flight, this will not occur, because even in hover there are unsteady effects including turbulence, interactions with the aircraft, and other unpredictable changes. The out-of-plane observers at angles approximately 20° to 40° see the highest acoustic pressure time history magnitude. This is also clear in the OASPL contour plot. The observers that see the highest dB magnitudes are approximately 25° out of the rotor plane.

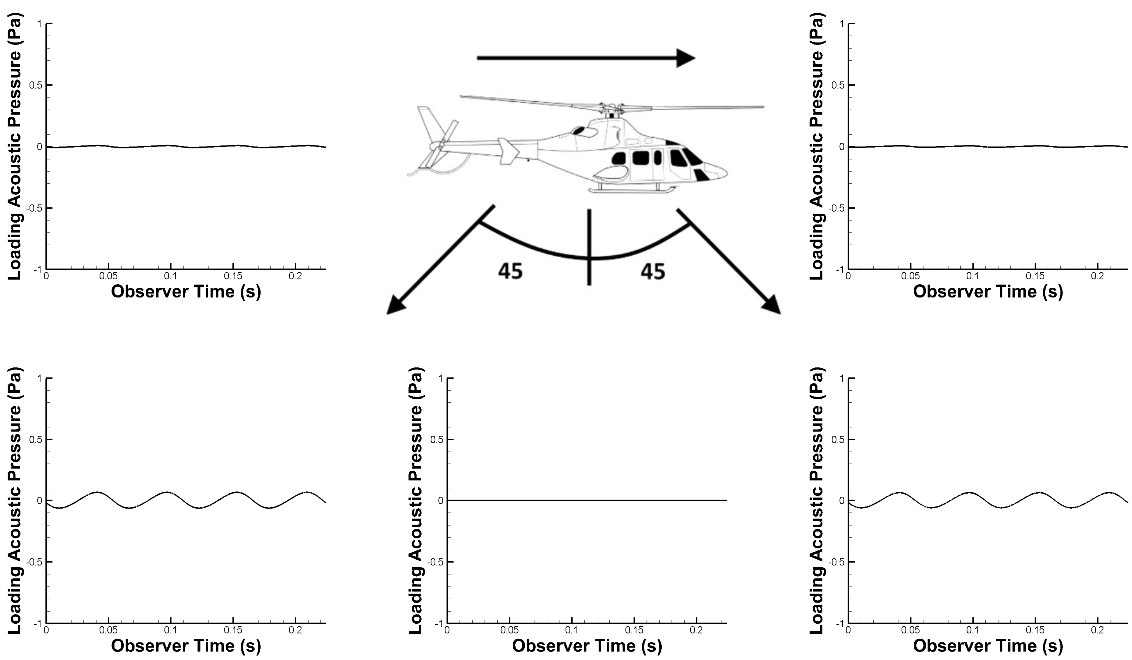

Figure 4.12: Acoustic pressure time history for observers positioned around the aircraft 10 rotor radii from the main rotor hub for the hover case.

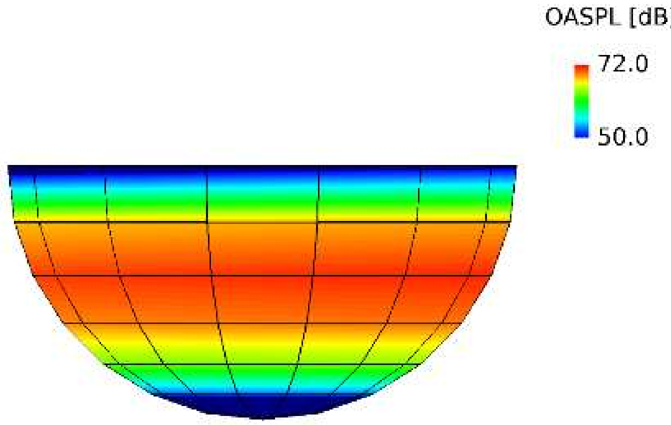

Figure 4.13: OASPL plotted on an observer sphere 10 rotor radii away from the main rotor hub for the hover case.

In forward flight, the main rotor must provide the lifting force and the propulsive force. As loading noise is proportional to the magnitude of the blade loads, this increases loading noise. In forward flight the loading changes around the rotor disk at different azimuth stations, because the forward flight velocity creates advancing and retreating sides on the rotor. The changes in loading around the azimuth cause the loading noise levels to be louder in forward flight because loading noise is dependent on the time rate of change of the blade loading. Equation 2.4 shows that the loading noise is proportional to the Doppler amplification term $\left(\frac{1}{1-M_r}\right)$. Its effect on the loading noise is greatest when the blade velocity approaches $M_r = 1$. In the forward flight case, observers in front of the aircraft see higher Doppler amplification because the forward flight velocity increases the velocity of the blades on the advancing side of the rotor. In the hover case the highest recorded M_r value is 0.62, while in the forward flight case the highest M_r value is 0.77. It is important to note that for these loading noise calculations, no HSI effects were included.

All observer locations yield a higher magnitude in acoustic pressure time history. Note that the y-axes in Figure 4.14 are much larger than the hover case to show the acoustic pressure more clearly. Because the aircraft is moving forward, the observers in front of the aircraft see a higher magnitude in acoustic pressure. In the forward flight case, the main rotor tilts forward about 3° which may increase the loading noise in the plane of the rotor. The out-of-plane observer that is in front of the aircraft sees the dominant loading noise signal. The OASPL is highest in the direction that the aircraft is moving. The observers on the advancing side of the blade have a slightly louder noise signal. This occurs because the Doppler amplification term is highest in this region. Observers between angles of 25° and 40° out of plane experience the loudest loading noise signal.

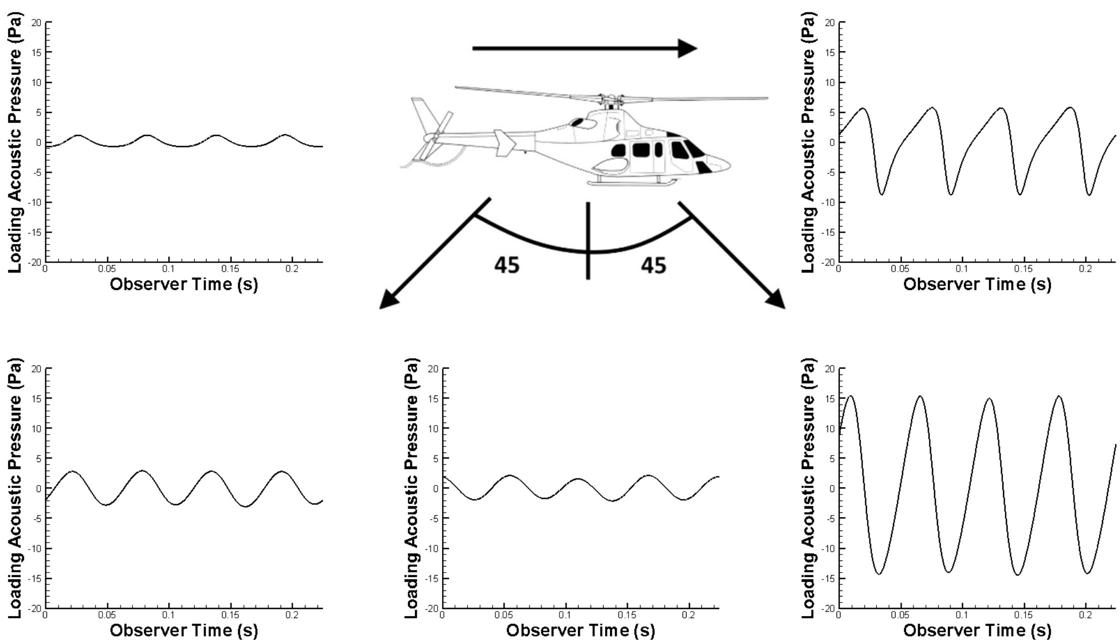

Figure 4.14: Acoustic pressure time history for observers positioned around the aircraft 10 rotor radii away from the main rotor hub for the forward flight case.

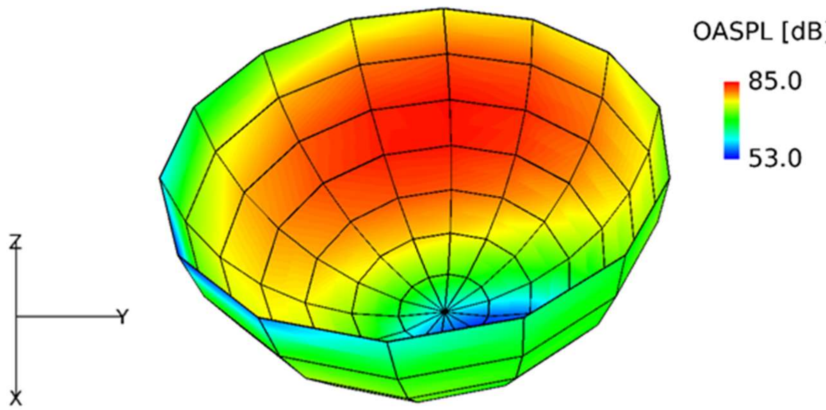

Figure 4.15: OASPL plotted on an observer sphere of radius 10 rotor radii for the forward flight case.

Chapter Summary

This chapter explored the blade loading model, and showed the acoustic results for two simple cases. BET is used to calculate the differential forces acting at each node of the discretized rotor disk. These loads do not contain interaction effects from other aircraft components or wake disturbances. To account for interaction loading, the BET model discussed in this chapter can be adjusted. Chapter 5 explores how unsteady interactions can modify the steady loading to model the effects on the noise output. It outlines the models for BVI, and explains how interactions add unsteady effects to the blade loads.

Chapter 5

Wake Modeling and Blade-Vortex Interaction

Unsteady interactions can dramatically change the blade loading and loading noise output of the vehicle. When disturbed fluid interacts with the rotor blades, the inflow of the rotor changes. Disturbances can be caused by upstream aircraft components, blades operating in their own wakes, or tip-vortices shed by another rotor. These disturbances induce a velocity on following rotor blades. The interaction model uses these induced velocity effects to adjust the blade loads. Because blade element theory assumes that each blade element is independent, each blade station can be individually adjusted to model the unsteady effects of interactions. WOPIt uses an ad hoc method to model the influence of BVI. After the steady loading is calculated for the rotor, the unsteady effects due to interactions are calculated. These unsteady interactions are added to the blade loading that was discussed in chapter 4, resulting in unsteady loading on the rotor. This is the basis of the interaction model included into NPS. This chapter explores the models that are were implemented in NPS. The calculation of trailing wake geometry and the interaction effects are discussed. Finally results are shown for a helicopter in a BVI condition, as well as a prototype case for rotor-rotor interactions. A potential model for aerodynamic interaction noise is proposed in this section, and is further discussed in the future work section of chapter 8.

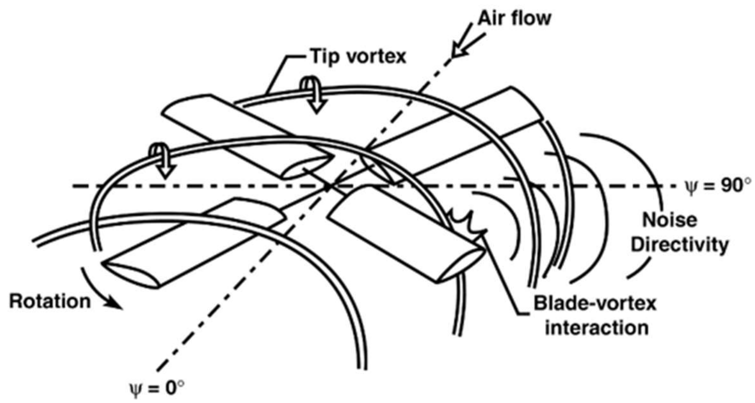

Figure 5.1: Diagram showing a rotor interacting with its trailed tip vortices [4].

Blade-Vortex Interaction

As a rotor spins, the blade tip experiences high loading. Flow travels around the blade tip from the high pressure region to the low pressure region. This flow rolls up and results in tip vortices. Blade-vortex interaction occurs when the rotor blades interact with these vortices. BVI can lead to highly impulsive loading on the rotor disk, which drastically increases the loading noise output. WOPIt uses the Beddoes wake model to describe the geometry of the trailed tip-vortices, and the discretized wake induces a velocity on the passing blades. The induced velocity from the tip-vortices is used to calculate a change in loading that is applied to the steady loading. This results in unsteady loading across the rotor disk that can be used to calculate the loading noise. The rotor is not re-trimmed after the unsteady interactions are added. This method increases the speed and efficiency of an NPS run. It also ensures that the unsteady models are adding details to the NDARC computations, not completely changing them. This is important because NDARC does not have a BVI model, and the rotor is already trimmed to match the NDARC condition with steady loading. The following sections describe this process in detail before showing the end results of the models.

Wake Modeling

To model the BVI effects in NPS, a wake model is needed in WOPIt. Modeling a wake can be very computationally expensive. It was important to choose a prescribed wake model as opposed to a free wake model to keep computational costs low. NPS may be used run a mission with many segments, so speed was a focus to ensure that modeling the wake for each rotor for each flight condition would not bottle-neck the system. The Beddoes wake model [33] was chosen because it can model the wake of the blade using only the tip vortex geometry, and it does not require information about the rotor that NDARC and the BET loading model cannot provide. This section follows Greenwood's [21] implementation of the Beddoes wake model in his dissertation work.

Rather than discretizing the entire wake, the Beddoes wake model only calculates the tip-vortex geometry as a three-dimensional curve. The location of the tip vortex geometry are governed by Beddoes' prescribed inflow over the rotor disk. The Beddoes inflow model combines the Glauert linear longitudinal inflow with a lateral cubic downwash [21]. The Beddoes inflow model has been further expanded by being combined with other prescribed inflow methods [34-35]. A general representation of the inflow calculation can be calculated with

$$\lambda_i = \lambda_{i_0}(A\chi(\cos\psi + |r_v \sin\psi|^3) + 2B\mu_x \sin\psi + C) \tag{5.1}$$

where the mean induced inflow ratio, λ_{i_0}, is calculated by

$$\lambda_{i_0} = \frac{C_T}{2\sqrt{(\mu_z + \lambda_i)^2 + \mu_x^2}} \tag{5.2}$$

which requires a numerical iteration of equations 5.1 and 5.2 to solve for λ_i. The coefficients A, B, and C are used to control the components of the prescribed inflow distribution. The general equation can be changed to match experimental data by manipulating these values. The original Beddoes wake model [33] is achieved by setting A and C to 1 while setting B to 0. Setting B to 1 adds the Drees lateral inflow as suggested by van der Waal [34]. Decreasing A weakens the wake skew, which was recommended by later works [21]. Increasing C controls the mean inflow ratio, which can account for the root cutout region. It is not known which values are best ahead of time, but in this work the values 0.5, 1.0, and 1.1 were assumed for A, B, and C, respectively, as default values. When running the NPS, these values can be changed by the user if desired, to ensure that the NPS allows the flexibility to account for any knowledge that a designer may have. The wake skew angle is defined as

$$\chi = \left| \tan^{-1} \frac{\mu_x}{\mu_z + \lambda_{i_0}} \right|. \tag{5.3}$$

The vertical location of the tip vortex geometry is calculated by

$$\tilde{z} = \mu_z \phi - \lambda_{i0} \phi \left[A\chi \left(\cos \psi_v + \frac{\mu_x \phi}{2r_v} - |r_v \sin \psi_v|^3 \right) + 2B\mu_x \sin \psi_v + C \right] \tag{5.4}$$

Where ϕ is the wake age – the difference in blade angle and tip-vortex angle $(\psi_b - \psi_v)$ in radians. The original Beddoes wake model [33] did not account for wake contraction over time. This can be accounted for by incorporating Landgrebe's [36] contraction model where the radial vortex position is calculated by

$$r_v = r_r \left(D + (1 - D) e^{-(0.145 + 27C_T)\phi} \right) \tag{5.5}$$

where r_r is the original tip-vortex release radius, and D is a coefficient that controls the wake skew. Setting D to 1 yields the original Beddoes model, but the NPS defaults to 0.85. As with the other parameters, this can be adjusted by the user if desired. The lateral and longitudinal position of the tip vortices are calculated by

$$\tilde{x} = r_v \, cos \, \psi_v + \mu_x \phi \tag{5.6}$$

$$\tilde{y} = r_v \sin \psi_v \tag{5.7}$$

These positions are normalized by the blade radius. The trailing wake is calculated for the rotor at every blade azimuthal step. WOPIt models the trailing wake until it is sufficiently far away from the rotor and is no longer important for BVI calculations. The user has control over how many wake revolutions are calculated behind the blade. The lifting lines and trailing wakes can be output in plot3D format by WOPIt for visualization. These plots can be animated to see the trailing wake shape for an individual rotor, or for the entire aircraft at once, progress through time. This discretized wake model is used to induce a velocity on the blade as it comes close to the tip vortices.

BVI Models

Once the tip-vortex geometry has been calculated for the wake, the BVI model steps through each azimuth station to see the impact caused by the trailing wake. The induced velocity caused by each individual wake station (ψ_v) is calculated for each radial station. Figure 5.2 explains the induced velocity algorithm in the example of a two-bladed rotor. The snapshot included in Figure 5.2 is the first time step. The induced velocity needs to be calculated for the entire blade, so the algorithm starts at blade station A. To calculate the total induced velocity for this radial station every point on the discretized wake behind each blade needs to included. First the calculation is performed at every vortex segment trailing behind this blade. This starts at point B_1 and steps through every point through B_n. Once the induced velocity on blade station A is calculated for every tip-vortex segment trailing the first blade, the influence from the tip-vortices trailing other blades is addressed. For this two-bladed example, the next step is to calculate the induced velocity at blade station A caused by the tip vortices R_1 through R_n. At this time the total induced velocity at blade station A is calculated. The algorithm moves on to radial station B and calculates the total induced velocity. This is repeated through radial station Z, which provides the calculated induced velocity for all blade segments at this azimuth angle. Finally, the rotor is incremented to the next time step (azimuth angle) and the entire process is repeated. The procedure continues until the calculation has been completed at every azimuth angle until the rotor has completed a full revolution.

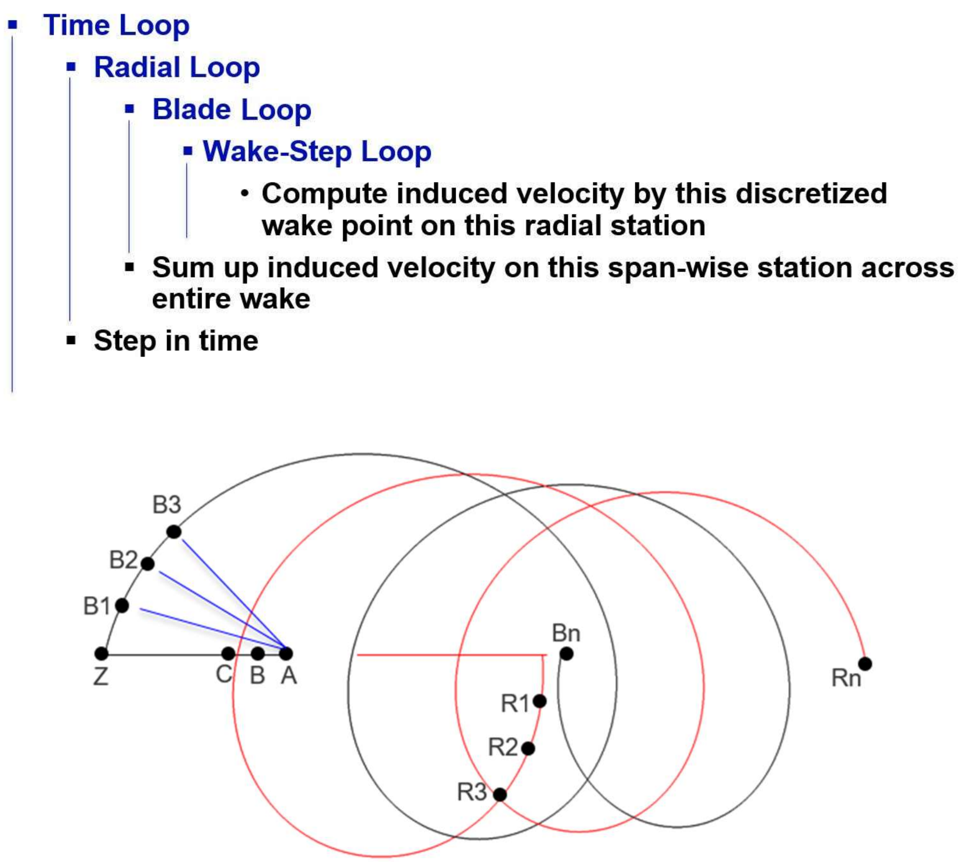

Figure 5.2: Algorithm used to calculate the induced velocity at every point on the discretized rotor disk.

The trailing wake is discretized into individual tip vortex elements. These elements are modeled as three dimensional vortices with individual source strengths. The induced velocity on the blade caused by each vortex can be calculated using the Biot Savart law [37]

$$d\vec{V} = \frac{\Gamma}{4\pi}\frac{d\vec{l} \times \vec{r}}{|r^3|} \tag{5.8}$$

where Γ is the strength of the vortex, the arc length element $d\vec{l}$ points along the discretized wake and $\vec{r}$ points from the point on the vortex to the point on the blade element. This can be integrated along the wake to get the total induced velocity. The vortex strength is calculated for each vortex segment using the Kutta-Joukowski theorem [1]:

$$\Gamma = \frac{L'}{\rho_0(\Omega r)} \tag{5.9}$$

where L' is the lift per unit span at the segment on the rotor disk that released the tip vortex. The notation and equations used to calculate the induced velocities on the blade follow the works of Sickenberger [38]. For a discretized wake the Biot-Savart law can be expressed in vector form for each individual wake segment as

$$\vec{V}_{ind} = \frac{\Gamma}{4\pi r_p}(\cos\theta_1 - \cos\theta_2)\hat{e} \tag{5.10}$$

where

$$r_p = \frac{|\vec{r}_1 \times \vec{r}_2|}{|\vec{r}_0|} \tag{5.11}$$

$$\cos\theta_1 = \frac{\vec{r}_0 \cdot \vec{r}_1}{|\vec{r}_0||\vec{r}_1|} \tag{5.12}$$

$$\cos\theta_2 = \frac{\vec{r}_0 \cdot \vec{r}_2}{|\vec{r}_0||\vec{r}_2|} \tag{5.13}$$

$$\hat{e} = \frac{\vec{r}_1 \times \vec{r}_2}{|\vec{r}_1 \times \vec{r}_2|} \tag{5.14}$$

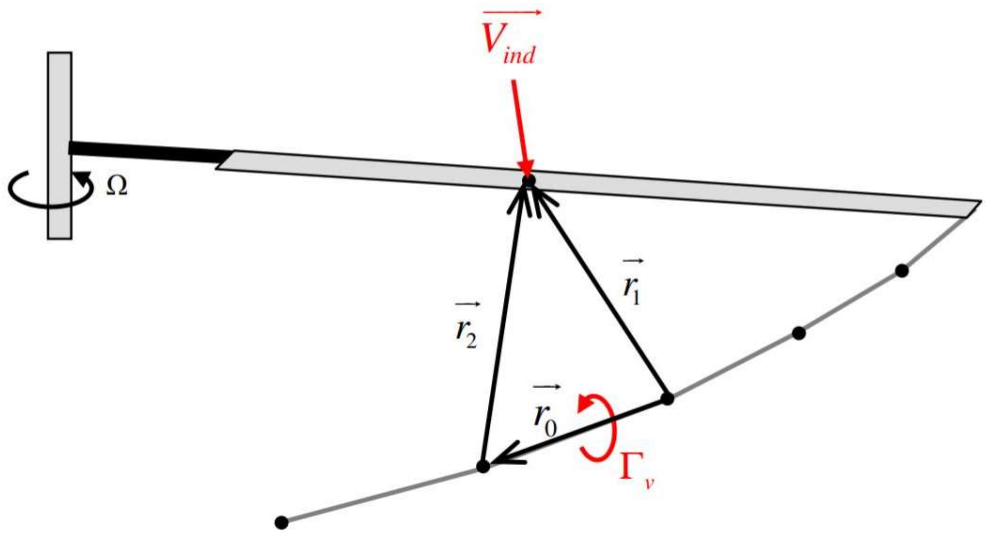

Figure 5.3: Vector definition of variables used in the Biot-Savart calculation used to calculate induced velocity from a vortex segment along the wake [38].

Figure 5.3 shows the vector definition of $\vec{r}_0$, $\vec{r}_1$, and $\vec{r}_2$. However, the Biot-Savart law exponentially approaches infinity as the distance between the blade and the vortex approaches zero. In a real fluid the vortex has a finite core radius and has solid body rotation within the core; therefore the induced velocity decreases once the core boundary is reached. To prevent this numerical singularity and mimic the vortex in a real fluid the Vatistas model [39] was created. Incorporating Vatistas model into the representation of the Biot-Savart law used in equation 5.10 can be expressed in vector form by

$$\vec{V}_{ind} = \frac{\Gamma}{4\pi} \frac{r_p}{\left(r_c^{2n} + r_p^{2n}\right)^{\frac{1}{n}}} (\cos\theta_1 - \cos\theta_2)\hat{e} \tag{5.15}$$

where r_c is the finite core vortex size and n determines which model is being used. Figure 5.4 shows multiple values for n, and the resulting induced velocity profiles. As n approaches infinity, the model becomes the Rankine vortex model [40] which assumes solid body rotation while inside the vortex core and Biot-Savart while outside of the core. This results in a sharp value at $r = r_c$ which is unrealistic. Other values of n smooth this discontinuity even further. This project uses the Bagai-Leishman model [41] by setting n to 2. This model was recommended because it agrees well with experimental data [1]. This project assumes that the vortex core size is approximately half the blade chord. This assumption is more accurate for aeroacoustic numerical calculations, as opposed to modeling them smaller.

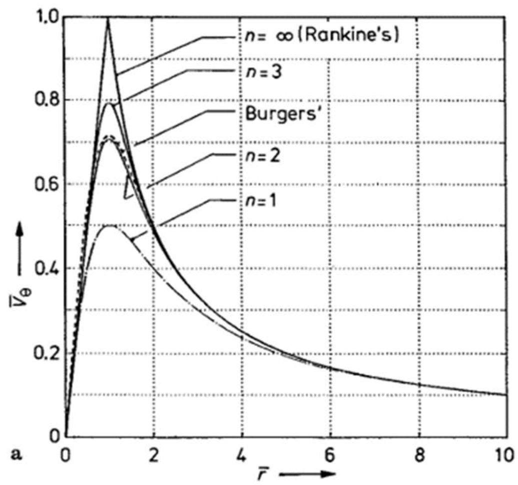

Figure 5.4: Tangential induced velocity as a function of distance between the vortex and blade (normalized by vortex core size) for varying models [33].

The induced velocity is calculated at each radial station for every wake segment. Once the resulting induced velocity has been calculated, the results from the steady loading model can adjusted. The induced velocities are used to adjust the values calculated by the BET loading model discussed in chapter 4. The induced velocity at each blade station is converted into the blade's frame of reference. This results in an induced velocity component perpendicular and tangential to the blade. The differential forces are calculated by equations 4.1 and 4.2 where

$$U_T = U_{T_0} + U_{T_{ind}} \tag{5.16}$$

$$U_P = U_{P_0} + U_{P_{ind}} \tag{5.17}$$

Equations 4.1 and 4.2 can be represented as

$$dF = \frac{1}{2}\rho c C_{l_\alpha}\left(\alpha_{eff}\right)dr \tag{5.18}$$

where the terms in parenthesis act as an effective angle of attack. An updated effective angle of attack on the blades is achieved is updating U_P and U_T with the induced velocities from tip-vortices at the correct radial and azimuthal stations. This results in blade loading that includes the unsteady effects caused by blade-vortex interaction. These blade loads are used by PSU-WOPWOP to calculate the acoustic results, just as they were in chapter 4. However, impulsive loading values can lead to a sharp increase in the noise output of the rotor. The results of the BVI model are discussed in the next section.

BVI Validation

To validate the BVI model, data from the HART-II test was used [42]. The HART-II rotor was a 40% Mach scaled model of a BO-105 main rotor. It had a constant chord, an NACA23012 airfoil, and a linear twist of -8°. The specifications and flight conditions of the HART-II case are shown in Table 5.1. These rotor specifications and flight conditions were modeled in WOPIt. The HART-II rotor was chosen because it is a well-known and verified study used in aerodynamics and aeroacoustics. The HART-II project studied a rotor in a BVI case and plotted the resulting loading around the azimuth of the rotor. This is an ideal validation case because the rotor can be modeled in the NPS and results can be directly compared at the same radial stations. The blades were modeled as lifting lines and only information that is provided to WOPIt by NDARC was used in the calculations for this case. The tip-vortex geometry was calculated for this rotor then used to calculate the induced velocity on the blade. The resulting unsteady blade loading was non-dimensionalized in order to compare to the measured HART-II blade loading [42]. The comparison of the model output with the experimental data is shown in Figure 5.5 for the radial station $r/R = 0.87$.

Table 5.1: Rotor specifications and flight conditions for the HART-II case

Helicopter Specs	
Number of blades	4
Blade radius	4 m
Chord	0.121 m
Root cutout	0.44 m
Solidity	0.077
Rotation speed	1041 RPM
Flight Conditions	
Advance ratio (μ)	0.15
Shaft tilt	5.3°
Thrust	3250 N
Roll moment	-18 Nm
Pitch moment	-15 Nm

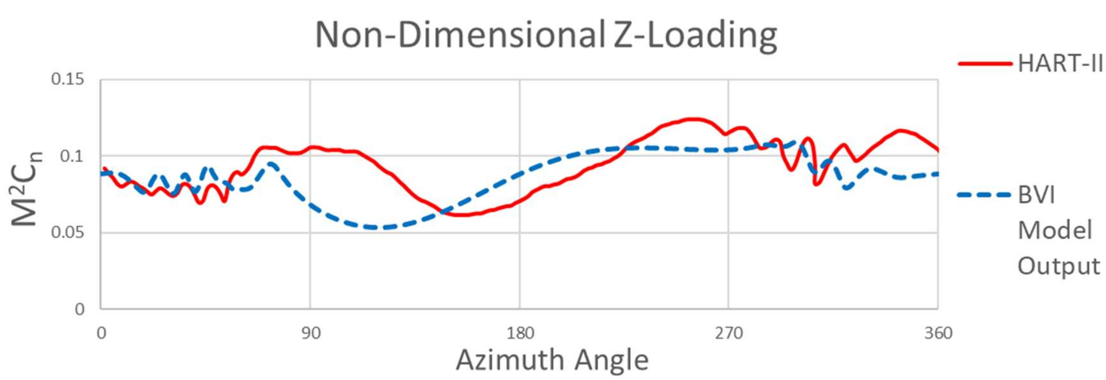

Figure 5.5: Comparison of non-dimensional loading vs azimuth angle for the HART-II experiment and NPS BVI model output at radial station $r/R = 0.87$.

The loading data is represented in non-dimensional form as M^2C_n, or Mach number squared multiplied by the coefficient of thrust normal to the blade. From the comparison it can be deduced that the NPS models are clearly capturing BVI events at the correct locations around the azimuth. While the magnitudes may differ, the corresponding spikes in loading are present at the same azimuth stations in both the experiment and numerical calculations. There are multiple BVI events that occur between $\psi = 0°$ and the advancing side of the aircraft ($\psi = 90°$). These events are captured fairly well by the model. There are a few more BVI events on the retreating side of the rotor between $\psi = 270°$ and $\psi = 330°$. The magnitude of these events are underestimated by the model, however, almost every BVI event that the experiment shows is captured by the model at the correct azimuth station.

Any differences between the model output and experiment may be attributed in part by multiple factors. Interaction angle and distance dramatically affect the strength of an interaction. Furthermore, it is likely that calibration of the constants in the model may be needed to improve the agreement. Because the model is capturing BVI events at the correct azimuth locations, it can be assumed that the ad hoc process of modeling BVI events using Beddoes wake model and Vatistas model to adjust base BET loading has merit. In the future, more validation could be performed to adjust the model for many vehicles and conditions. This is further addressed in chapter 8. The following section describes the results for a BVI test case including the calculated wake geometry, induced loading, and acoustic output.

BVI Results

To demonstrate the BVI model, a simple test case was created in NDARC. It consists of a single helicopter rotor operating at a 6° descent. The aircraft used is identical to the one used in chapter 4 to demonstrate the blade loading model. The flight conditions for this case are listed in Table 5.2 below. This section will describe the predicted wake, the blade loading with and without BVI effects, and acoustic results that include BVI. Finally, the acoustic impact for a range of descent angles is discussed.

Table 5.2: Flight specifications for the BVI test case

Flight Conditions	
μ_x	.23
μ_z	.024
Descent angle	5.96°
C_T	0.0095
Azimuthal resolution	360 stations
Radial resolution	50 stations

The NDARC helicopter performed a simple steady descent case to test BVI. A descent angle of 6° was chosen because it is often near the maximum BVI for many helicopters. To capture the interactions, it is important to have a high enough spatial and azimuthal resolution of the blade loading. Since the wake geometry is calculated at each azimuth step, a very impulsive interaction can easily be missed if the resolution is too low. For example, if a parallel interaction is only visible for a 1 degree slice of the azimuth, but the azimuthal resolution is set to 3° or more, it may be missed entirely. The same holds true if the interaction is only visible for a small fraction of the blade and the radial resolution results in blade stations being too large. For this reason, the BVI loading resolution was set to one degree azimuth and 50 radial stations in this work. The overall execution speed of the system is directly proportional to the resolution, so if a faster speed is desired radial and azimuthal resolution can be decreased. In general it was found that the BVI noise prediction will be representative if there are at least 30 radial stations and 180 azimuthal stations. If BVI is not being analyzed, the necessary resolution to calculate the base loading is not nearly as high.

Unsteady Loading Results

The trailing wake was modeled for the rotor at each timestep. These plots can be animated to show the rotating blades and resulting wakes, however, for this thesis a snapshot was chosen that shows a parallel interaction. A top and side view of the trailing wake calculated by the Beddoes model is shown in Figure 5.6. In this plot the aircraft is flying right to left, and the blades are rotating in the counterclockwise direction when looking from above the rotor. The parallel interaction is occurring on the top right blade approximately 90% along the span. From the side view it is clear that the rotor is operating inside its own wake. This plot includes more trailing wake segments than necessary for a BVI calculation to show off the overall wake shape.

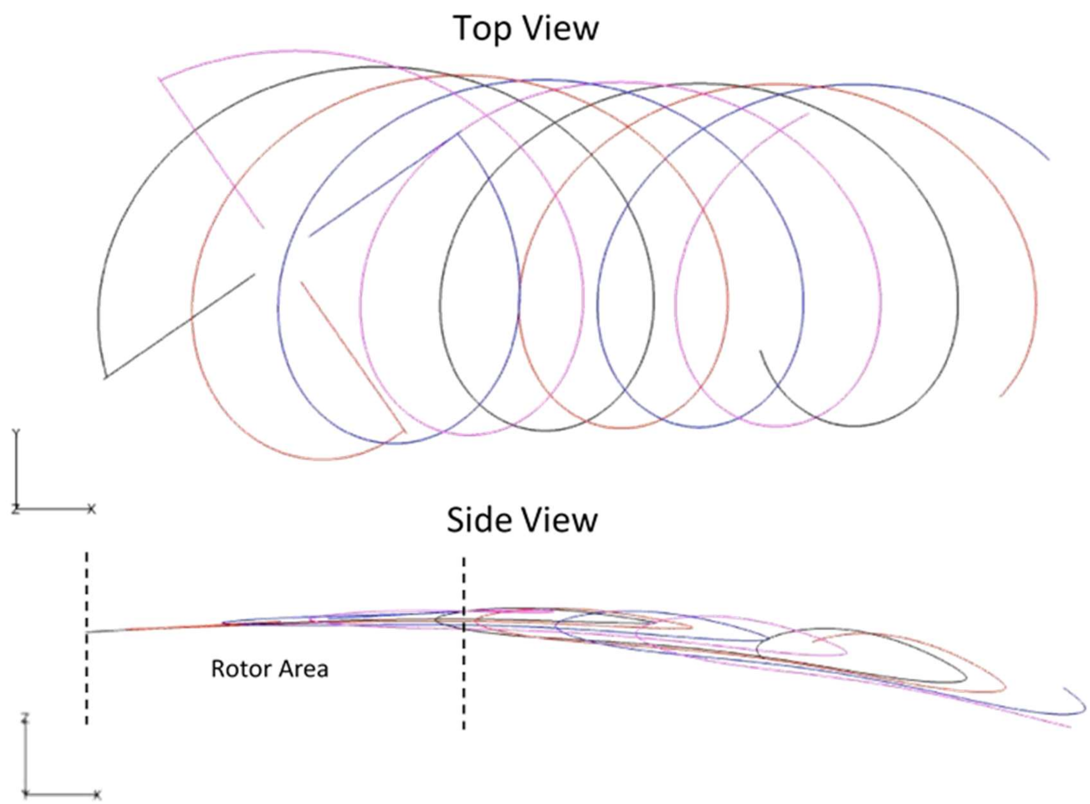

Figure 5.6: Calculated tip vortex geometry for the rotor in the BVI case.

The induced velocity profile perpendicular to the rotor disk is plotted in Figure 5.7. The orientation of this plot is identical to chapter 4 where the aircraft is flying towards the top of the page and the blades are rotating counterclockwise. It is clear that there are distinct interactions on the rotor disk in the first and second quadrants. Most of the rotor disk sees little to no increment in induced velocity profile because only the strongest interactions dominate. These interactions abruptly change from a positive to negative induced velocity as the blade passes over the tip-vortices. These effects are then applied to the blade loading. Figure 5.8 shows a comparison of the base loading in the thrust direction with the adjusted blade loading after BVI. The blade loading has distinct abrupt changes at the same locations of strong induced velocity. An extra plot is included in Figure 5.8 to show the rapid change in loading by adding black contour lines that represent a change in 20 Newtons per meter. Many contour lines close together indicates a rapid change in loading.

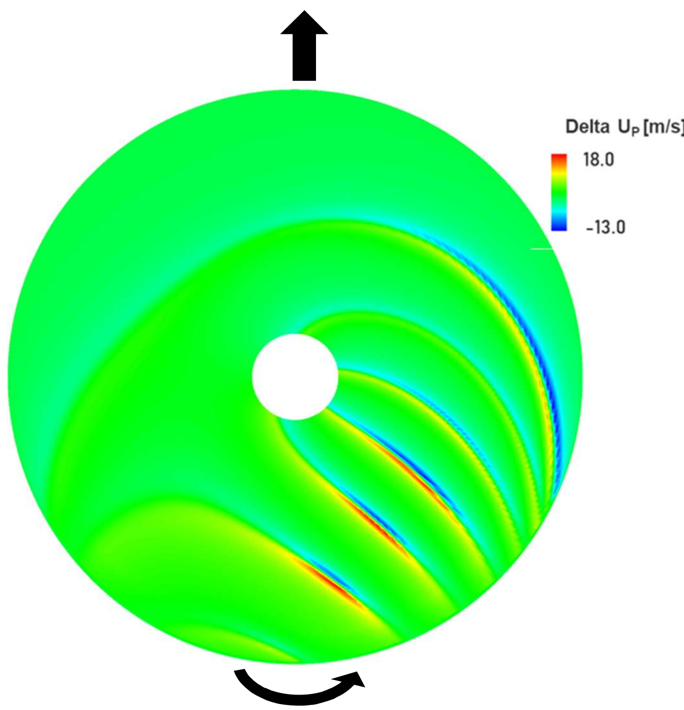

Figure 5.7: Induced perpendicular velocity on the rotor disk due to BVI.

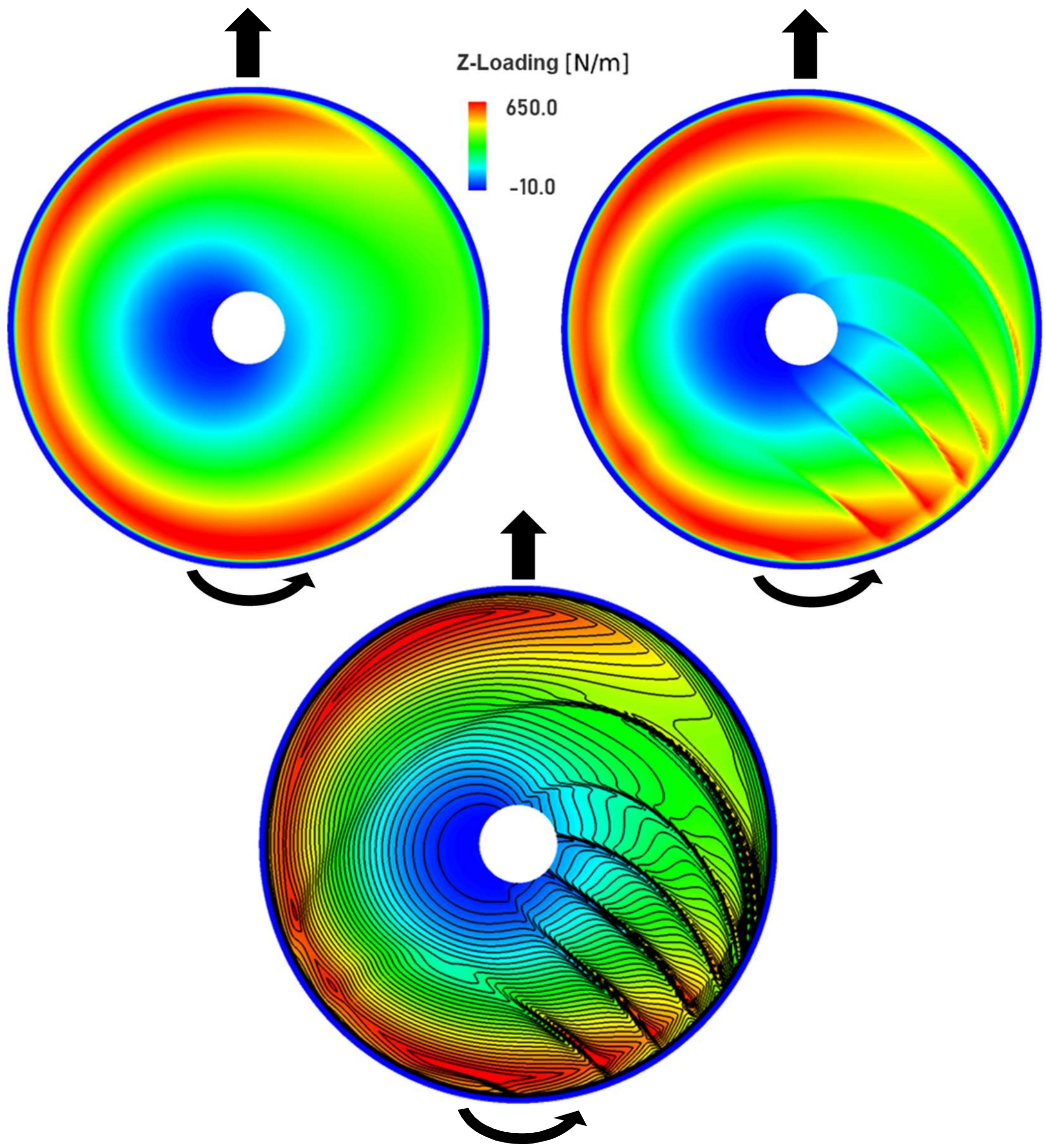

Figure 5.8: Comparison of the base BET Z-loading (top left) with the adjusted blade loads due to BVI (top right). A 32 contour plot (bottom) of the adjusted Z-loads.

BVI Acoustic Results

The adjusted blade loads were used to calculate acoustic results. The loading noise OASPL was plotted onto an observer sphere located 10 rotor radii away from the rotor hub in Figure 5.9. The aircraft is flying in the negative x direction, and this sphere shows results below the aircraft in all directions. Figure 5.10 shows this same plot opened up onto a square grid. This grid can show the entire observer sphere. There are some distortions in the same way that a Cartesian plot maps the sphere. The vertical axis shows the elevation angle, while the horizontal axis shows the azimuth angle. This map is designed such that the plane of the rotor in the flight direction is at the center of the plot. The center vertical line shows the observers that are directly ahead of the aircraft, while the far left and right edges of the map are directly behind the aircraft. Following the center horizontal line results in the observers in the plane of the rotor. Noise is lowest in the plane of the rotor behind the aircraft. The dominant location for noise is found in front of the aircraft out of the plane of the rotor between 40° and 65°. The highest noise levels occur towards the advancing side directly in front of the rotor. This azimuth angle is where the most impulsive blade load interactions occurred.

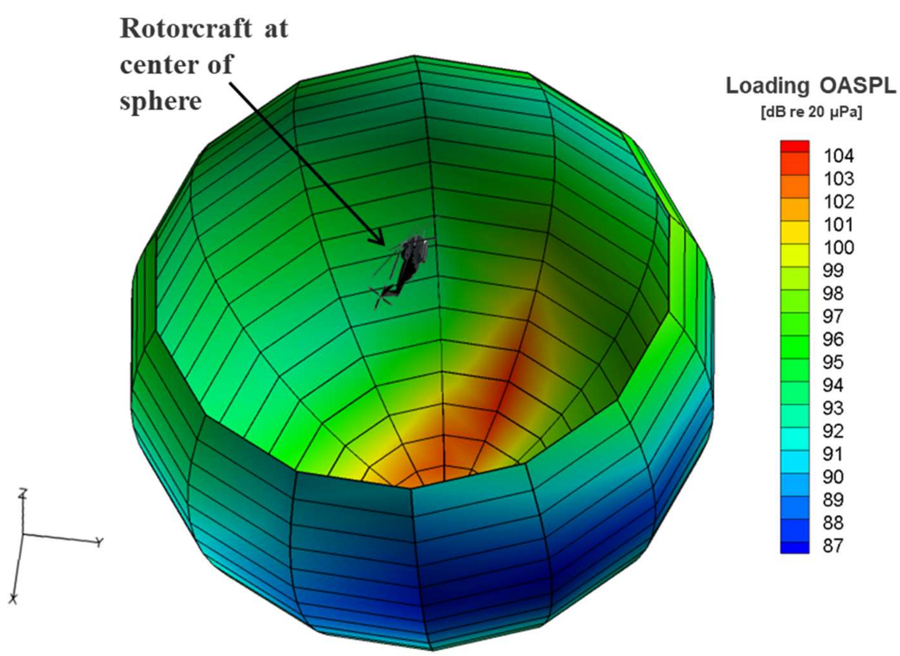

Figure 5.9: Overall Sound Pressure Level for a sphere of observers 10 rotor radii away from the aircraft in the BVI case.

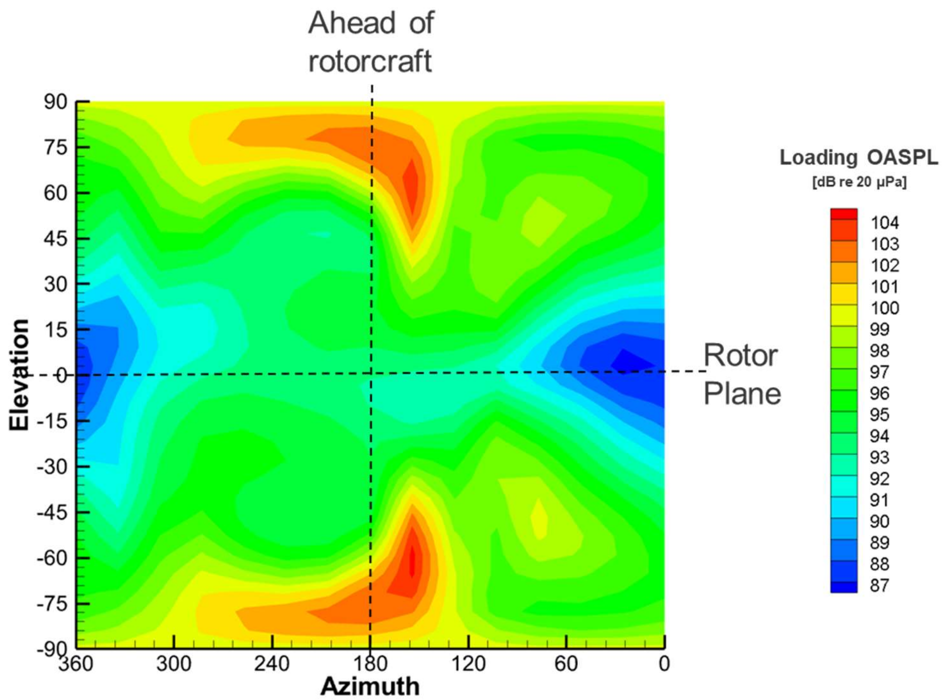

Figure 5.10: Overall Sound Pressure Level for the BVI case mapped onto square grid to show full directivity.

A case study was conducted to study the importance of descent angle when modeling BVI acoustic results. As previously shown in Figure 2.3, the distance that the wake trails below the aircraft is very dependent on the angle of descent. When the z location of the wake geometry is calculated with equation 5.4, μ_z is a dominant factor. To test this, the NDARC helicopter model used in the previous section operated at descent angles varying from level flight to 8° descent. The OASPL was plotted on the same maps used in the BVI test case with an identical scale. This sweep of descent angles is shown in Figure 5.11

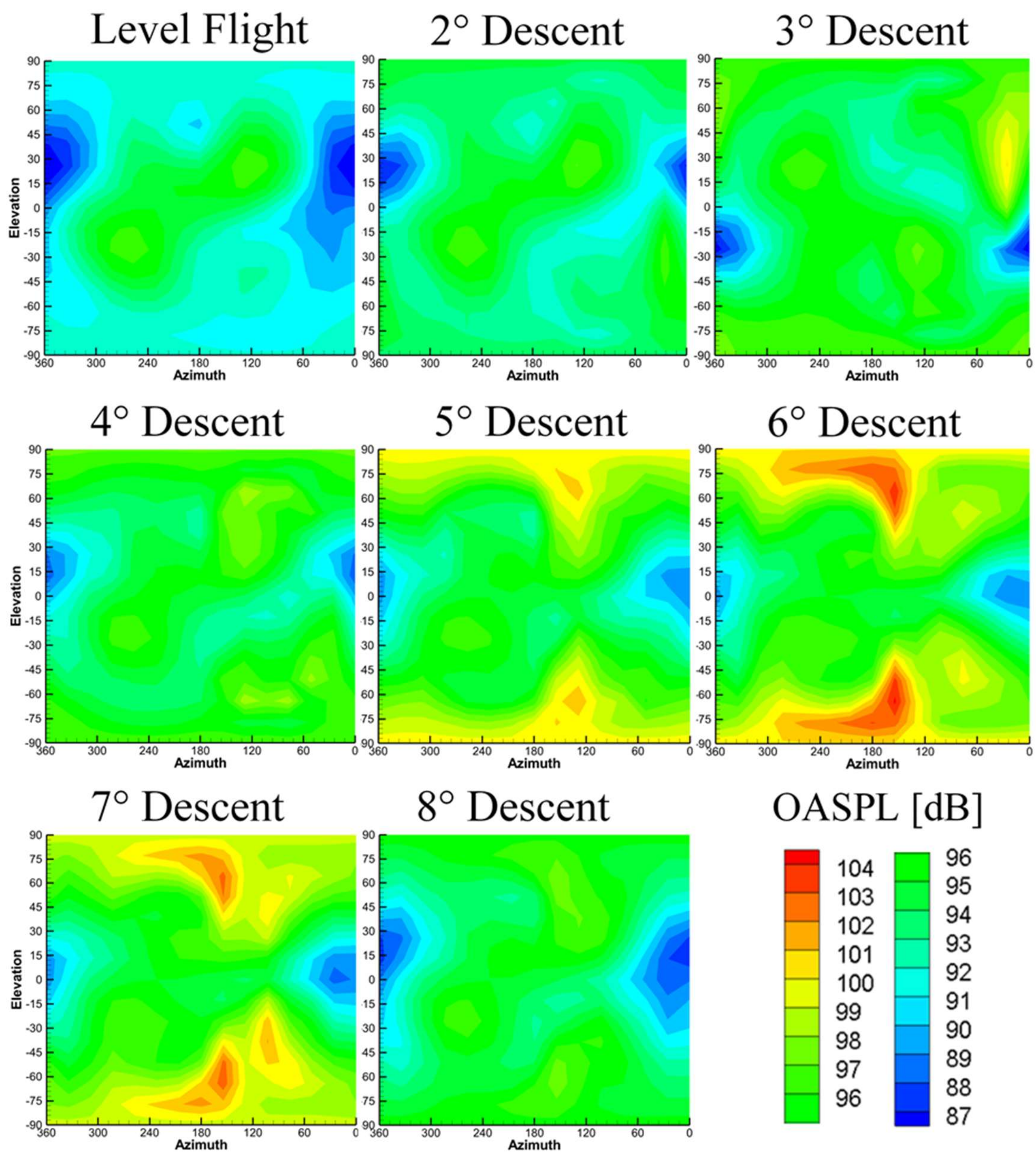

Figure 5.11: Overall Sound Pressure Level plotted for an array of descent angles ranging from 0° to 8° while modeling BVI.

It is clear that that a 6° descent has the highest BVI noise levels for this helicopter. The OASPL is highest for this case. A level flight case sees little to no interactions with the trailing wake. For descent angles of 3° and 4° the effects of BVI begin to appear. The OASPL is higher than that of the previous cases, but there are no dominant bands of very loud signals. At a 5°

descent, there is a clear region in front of the aircraft on the advancing side that has a dominant noise signal. This is further emphasized in the 6° descent case where the noise levels peak. At a 7° descent angle the dominant region is still there. It is not as high as the 6° case, but it is louder that the 5° case for this aircraft. There is also a smaller region of high OASPL on the right side of the aircraft at an angle of 30°-50° below the plane of the rotor that is not seen for the other cases. Finally at an 8° descent, there are no more dominant OASPL regions, as it begins to resemble the 2° descent case. This occurs because the descent is steep enough that the wake is mostly shed above the rotor disk and there are few interactions. Any descent angles steeper than this show no blade-vortex interactions. Similarly, in level flight and shallow descent, the wake is being shed below the rotor so there are not as many locations along the rotor disk where interactions are possible. For the cases of 5° to 7° descent, the rotor is operating very close to the shed wake which maximizes the blade-vortex interactions.

Aerodynamic Interaction

Any upstream disturbance that is ingested into the rotor can create unsteady interactions that affect the blade loading. The previous section described the modeling of a rotor interacting with the tip vortices shed from blades in the same rotor at a previous time. This BVI computation can be used to model the effects of an upstream rotor's wake interacting with a downstream rotor. A similar model could be developed to model the interactions caused by the wake of any non-lifting aircraft component as well.

Rotor-Rotor Interaction

A rotor operating in the wake of another rotor will experience interactions that affect the blade loading and noise output of the rotor. Many new aircraft configurations are being developed that incorporate multiple rotors. These new configurations can have many rotors operating at different angles, leading to interactions that more conventional rotorcraft do not experience. The BVI model that was described above is still applicable in this situation; however, it needs to be expanded. The Vatistas model is still valid and can calculate the velocity induced on a blade due to an upstream rotor's wake. The ad-hoc method of using this induced velocity to modify the BET calculation and increment the steady loading can still be used. However, the tip-vortex geometry is the limiting factor in the case of modeling rotor-rotor interactions. The Beddoes wake model is a prescribed wake model with some distortions applied to mimic the real physics. This means that when the tip-vortex geometry is being calculated for a rotor, the Beddoes wake model has no knowledge of the downstream rotor. In reality the downstream rotor will change the shape of the wake that is shed from the upstream rotor. If the interaction between the downstream rotor and upstream tip vortex geometry, or the wake geometries of the two rotors, can be modeled to make the computation fast, then the current approach can provide the interaction between rotors, or other airframe components and rotors.

A very simple case was created to demonstrate rotor-rotor interactions as a proof of concept. In this case, two identical rotors are operating in the same plane in a tandem configuration. Rotor 1 is directly in front of rotor 2 as shown in Figure 5.12. The aircraft is flying from right to left and the blades are rotating counterclockwise. The wake trailing rotor 1 is being shed above rotor 2. Using Beddoes wake model, this wake will miss the downstream rotor. In reality the inflow of the downstream rotor would pull the upstream wake closer to the blades, dramatically increasing the interactions. To mimic this, the z-location of the tip vortex geometry calculated for the upper rotor is linearly decreased while it is in the area directly above the downstream rotor. Figure 5.12 shows a side view of the tip-vortex geometry without the tip vortex geometry modification, while Figure 5.13 shows the side view of the wake after it is modified. This causes the wake to interact with the blades of the downstream rotor. The induced velocity on the downstream rotor caused solely by the upstream rotor is plotted in Figure 5.14. These disk plots follow the same convention where the rotor is flying towards the top of the page and the blades are rotating counterclockwise.

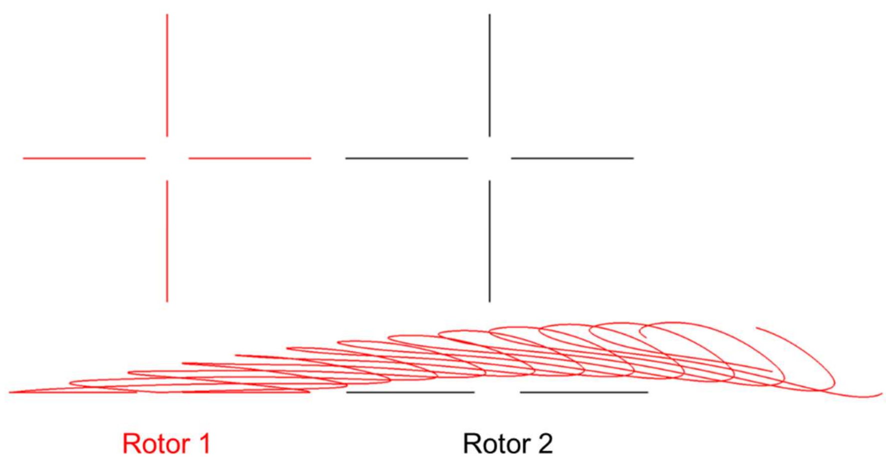

Figure 5.12: Top and side view of the simple rotor-rotor interaction case. The unadjusted wake from rotor 1 is plotted.

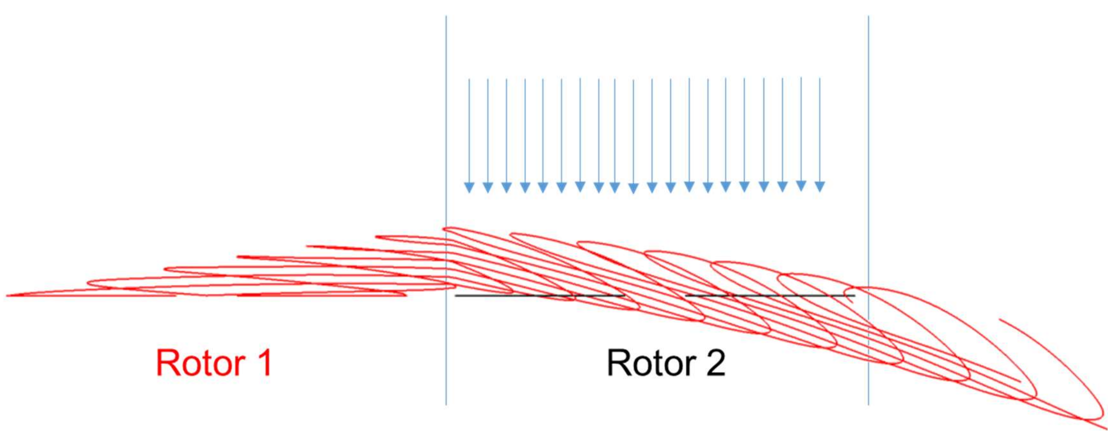

Figure 5.13: Linear adjustment of the wake trailing Rotor 1 due to the inflow of Rotor 2.

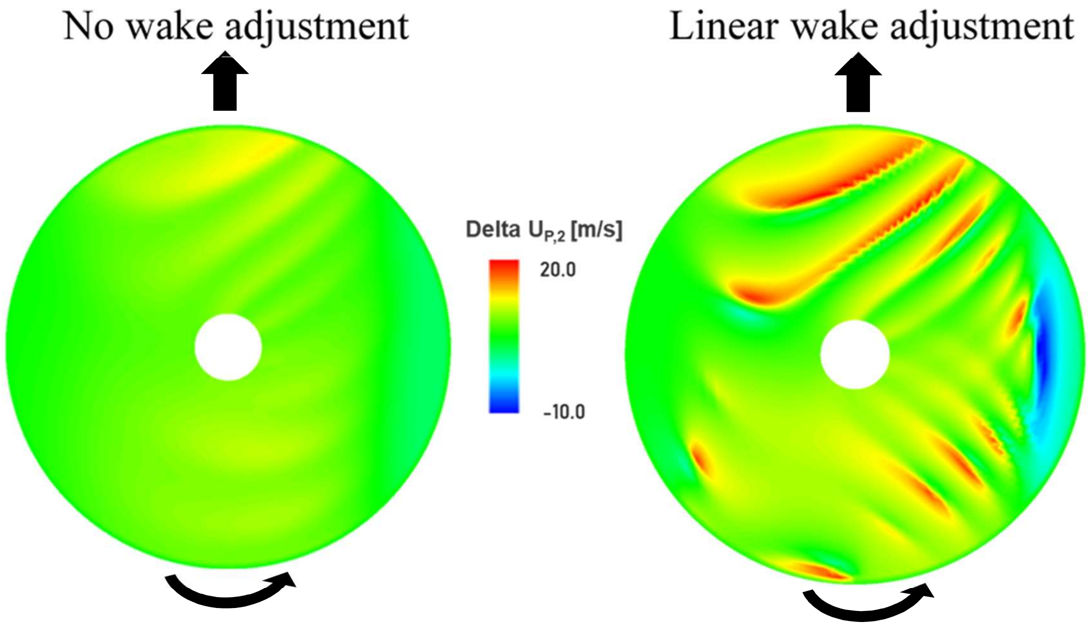

Figure 5.14: Induced velocity on Rotor 2 caused by the wake trailing Rotor 1 compared for the case where the wake was not modified (left) vs when the wake is linearly adjusted downward.

This comparison shows that the added deformation of the wake can play a key role in the resulting unsteady loading. If the tip vortex geometry is calculated with no knowledge of the downstream wake, the system would miss this interaction. In the case where the geometry is not modified, there is minimal interaction with the upstream rotor. With the modification representing the influence of the downstream rotor on the upstream rotor wake, strong impulsive interactions are present. When a rotor is operating in its own wake there are common locations where the interactions will occur on the rotor disk. When the wake is coming from another rotor, the locations of these interactions can occur at any location on the rotor disk. There are strong interactions present all across the rotor disk. It is especially clear that there are strong interactions on the blades in front of the aircraft. These were not present in the cases where a rotor was only interacting with its own wake.

It is important to note that this case was used as a proof of concept and the interaction between rotors and the wake of another rotor needs to be developed further to truly capture unsteady effects caused by rotor-rotor interactions. In this case the wake suddenly jumps downwards which is unrealistic. The vertical distance that the wake is adjusted by needs to be based on a physical metric such as the rotor inflow or lift. It would also need to be validated to ensure that the wake adjustment is sufficiently accurate. Finally, the vortex strength needs to be addressed. If the upstream wake is travelling a long distance before reaching the downstream rotor, the tip vortices will gradually weaken as the vortex cores grow. This would lower the induced velocity on the blades. All of this can be addressed, and this approach can be expanded to capture the interactions between rotors for NDARC aircraft.

Upstream Interactions

Unsteady interactions are not solely caused by spinning blades. Any upstream component of an aircraft can create a disturbance that will be ingested into a downstream rotor. This includes lifting components like wings, or non-lifting components including struts, fuselage, or any other structure. When these structures travel through the air, they leave a trail of displaced air. When this wake reaches the rotor, there will be a temporary change in local lift on the blade. If the interaction results in a rapid or dramatic change in loading, the loading noise may be significantly increased. This occurs because the loading noise is not only dependent on the magnitude of loading, but also its time derivative. A sudden change the magnitude of loading can be impulsive, which could become a dominant component of loading noise.

This project mimics unsteady interactions by using simple models to calculate the disturbance, then adjust the base loading accordingly. This process is appropriate for conceptual design because it is simple and fast, while maintaining a sufficient level of accuracy given the details known early in the design process. This same philosophy can be applied to interactions with other upstream components. The system could use geometry known from the NDARC aircraft configuration and model a “region of interaction” that trails behind the vehicle components. Figure 5.15 shows two examples of this. In the helicopter case while flying forwards, the wake shed by the wing is pushed back towards the rear rotors. In the drone example in descending flight, the shape of the structure will cause a velocity deficit to enter each of the rotors.

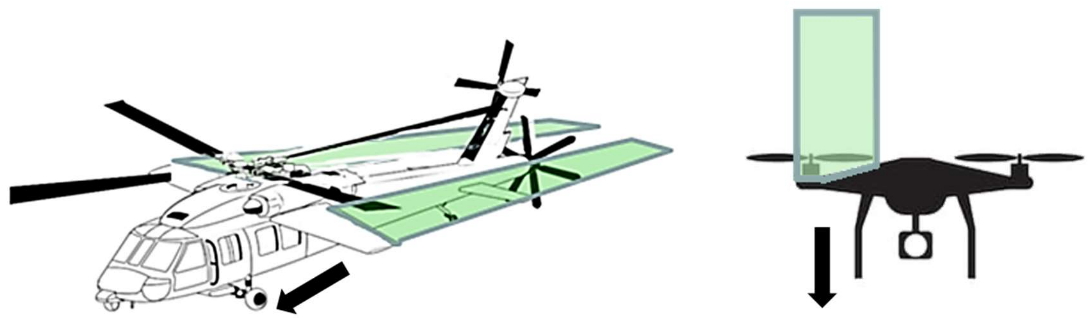

Figure 5.15: Projected area of interaction of wake and downstream aircraft components [9].

Each region of interaction should have a calculated velocity deficit based on the shape and any resulting lifting forces. When a rotor blade is operating in this region, the steady blade loads would be adjusted. This would result in the blade loading that includes unsteady aerodynamic interactions due to upstream aircraft components. The ability to account for the unsteady effects that upstream aircraft components have on the blade loading would be valuable in the NPS.

Chapter Summary

This chapter discussed the models needed to calculate blade-vortex-interaction noise. A prescribed wake model with distortions is used to calculate the tip-vortex geometry that trails behind the rotor. This wake geometry induces a velocity onto the rotor as it operates close to the wake. This induced velocity increments the blade loading model that was discussed in chapter 4. Unsteady loading and acoustic results are shown for a BVI case. This chapter also discussed other upstream aerodynamic interactions. A prototype case for rotor-rotor interaction was shown, and a model for aerodynamic interaction was proposed. The work needed to accomplish these models is discussed further in chapter 8.

Chapter 6

High-Speed-Impulsive Noise

High-speed-impulsive (HSI) noise becomes important when the advancing tip-Mach number of the rotor blades begins to approach 1. The negative peak of thickness noise pulse grows dramatically in amplitude, and the pulse shape changes. This pulse shape is more impulsive, and radiates large amounts of acoustic energy. This extreme thickness noise is called HSI noise [43]. When HSI noise occurs it is often a dominant source that propagates very far down range. For this reason it was important that the system can approximately model the effects that occur.

HSI noise generation is strongly controlled by the Mach number. Small increases in Mach number can lead to a large change in the magnitude and shape of a thickness noise signal. Schmitz showed experimental acoustic pressure results on model-scale and full-scale aircraft [43]. This data is shown in Figure 6.1. As the tip Mach number increases, the peak pressure amplitude increases. After Mach 0.84, the peak pressures increase at a much higher rate. At higher Mach numbers, a small increase in Mach numbers can lead to a large change in peak pressure amplitude. The HSI effects on the acoustic pressure waveform shape can be seen in the model-scale and full-scale acoustic signals. At lower tip Mach numbers the pulse shape is symmetrical, and the amplitude is lower. As tip Mach number increases, pulse shape becomes sheared. In both cases the higher tip Mach number cases have very impulsive shock-like pulse widths. These high amplitude impulsive signals are indicative of the impacts of HSI noise.

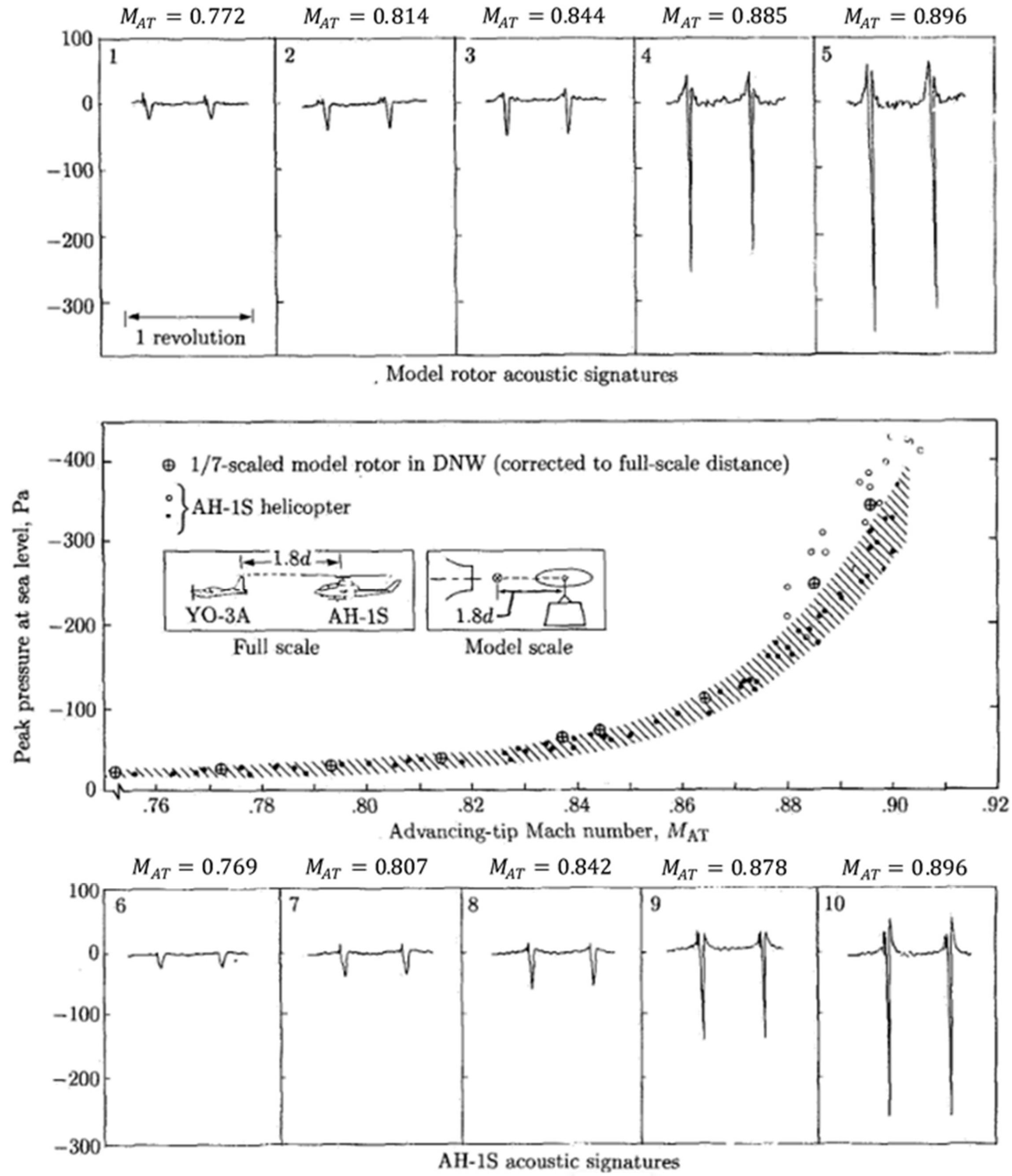

Figure 6.1: Acoustic pressure for varying advancing tip Mach numbers (M_{AT}) for model-scale and full-scale aircraft [43].

The pressure amplitude and shape of the acoustic pressure signal are important for determining the noise output for the rotor. Higher amplitudes and impulsive waveforms both increase the HSI noise output. Using thickness noise theory alone would under-predict the amplitude and the pulse width. Schmitz compared linear theoretical thickness prediction with experimental results for varying tip Mach numbers on a hovering rotor [43]. This comparison is shown in Figure 6.2. At $M_T = 0.80$ the theory under-predicts the peak by a factor of two, while the pulse width is still fairly symmetrical. At $M_T = 0.88$ the experimental pulse is beginning to become more asymmetric. At the higher tip Mach numbers, the pulse starts to approach a saw-tooth pattern. After the pressure peak, the signal quickly spikes to a positive peak. This impulsive saw-tooth pattern generates high intensity, high frequency noise [43]. The theory does not capture the dramatic increase in magnitude, or the steepening of the wave.

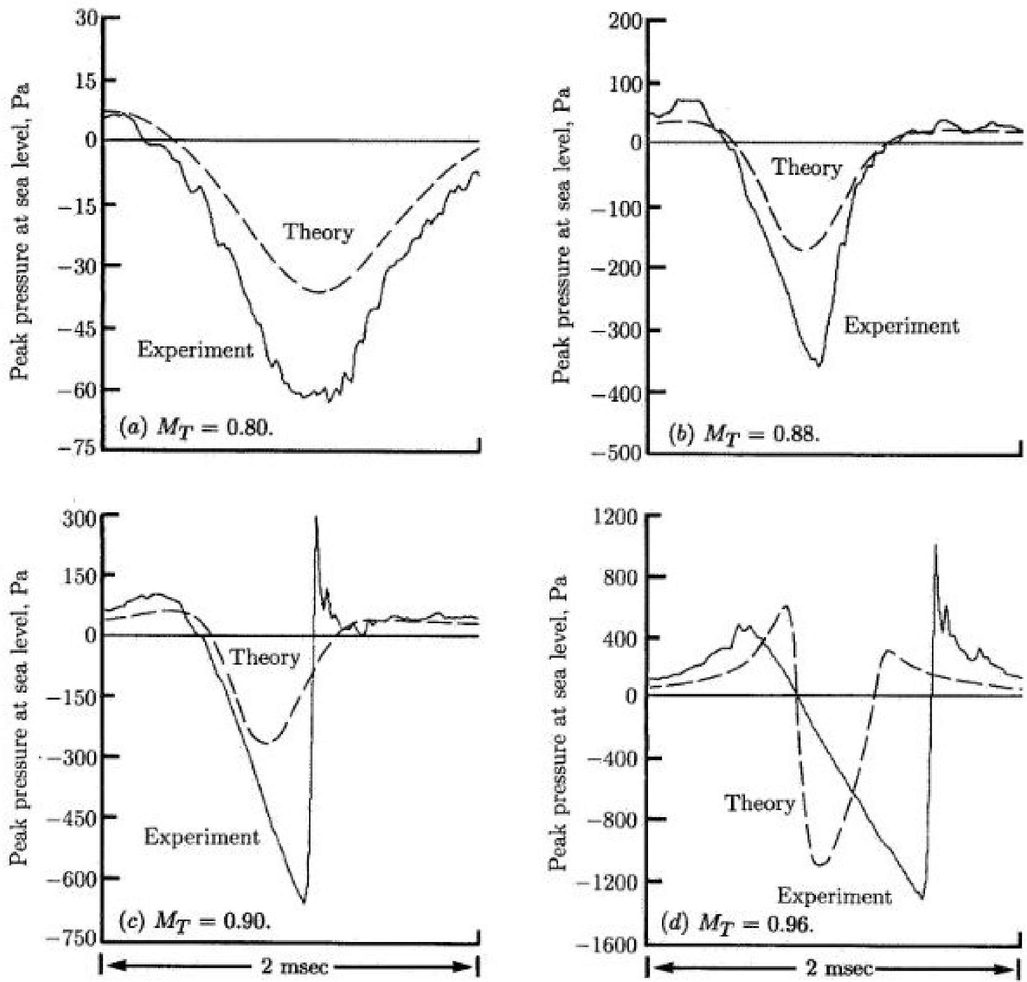

Figure 6.2: Comparison of theoretical an experimental time histories for an in-plane observer 3.0 rotor radii away from the blade at varying tip Mach numbers [43].

Since HSI noise is a dominant, impulsive noise source that has a significant impact on the noise output of the rotorcraft, it is important that the NPS can model HSI noise. In general, HSI conditions should be avoided, but the NPS needs to include a reliable approach to determine these conditions. This will allow a designer or optimizer to make choices with the knowledge of HSI conditions. However, modeling HSI noise is often very computationally expensive. CFD models are often used model the complex nonlinear interactions that occur around a rotor operating in the transonic regime and propagate them to the far-field. This computationally expensive level of detail is incompatible with conceptual design. A simple empirical model that can provide a realistic HSI waveform shape to predict the impact of HSI noise is ideal for the NPS.

In this work, an HSI model (ShearIt) is designed to mimic nonlinear affects that occur when the rotor blades approach a transonic tip speed. As the tip Mach number increases, the peak amplitude increases, and the wave becomes asymmetric. An empirical model has been developed to capture the HSI effects by amplifying the signal to match the appropriate peak pressure, shearing the signal to match the appropriate shape, and shock fitting the signal when appropriate. Figure 6.3 shows the three-step process that the present HSI model uses to mimic HSI noise.

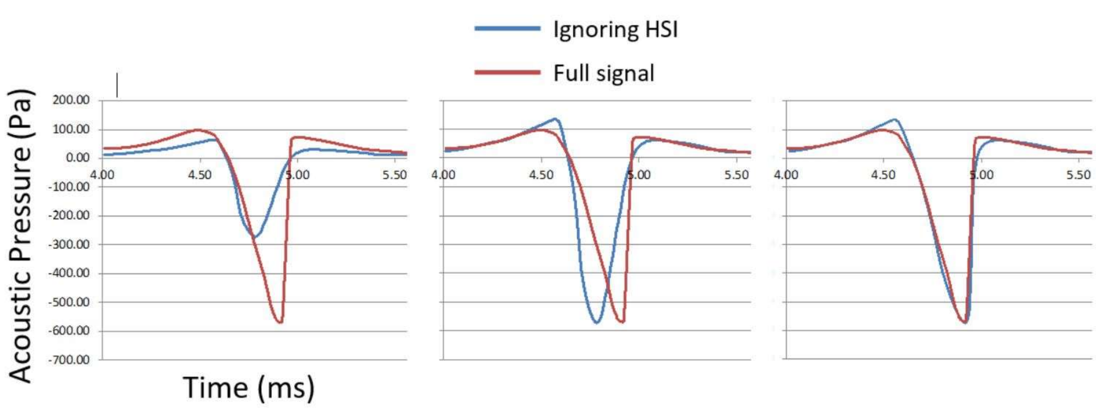

Figure 6.3: The signal adjustment process for HSI post-processing. The original signal (left) is amplified (middle) then sheared (right) to match the full signal (Figure 3.8 repeated for convenience).

In 2016 Sharma [9] showed that this approach is viable. Sharma's simple model used empirical equations based on tip Mach number to adjust the signal produced by PSU-WOPWOP. The peak amplitudes and wave shapes generally matched data, and the shock-fitting algorithm inserted shocks at the correct location in the signal. The 2016 HSI model was not robust, and did not take out-of-plane observers or radiation distance into account when predicting HSI noise. This work developed empirical relations using the Mach number in the radiation direction of the observer (M_r) and radiation distance (r_{obs}) to amplify and shear the signal. A small modification was added to PSU-WOPWOP to provide M_r and r_{obs} to ShearIt. These variables are calculated in PSU-WOPWOP, and are dependent on observer location, flight condition, and rotor orientation. A more robust and efficient shock-fitting algorithm was implemented in the ShearIt code as well. The new model can predict HSI noise for an aircraft with multiple rotors for observers at any location in or out of the rotor plane. The following section describes the development of the empirical equations used in this model.

HSI Model Development

The post-processing HSI model was developed using data from Baeder et al. "A Computational Study of the Aerodynamics of Rotors in Hover" [30] as the data source for the empirical model. This study directly computed the acoustics by CFD in the plane of the rotor for a 1/7th scale model of a UH-1H rotor. The blades were straight, untwisted, and rectangular, with a radius of 1.045 meters and a chord of 0.0762 meters. Baeder et al. collected the acoustic pressure on a CFD grid that focused its resolution on the travelling acoustic wave. The data was collected in hover conditions for tip Mach numbers varying from 0.6 to 0.95.

Baeder's rotor was modeled for each of the conditions in the study, and PSU-WOPWOP was used to calculate the acoustic pressure results without any HSI effects. This would serve as a baseline acoustic pressure, which would be modified to match the data. The PSU-WOPWOP results were scaled and sheared to best match the CFD data's acoustic pressure time history and spectrum data. The acoustic pressure signal and spectrum data were overlaid with the results from Baeder et al., and the amplification and shearing functions were adjusted until the signals had similar magnitudes, wave form slopes, and shock locations. The results of the HSI model predictions compared to the data from Baeder et al. are shown in Figure 6.4 for the baseline case for tip Mach number 0.95. For each tip Mach number, values for amplification factor and shear factor were recorded. These results are shown in Table 6.1. These values were used to develop the empirical equations for amplification and shock fitting. These empirical relations are represented by equations 6.1 and 6.4 and plotted in Figure 6.7 and Figure 6.9, respectively.

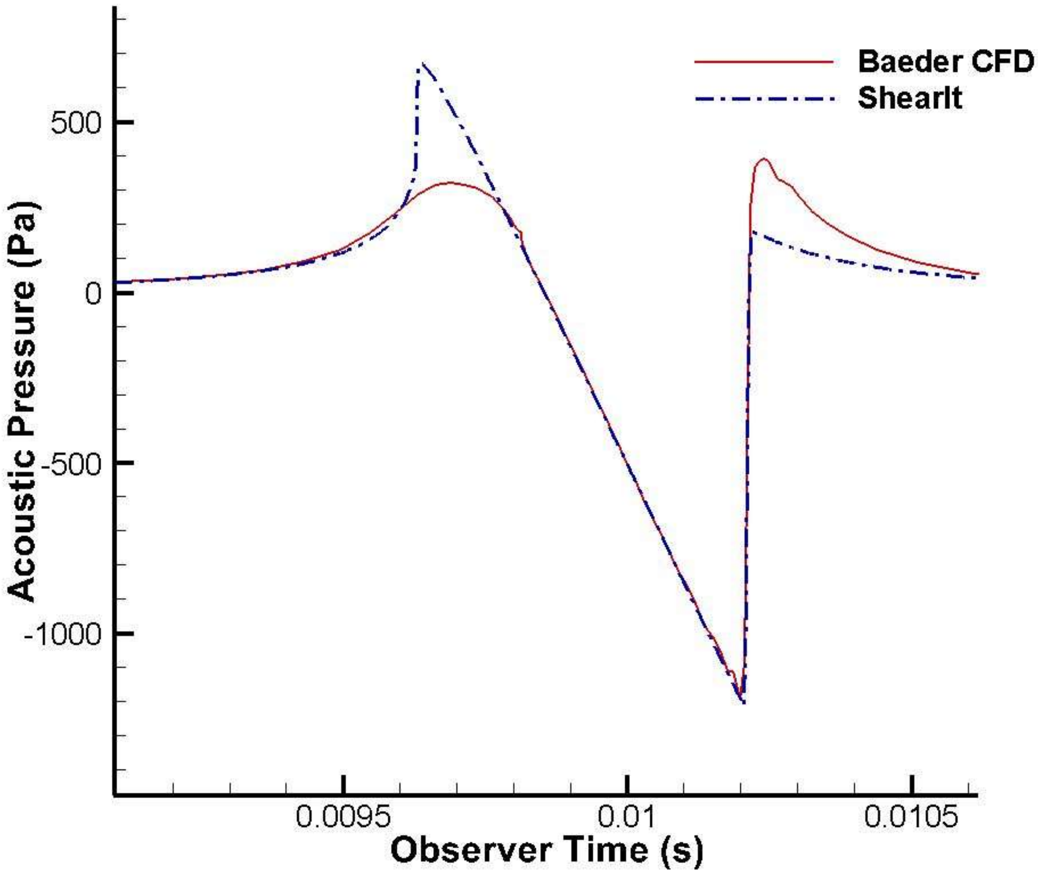

Figure 6.4: Acoustic pressure time history comparison of shock-fitting results with Baeder et al. CFD for a tip Mach number of 0.95.

Table 6.1: Amplification factors and shear angles that result in a good fit to the data at each tip Mach number

Tip Mach	Amplification	Shear Angle [rad]
0.6	1.134	0.0
0.7	1.175	0.0
0.8	1.222	0.0
0.85	1.374	0.0
0.88	1.814	0.70
0.9	2.35	1.03
0.925	2.14	1.072
0.95	2.3	1.09

The HSI model equations for amplification and shearing were obtained by fitting curves to this data. Piecewise curves were used to capture as much of the trends as possible. For values of tip Mach number higher than 0.95, the curves were extrapolated based on the trends. This model does not explore any blade tip speeds greater than Mach 1. The equations used to calculate HSI effects are derived in the following paragraphs.

Baeder et al. focused on the HSI effects in the plane of the rotor. However, NPS needs the capability to model the effects for any observer locations. Thus, the amplification and shear factor equations depend on Mach number in the radiation direction, M_r, to modify the signal. M_r is calculated by taking the dot product of the Mach number vector of the blade tip, with the unit vector that points to an observer's location. As shown in Figure 6.5, this is maximum in the plane of the rotor, ahead of the rotor, and minimized directly below the rotor. As an observer is further from the plane of the rotor, the effects of HSI become less important. The empirical equations used to amplify and shear the signal are based on the maximum M_r value around the rotor disk.

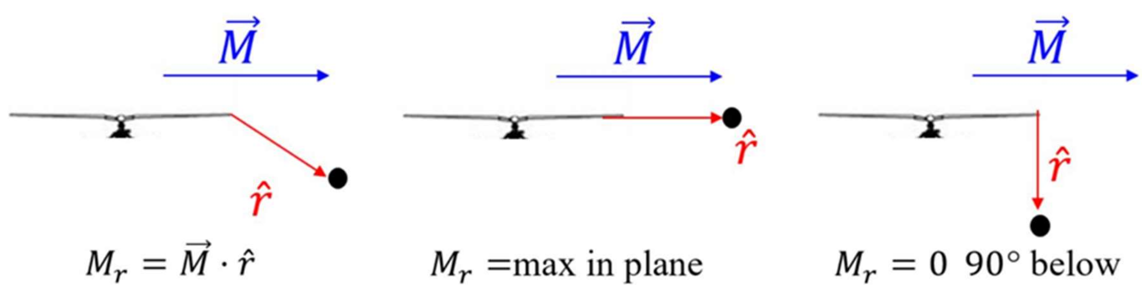

Figure 6.5: Demonstration of Mach number in the radiation direction (M_r).

To ensure that M_r is a suitable basis for the model, data was collected from out-of-plane observer locations on the CFD grid from Baeder et al. Values of acoustic pressure vs M_r were recorded for varying observer locations, as well as varying Mach numbers. This data is plotted in Figure 6.6, with each hover tip Mach number being represented by a different color. The rightmost point of each color would signify an in-plane observer at that Mach number, while all others are out of plane observers at that Mach number. (i.e., the rightmost green point is an in-plane observer at Mach 0.925, while all other green points are out of plane observers for the 0.925 tip Mach number.) The overall pattern shows that regardless of hover tip Mach number, pressure behaves similarly for observers that have a similar M_r. An observer in-plane for a hover tip Mach number of 0.88 (rightmost orange) is nearly identical to an observer for the Mach 0.925 case that has an M_r of 0.88. It is worth noting that the CFD grid was very dense in plane, and the grid that was furthest out of plane became quite coarse. These out-of-plane points are where the values deviate from the curve the most (leftmost for each color). This comparison shows that, it is reasonable to use M_r as the proper variable for the NPS to model HSI effects.

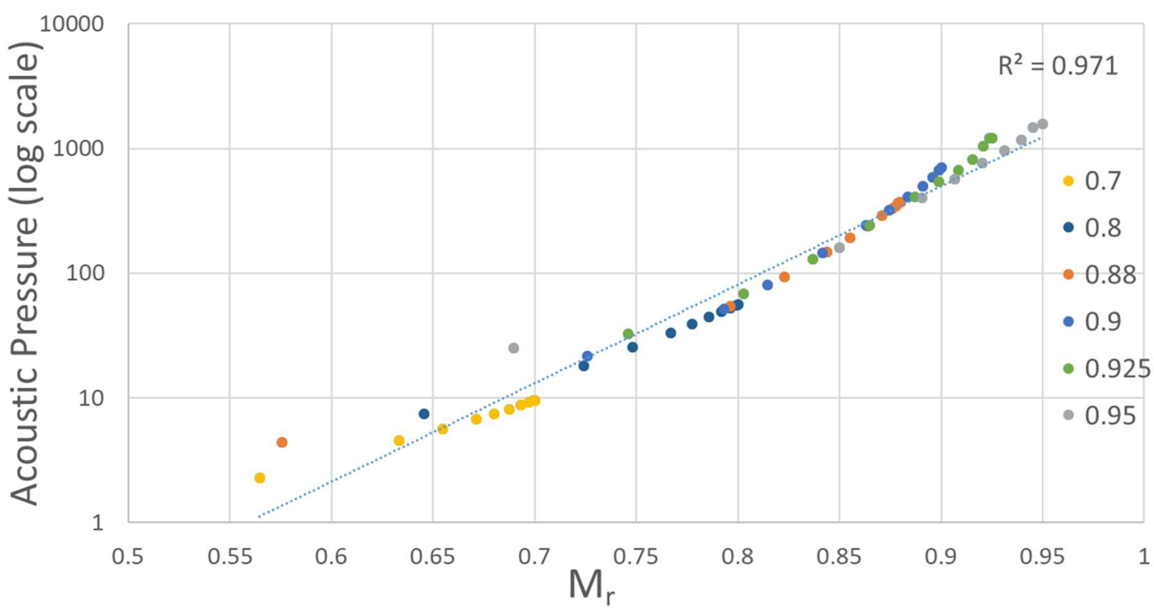

Figure 6.6: Peak acoustic pressure values at varying tip Mach numbers for an array of in-plane and out-of-plane observers.

HSI Model

The model adjusts the signal in three consecutive steps: amplification, shearing, and shock fitting. First, the entire pressure time history is amplified by a scale factor. The amplification factor is calculated by

$$AMP = \begin{cases} 1 + 0.1800844M_r & if\ M_r \leq 0.687 \\ 42.504M_r^3 - 80.822M_r^2 + 50.869M_r - 9.4594 & if\ M_r > 0.687 \end{cases} \quad (6.1)$$

$$p'_{amp} = p' * AMP, \quad (6.2)$$

where M_r is the maximum tip Mach number in the radiation direction over a full revolution. The function is plotted versus M_r in Figure 6.7. The piecewise nature of this function is to smoothly combine the data that was outside of the range of results from Baeder et al. (below Mach 0.6) with the data that was fit by the model. At lower tip Mach numbers, amplification is not needed, so the function starts at 1. As the Mach number increases, the necessary amplification increases. It is important to note that this scale factor take into account shearing and shock fitting the signal as well. When the system inserts a shock into the signal, there may be a loss in amplitude. Figure 6.8 shows an example of this. After the shock is inserted, the final amplitude is lower than the pre-shock amplitude. Thus, the model takes this into consideration and over-amplifies the signal to reach the target amplitude.

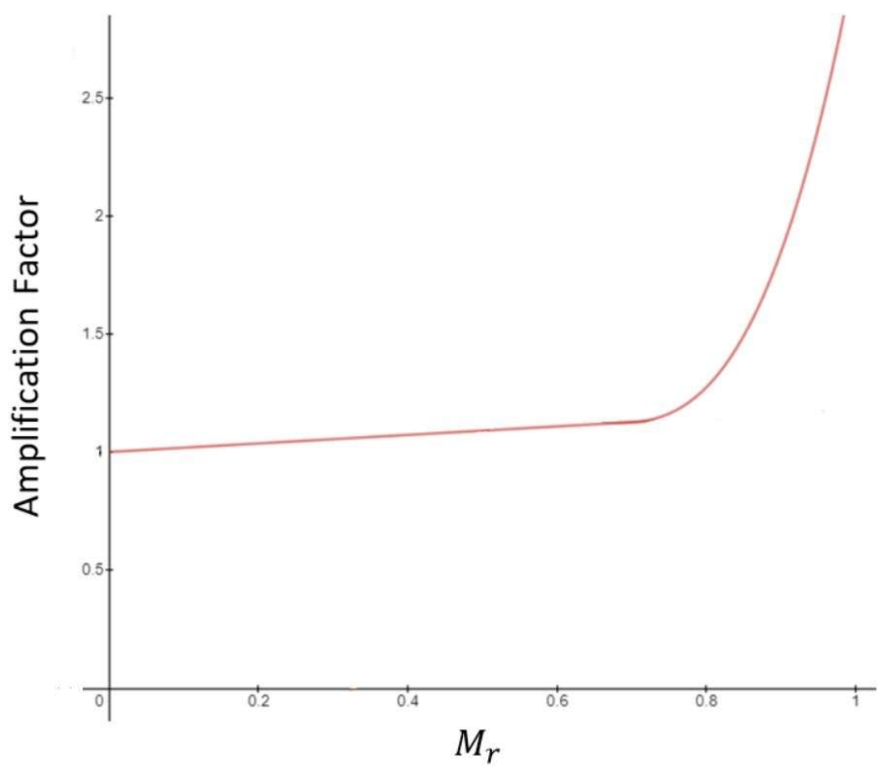

Figure 6.7: Amplification factor as function of M_r.

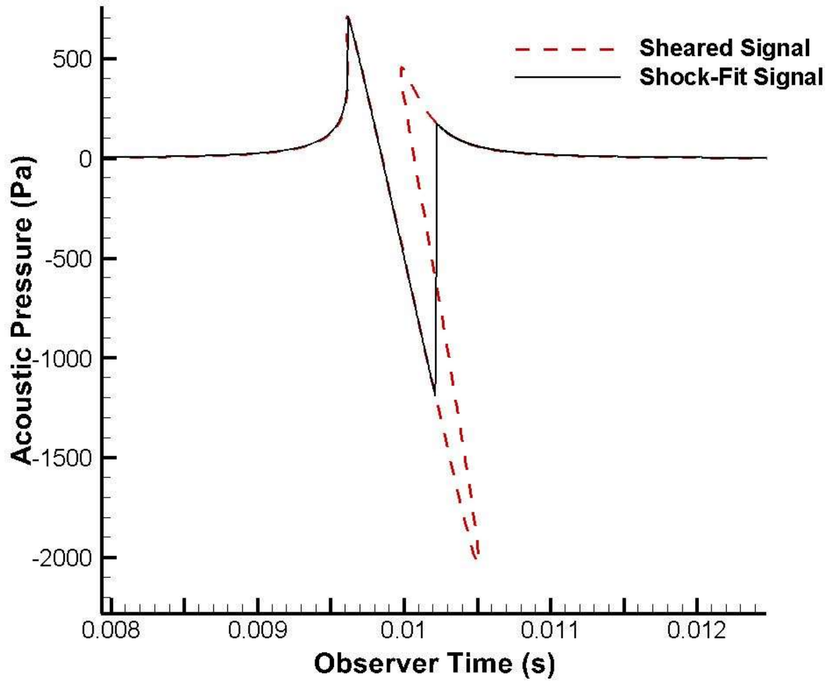

Figure 6.8: After the shock-fitting algorithm finishes, the signal is often at a lower amplitude. Increasing shear that is applied to a signal leads to a greater decrease in amplitude.

Next, the signal is sheared by an angle. However, the model that calculates this angle uses non-dimensional parameters for time and pressure. The non-dimensionalizations are calculated by

$$\tilde{p} = \frac{p}{\rho c^2}, \quad \tilde{t} = \frac{t\Omega}{2\pi}, \tag{6.3}$$

where pressure is normalized by density and the speed of sound, and time is normalized by the blade period. These non-dimensional numbers produce more friendly numbers for shear angle that were easier to work with to fit the models. The shearing angle is calculated (in radians) by

$$\gamma_s = \begin{cases} .0006e^{8.0675M_r} & if\ M_r \leq 0.87 \\ 914.12M_r^3 - 2645.3M_r^2 + 2548.9M_r - 816.7 & if\ M_r > 0.87 \end{cases} \tag{6.4}$$

where r is the radiation distance. This function is plotted versus M_r in Figure 6.9. Shearing is not important for lower Mach numbers, so the shearing angle function starts at 0. Between Mach 0.85 and 0.925 there is a steep increase in the shear of the signal. After Mach 0.925 it begins to flatten off and then decrease. The curve fit used to describe the shearing angle continues decreasing after Mach 0.95 before flattening off again. This model was not built with any data above Mach 0.95, so any case greater than that is not verified. However, it is rather unlikely that the tip Mach would exceed Mach 0.95 in typical conditions. It is important to note that unless the x and y axes are identical, the amount that a signal is sheared by will not directly translate to an angle in degrees. For example, the sheared plot in Figure 6.4 may look bent at a 45 degree angle, but the time range is much smaller than the pressure range, therefore the angle used in the model would be much different.

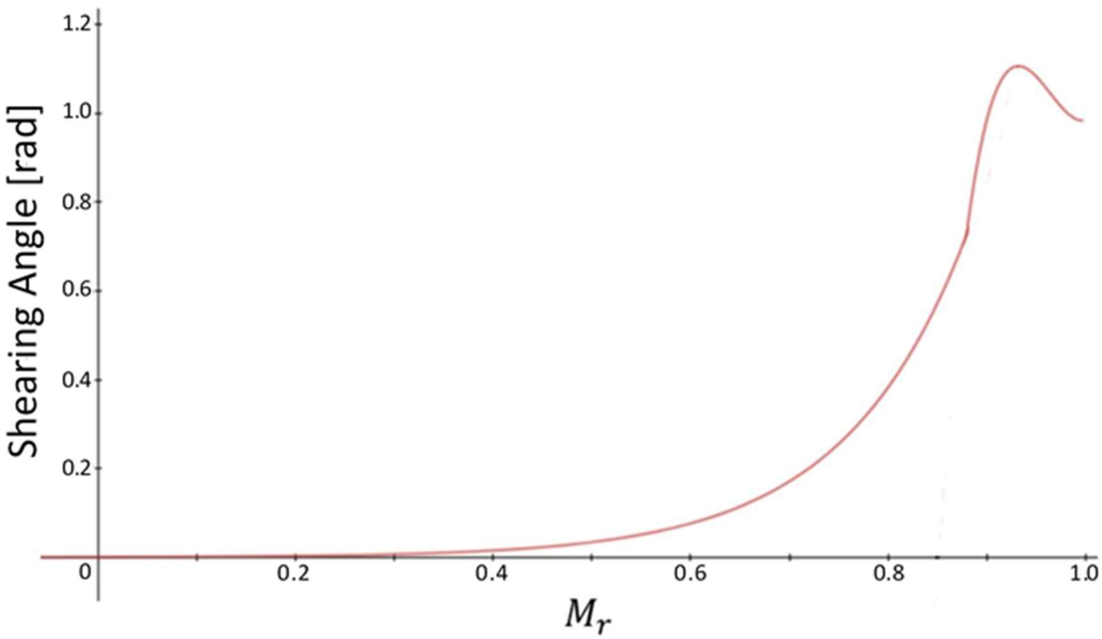

Figure 6.9: Shearing angle as a function of M_r.

The HSI model developed here also takes distance effects into account. As a signal propagates, it loses amplitude as a result of spherical spreading. The local pressure of the signal is inversely proportional to the distance it has travelled. It can be calculated with $p = \frac{A}{r}$ where A is the pressure amplitude of the signal when it was released. In addition to changing the amplitude as the signal propagates, given enough distance (and absent dissipative processes), any signal will shock due to wave steepening effects. To mimic this, the shearing angle is applied to the amplitude of the pressure signal when it was released. This means than regardless of how far the signal has propagated, the same shearing angle is applied. Because the time shift is the result of an angle, the severity of how much any given time step is sheared is directly proportional to the pressure amplitude at that point. If distance effects were not included in the model, then a signal that has propagated a far distance (thus having a smaller amplitude) would be sheared by a smaller amount. Applying the shearing angle to the amplitude ensures that even at lower tip Mach numbers, a signal will shock with a great enough distance. Figure 6.10 shows an example of a lower tip Mach number shocking due to a large radiation distance. The effect of distance on the shearing angle needs to be further validated, as its effect may be too strong. This is discussed further in chapter 8.

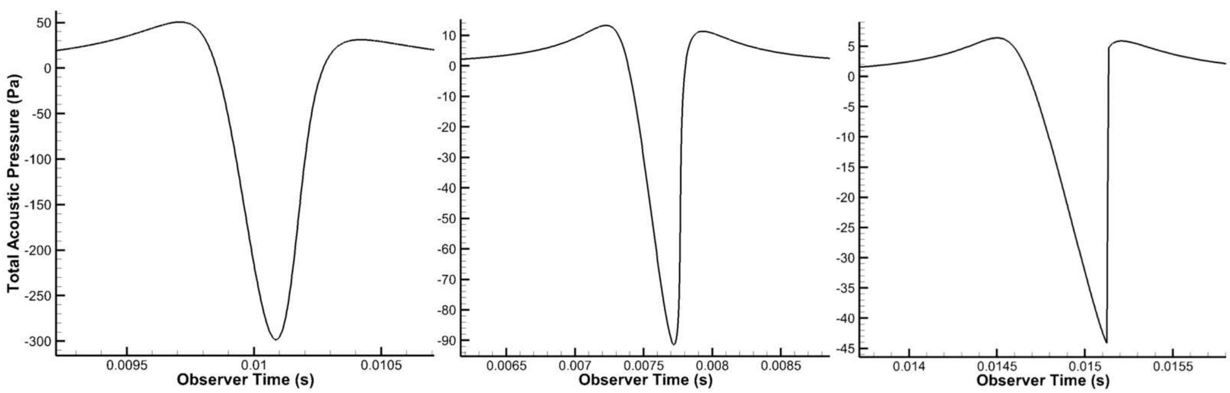

Figure 6.10: Noticeable distance effects in the post-processed acoustic pressure time history for a rotor at Mach 0.88 for an in-plane observer at varying distances. Left to right: 3.09, 10, 20 rotor-radii away.

The effect of the shearing angle is found at each time step of the non-dimensionalized signal, using

$$\delta t(r, M_r) = \tilde{A} \tan \gamma_s(M_r) * \frac{r}{r_0} \tag{6.5}$$

$$\tilde{t}_{shear} = \tilde{t} - \delta t \tag{6.6}$$

where $\tilde{A} = \tilde{p}r$ is the non-dimensional pressure amplitude at the source, and r_0 is the calibration distance that was used to develop the model. This change in time is applied to every time step of the non-dimensional signal before it is re-dimensionalized, resulting in the completed sheared signal. However, this shearing results in a signal with uneven time steps, so the signal is then resampled back to even time steps which is needed for PSU-WOPWOP.

Finally the signal is shock fit if necessary. The system determines that a signal needs to be shock fit when it is multi-valued (i.e., one value of time has multiple values of pressure) as shown in Figure 6.11. This is unrealistic in nature, so when this occurs, the system inserts a discontinuity into the signal to model a shock. Inserting a discontinuity into any location of the triple-valued signal results in two enclosed shapes between the curve and the discontinuity, as shown in Figure 6.12. Whitam's theory of nonlinear propagation proposed that inserting a shock into the signal should be done at a location that causes the two shapes to have equal areas [44].

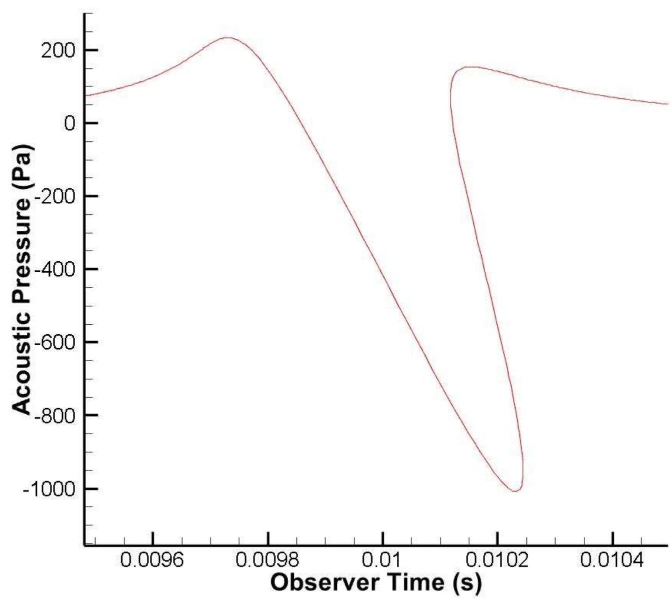

Figure 6.11: Generic triple-valued acoustic pressure time history signal after amplifying and shearing. The shock-fitting algorithm will fix this.

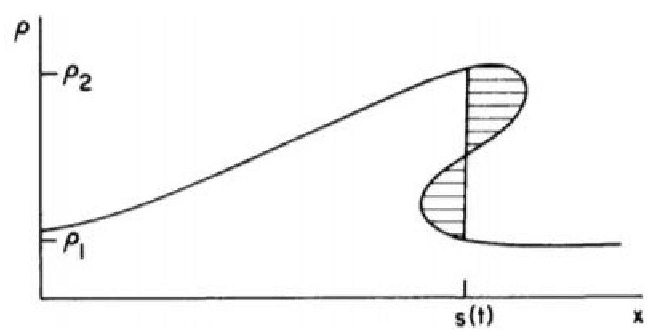

Figure 6.12: Inserting a discontinuity into the signal resulting in equal areas [44].

The algorithm that inserts this shock steps through every timestep in the signal. If the time value for any point is lower than the point that came before it $(t(i) < t(i-1))$, the signal has begun to curve back on itself. This indicates that signal needs to be shock fit. From this point on, the system steps forward while looking for the point where the signal curves forward again$(t(i) > t(i-1))$. These points are denoted by t_{back} and $t_{forward}$ in Figure 6.13. While marching forward, it is also computing an area calculation for the lower curve as shown in Figure 6.14. When the system reaches $t_{forward}$, it has computed the maximum area for the lower curve, shown in Figure 6.15.

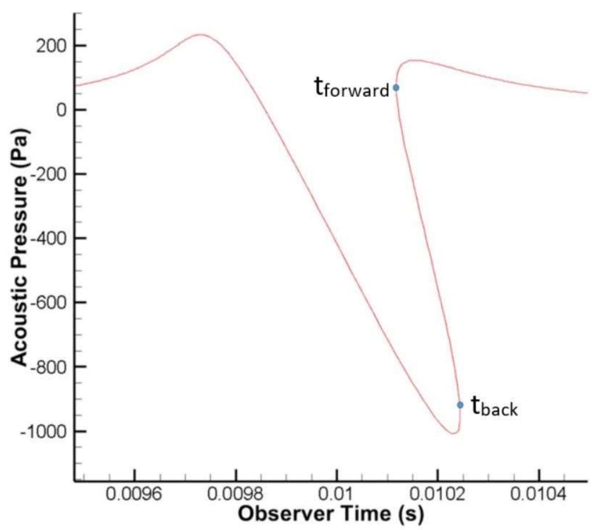

Figure 6.13: Time steps where the signal curves back on itself and where the signal begins to curve forward again.

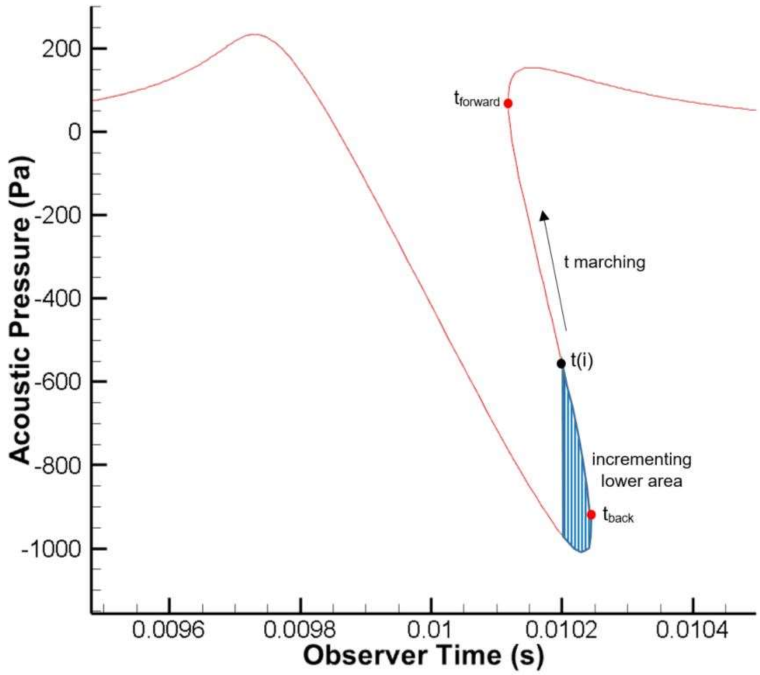

Figure 6.14: After reaching t_{back} the system marches towards $t_{forward}$ while calculating area for the lower curve.

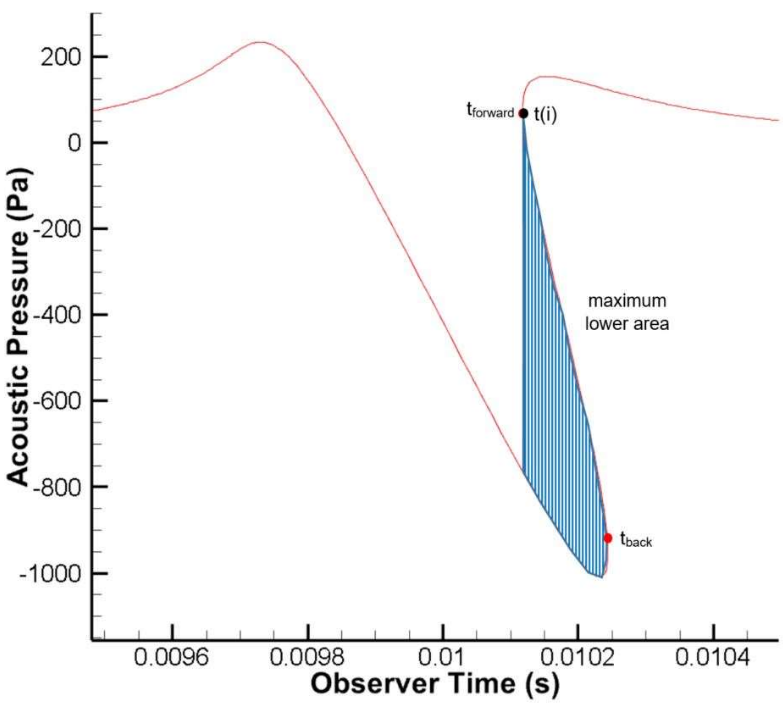

Figure 6.15: Once the signal reaches $t_{forward}$ the maximum lower area has been calculated.

From here, the system marches forward computing the upper curve area, while decrementing the lower curve area, which is illustrated by Figure 6.16. This marching stops upon reaching the time step that provides equal areas. The "top" of the shock will be inserted at this time step, and the algorithm marches backwards to find the intersection point to act as the "bottom" of the shock. Any points that occurred between the intersection point and the shock time will be discarded, resulting in a shock-fitted signal as shown in Figure 6.17.

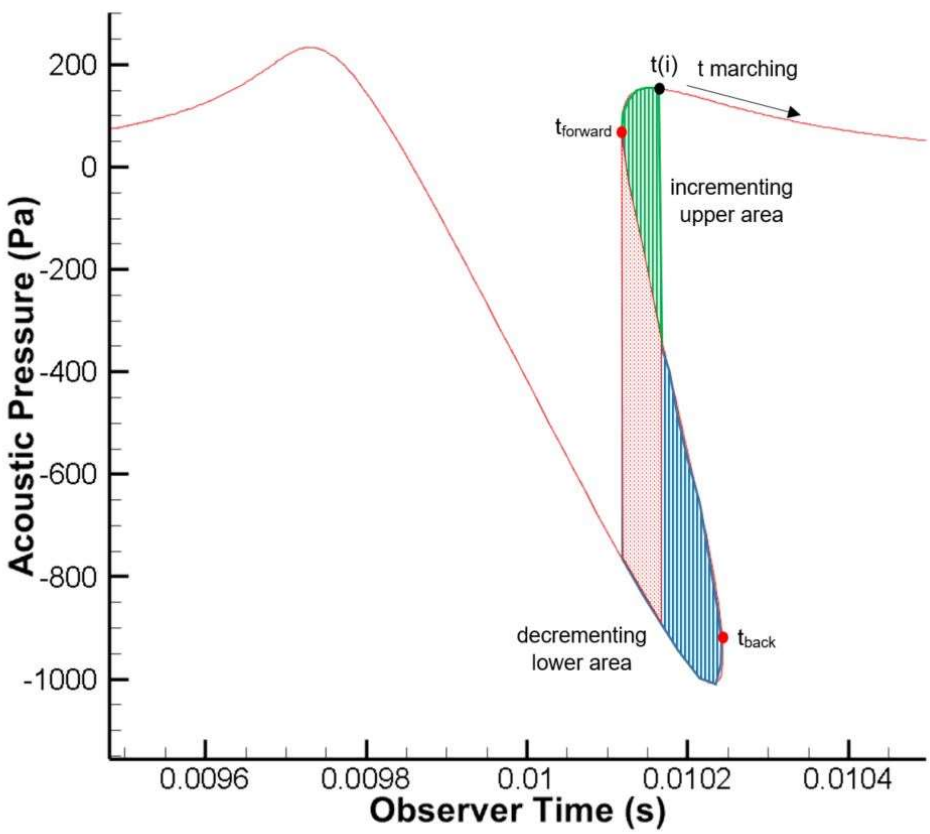

Figure 6.16: After reaching $t_{forward}$ the signal marches forward while computing 2 area calculations at once. The lower area is decremented while the upper area is incremented.

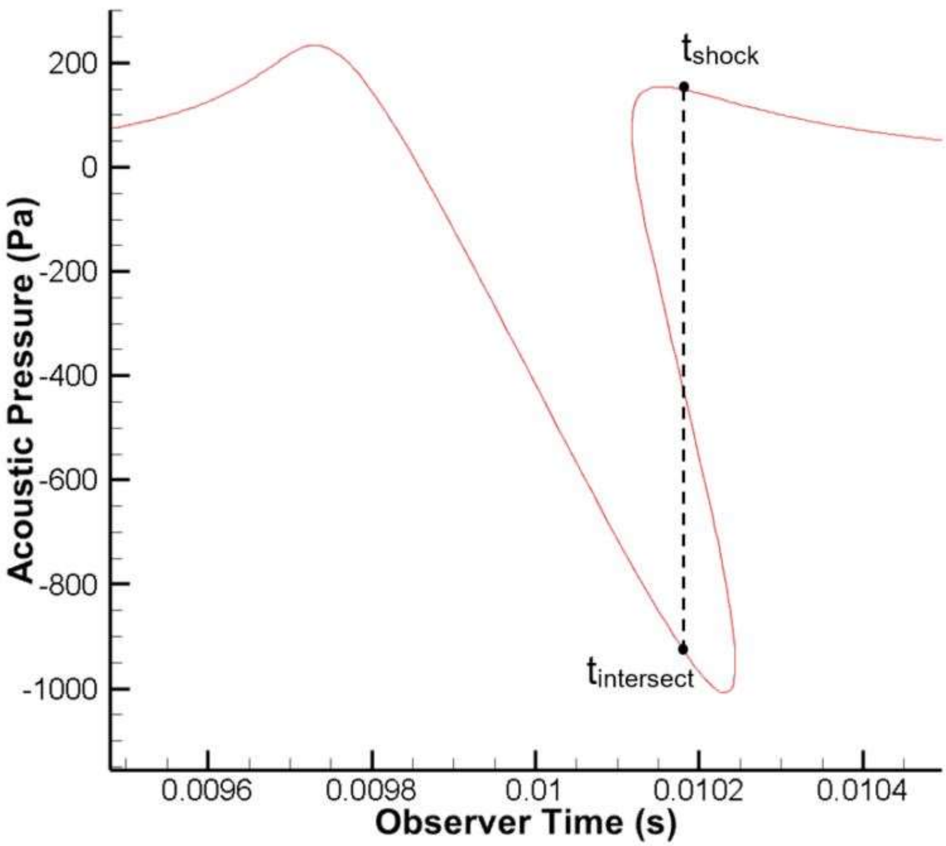

Figure 6.17: Insert a discontinuity into the signal where the top and bottom have equal areas.

HSI Model Results

The amplification and shearing functions were built by finding the best data points for each individual case. The resulting functions form a smooth model that will adjust a signal at any Mach number. This model was used to predict all eight cases that Baeder et al. studied. Figure 6.18 compares the acoustic pressure time histories of the HSI model to the original CFD data from Baeder et al. PSU-WOPWOP was also used to compute the spectrum data for both Baeder's CFD cases, as well as the HSI model. The resulting spectrum data is compared in Figure 6.19.

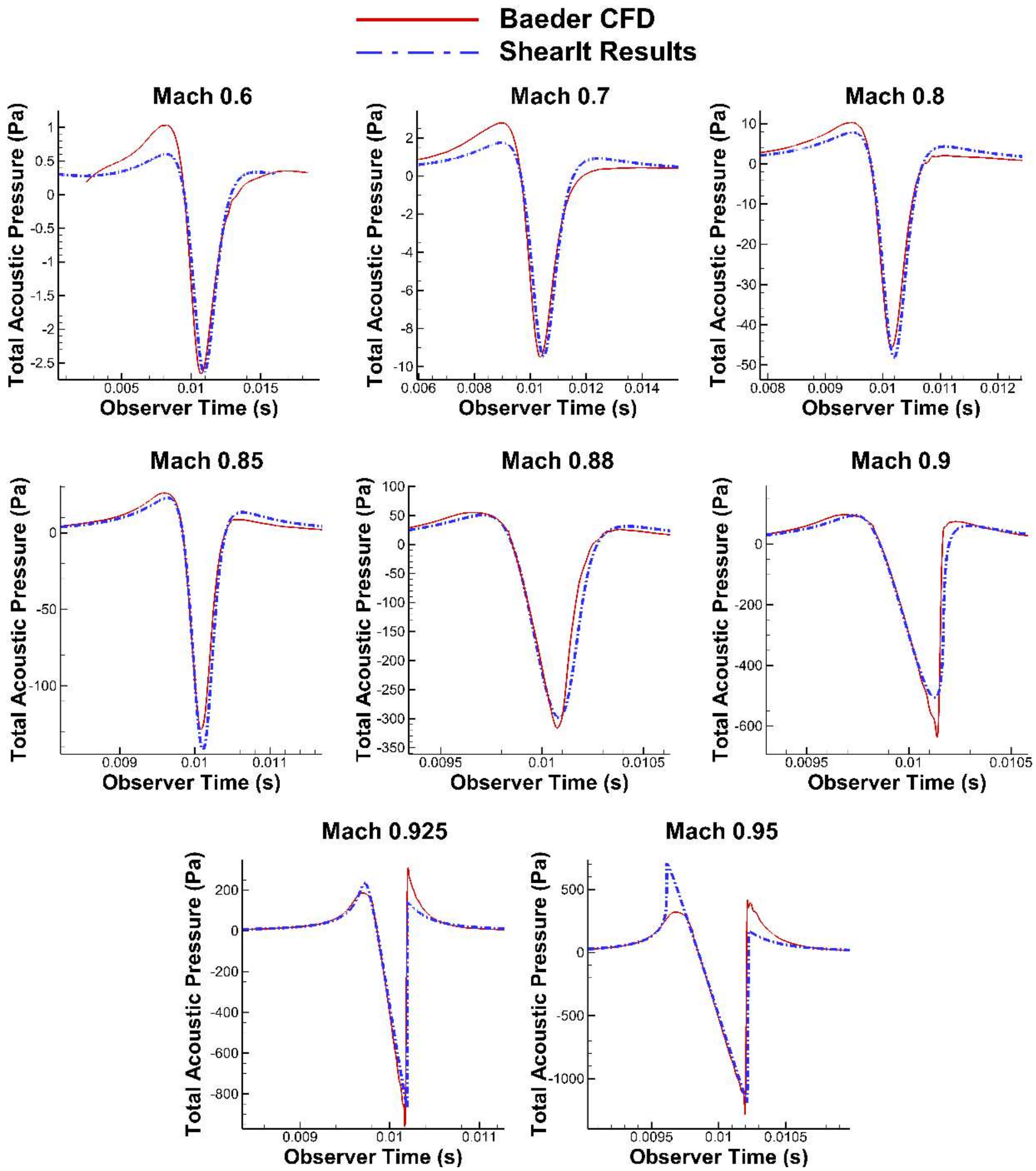

Figure 6.18: Comparison of acoustic pressure time history for post-processing model results and Baeder et al. CFD for tip Mach numbers ranging from 0.6 to 0.95.

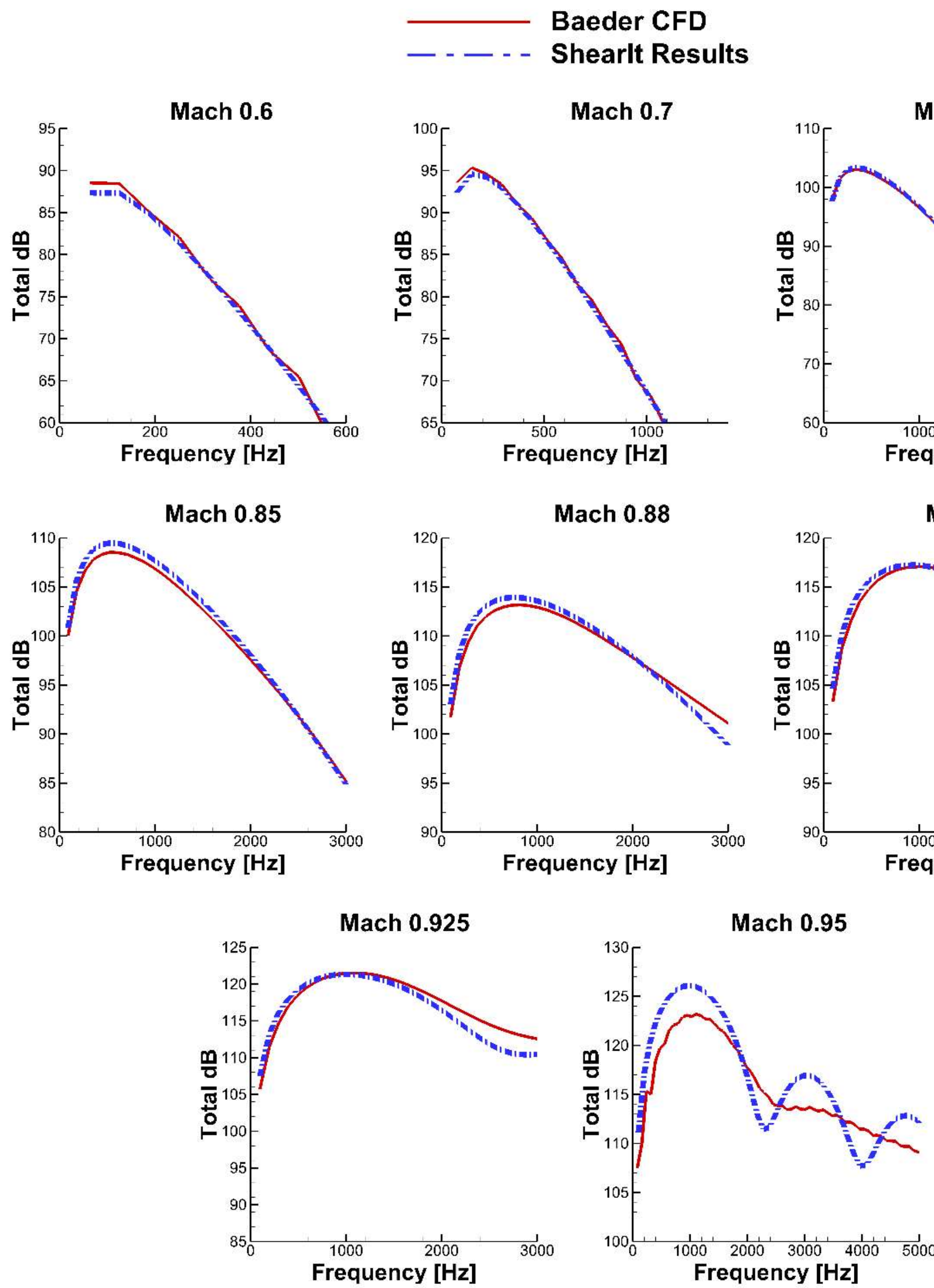

Figure 6.19: Comparison of acoustic spectrum for post-processing model results and Baeder et al. CFD for tip Mach numbers ranging from 0.6 to 0.95.

Overall, the model has a good fit for the UH-1H rotor. For tip Mach 0.6 and 0.7, the model accurately predicts the negative peak pressure of the signal. However, the peak to peak amplitude is not matched because the CFD model has a larger positive peak that PSU-WOPWOP does not capture. The shearing in these cases are negligible and the overall shape is matched. The shearing effects become increasingly noticeable at Mach 0.8 and higher. For both Mach 0.8 and 0.85 the HSI model slightly over predicts the negative peak amplitude. Both cases match the shear and overall shape of the signal very well. The largest discrepancy seen is the case of Mach 0.9. To match the amplitude of this case, the signal would need to be amplified by a much higher value. This value was outside of the overall trend formed from the rest of the cases. Nevertheless, the shearing angle of the signal did match the Baeder et al. CFD data very well. For cases Mach 0.925 and 0.95, the shock-fitting algorithm kicks in. The negative peak amplitude, shearing angle, and shock location match the CFD data very well. The HSI model over predicts the peak to peak amplitude because the positive peak is amplified. After the shock is inserted, there is a loss in amplitude that under predicts the positive peak.

PSU-WOPWOP was used to compute the acoustic spectrum data for the CFD data and the HSI data by reading in the acoustic pressure time histories. These plots focused on the frequency range that had the highest dB levels for each case. It is worth nothing that the CFD data did not have perfectly periodic signals due to issues around the boundaries. This can lead to jagged results in the spectrum data. This issue was most noticeable in the case of Mach 0.95, which is also the case that results in the greatest difference between the CFD and modeled predictions. Overall, the acoustic spectrum output calculated by the HSI model matches very well with the spectrum calculated with the CFD data. For the lower Mach numbers, a small range of frequencies result in high dB levels. As Mach number increases, the peak dB levels increase along with the frequency ranges that produce them. Mach 0.8 matches the acoustic spectrum nearly perfectly. Both Mach 0.85 and 0.88 over predict the peak dB value by about 1 dB. Interestingly, even though Mach 0.9 had the worst match in acoustic pressure time history, it still matches the peak dB level well. The entire acoustic spectrum in the range shown is within 2 dB of the CFD data. The Mach 0.95 case over predicts the peak dB level by about 3 dB, but both spectrums follow the same trend. Overall, the post-processing model agrees with the CFD data for both acoustic pressure and acoustic spectrum. The important trends are followed, and the overall shapes and peak values match.

The HSI model was implemented into the NPS so that the signal for each rotor is amplified, sheared, and shock fit individually. This allows each rotor to be adjusted based on its maximum M_r value, rather than shearing the entire aircraft's signal by one rotor's M_r value. This ensures that the model accurately predicts the HSI signal for each individual rotor, regardless of the configuration or presence of other rotors. This could be important, depending on the configuration and flight condition. For example, if a conventional helicopter has a tail rotor that operates at a much greater tip Mach number than the main rotor, it would be incorrect to adjust the main rotor signal based on the high tip Mach number from the tail rotor. This also allows ShearIt to correctly account for the maximum M_r value for each rotor. The orientation and position of a rotor may change the maximum M_r value depending on how each rotor plane is oriented with respect to the observer. Once ShearIt has adjusted the signal for each individual rotor, they are combined into one signal. The combined signal is the final output that represents the noise signal for the entire aircraft.

The goal of including a simple HSI model in the NPS was to provide a designer or optimizer that HSI effects are occurring because they dominate the noise output. The model that was implemented achieves this goal. The simple post-processing addresses the increase in amplitude of the acoustic pressure by amplifying the signal, and the impulsive nature is addressed by shearing and shock fitting the signal. In the future, more testing of the HSI model should be completed with different rotors. Different rotor geometry will naturally change the acoustic pressure time history computed in PSU-WOPWOP before the HSI model is used. Comparing this with data could adjust the empirical models for more accurate results. However since the focus of the NPS is conceptual design, and HSI conditions are often avoided, the level of detail used in this HSI model implementation may be satisfactory.

Chapter Summary

This chapter described the effects of HSI noise, and the development of the post-processing model that is used to predict them. The acoustic pressure time history created by PSU-WOPWOP is amplified, sheared, and shock fit as necessary. Empirical models are used to upscale the entire time history and shear the signal at an angle. Empirical equations for amplification factor and shear factor were derived using M_r and r_{obs}. These equations were developed by comparing WOPWOP output that ignores HSI effects to CFD data of a rotor at high tip speeds. If the resulting signal is multi-valued, a shock is fit into the signal. Results for many tip-Mach numbers were shown and compared to the CFD data.

The previous chapters discussed the noise sources (loading, thickness, broadband, BVI, HSI) and the models that were implemented to predict them. The next chapter demonstrates the entire system as a whole. Multiple NDARC aircraft simulate a mission that highlights each model, and the acoustic results are discussed for each.

Chapter 7

System Demonstration

This chapter demonstrates the capabilities of the noise prediction system as a whole. The previous chapters focused on showing the development of individual noise models that are appropriate for conceptual design and testing them for simple cases. This chapter predicts the noise output for multiple NDARC aircraft executing a mission. The overall sound pressure level is analyzed for every aircraft at each stage of the mission. Other plots including acoustic pressure time history, frequency analysis, disk plots to show loading and induced velocity, and wake plots are used to demonstrate the full noise prediction system for various operating conditions.

Mission Profile and Aircraft Data

The mission used in this chapter is designed to show the full capabilities of the system. Each model described in the earlier chapters (loading, thickness, BVI, HSI) are used to predict the acoustic output for four different aircraft configurations. Figure 7.1 shows the mission profile that is executed by NDARC to analyze four significantly different vehicles to demonstrate the capability of the NPS to predict noise for a variety of rotor configurations. In segment 1 the vehicle is commanded to climb at its best rate of climb while minimizing the power margin. Segment 2 is a level flight cruise condition flown at the aircraft's best endurance velocity. Segment 3 is a prescribed 6° descent to study the aircraft in a likely BVI condition. Segment 4 is a shallow descent case to show the aircraft in a non-BVI descent condition to compare the results with the previous segment. Segment 5 operates in level flight at the aircraft's maximum velocity. With a high enough forward speed, HSI effects can become important. Finally, segment 6 is a high-speed descent case to study any BVI effects that may get scaled by the HSI model. This mission profile was chosen to highlight each of the noise models implemented in this thesis, while also demonstrating the ability for NPS to predict the aircraft noise for widely varying NDARC configurations.

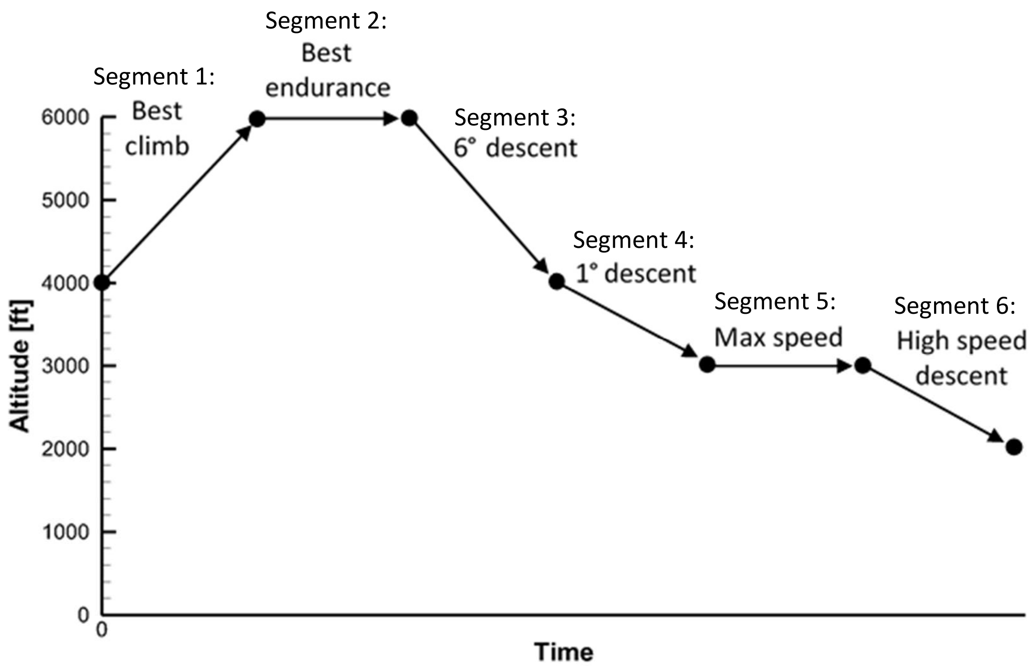

Figure 7.1: Mission profile that is executed for 4 NDARC vehicles to demonstrate the capability of the NPS.

The four aircraft used in this chapter are: 1) a conventional main rotor tail rotor helicopter; 2) a tandem helicopter; 3) a coaxial helicopter; and 4) a hexacopter. All of these vehicles were configured in NDARC by Johnson [45]. The first aircraft is a conventional helicopter. Its specifications are listed in Table 7.1, and a rendering of its configuration is shown in Figure 7.2. This model was designed to resemble the UH-60A. The next aircraft is a tandem configuration, which is shown in Figure 7.3 with its specifications listed in Table 7.2. This model was designed to resemble the CH-47D. A coaxial configuration is shown in Figure 7.4 and its specifications are listed in Table 7.3. This model was designed to resemble the XH-59A. The final aircraft is a hexacopter, which has six rotors that rotate in the opposite direction of the adjacent rotors. The locations and rotation direction for these rotors are shown in Figure 7.5 and the specifications are listed in table 7.4. All of these aircraft are designed with a tip speed of 700 ft/s. Each aircraft will execute the same mission with an identical payload weight of 3000 pounds. Each aircraft is designed for a different mission, so their weights are significantly different. Although a 3000 pound payload is used for each aircraft, the max payload is different for each aircraft.

Table 7.1: NDARC Helicopter Specifications

Aircraft	
Number of rotors	2
Aircraft weight	11,332 lbs
Main Rotor	
Number of blades	4
Blade radius	7.62 m
Chord	0.58 m
Thickness:chord ratio (t/c)	.09
Rotor rotation speed (Ω)	28 rad/s
Tail Rotor	
Number of blades	4
Blade radius	1.55 m
Chord	0.23 m
Thickness:chord ratio (t/c)	.09
Rotor rotation speed (Ω)	116 rad/s

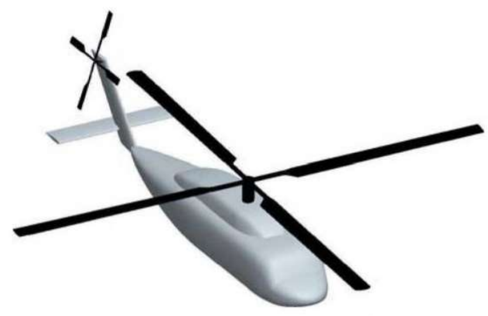

Figure 7.2: NDARC helicopter configuration [45].

Table 7.2: NDARC Tandem Specifications

Aircraft	
Number of rotors	2
Aircraft weight	23,754.2 lbs
Rotors	
Number of blades	3
Blade radius	9.144 m
Chord	0.81 m
Thickness:chord ratio (t/c)	.1
Rotor rotation speed (Ω)	23.33

Figure 7.3: NDARC tandem configuration [45].

Table 7.3: NDARC Coaxial Specifications

Aircraft	
Number of rotors	2
Aircraft weight	8,307 lbs
Main Rotor	
Number of blades	3
Blade radius	6.1 m
Chord	0.38 m
Thickness:chord ratio (t/c)	.09
Rotor rotation speed (Ω)	32.5 rad/s


Figure 7.4: NDARC coaxial configuration [45].

Table 7.4: NDARC Hexacopter Specifications

Aircraft	
Number of rotors	6
Aircraft weight	10,012 lbs
Rotors	
Number of blades	4
Blade radius	3.05 m
Chord	0.22 m
Thickness:chord ratio (t/c)	.09
Rotor rotation speed (Ω)	70 rad/s

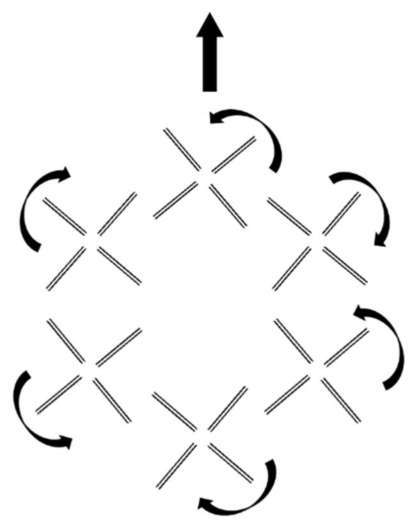
Figure 7.5: Overhead view of NDARC hexacopter configuration.

Table 7.5: Table of mission flight conditions for all four NDARC aircraft

	Forward Velocity (m/s)	Advance ratio (μ)	Climb Velocity [m/s, (ft/min)]	Climb Angle (deg)
Helicopter				
Segment 1	48.5	0.225	3.96 (779.5)	4.9
Segment 2	40.5	0.187	0.0 (0.0)	0.0
Segment 3	25.7	0.119	-2.69 (-196.9)	-5.99
Segment 4	25.7	0.119	-0.51 (-100.4)	-1.1
Segment 5	82.8	0.388	0.0 (0.0)	0.0
Segment 6	77.2	0.362	-6.6 (-1300.0)	-4.9
Tandem				
Segment 1	46.7	0.216	4.29 (844.4)	-5.28
Segment 2	46.4	0.215	0.0 (0.0)	0.0
Segment 3	25.7	0.121	-2.7 (-531.5)	-5.99
Segment 4	25.7	0.121	-0.51 (-100.4)	-1.1
Segment 5	89.0	0.412	0.0 (0.0)	0.0
Segment 6	77.2	0.363	-6.6 (-1300.0)	-4.9
Coaxial				
Segment 1	40.6	0.204	5.02 (988.2)	7.05
Segment 2	41.5	0.209	0.0 (0.0)	0.0
Segment 3	25.7	0.130	-2.69 (-196.9)	-5.99
Segment 4	25.7	0.130	-0.51 (-100.4)	-1.1
Segment 5	84.8	0.425	0.0 (0.0)	0.0
Segment 6	77.2	0.390	-6.6 (-1300.0)	-4.9
Hexacopter				
Segment 1	34.8	0.161	2.97 (584.6)	4.87
Segment 2	44.0	0.205	0.0 (0.0)	0.0
Segment 3	25.7	0.121	-2.69 (-196.9)	-5.99
Segment 4	25.7	0.121	-0.51 (-100.4)	-1.1
Segment 5	79.6	0.355	0.0 (0.0)	0.0
Segment 6	77.2	0.344	-6.6 (-1300.0)	-4.9

Mission Acoustic Results

Conventional Helicopter

The acoustic output for the conventional helicopter during the mission profile is studied in this section. OASPL is plotted for a hemisphere of observers with radius 10 rotor radii (76.2 m) away from the main rotor hub. The OASPL for segments 1-4 are shown in Figure 7.6. These plots map the entire observer hemisphere below the rotor. The elevation angle is displayed on the vertical axis, which makes the plane of the rotor at the top of this plot, and the point directly below the rotor is mapped to the entire bottom edge of the plot. The azimuth angle is shown on the horizontal axis with the direction directly in front of the aircraft at the center. The advancing side (0° to 180°) is on the right half of the plot and the retreating side (180° to 360°) is on the left half of the plot. This convention is used to map all of the observer hemispheres in this chapter.

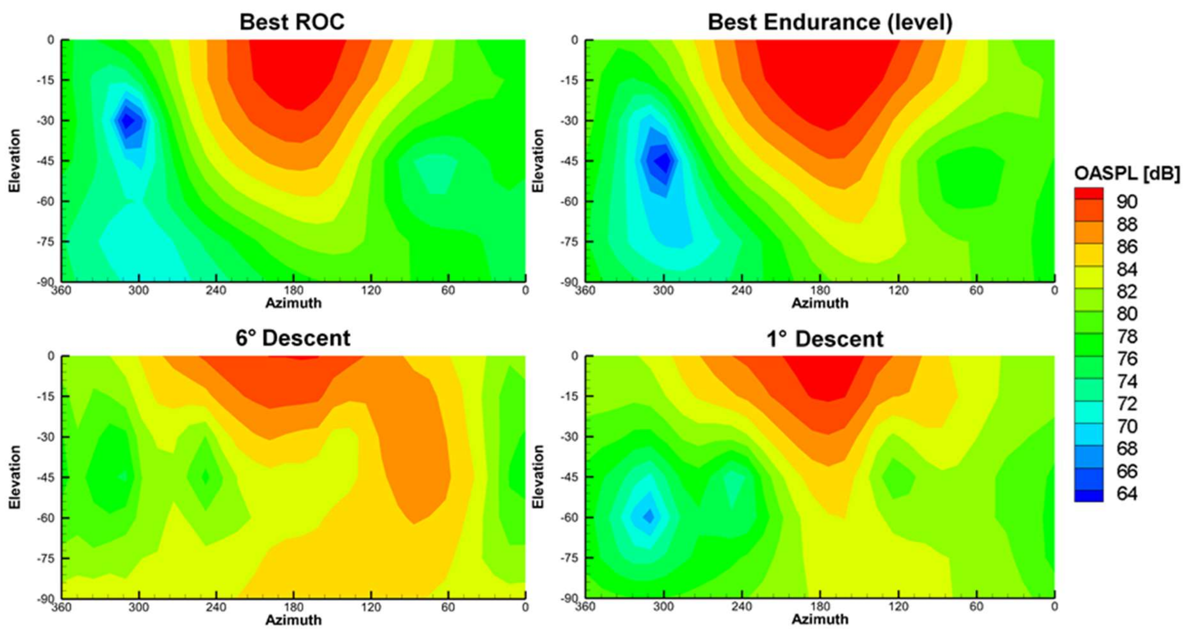

Figure 7.6: OASPL values mapped from a hemisphere of observers for the helicopter in segments 1-4.

Segment 1 trimmed the helicopter's flight speed and rate of climb to provide the best rate of climb for the power margin. For this aircraft, it resulted in a forward speed of 48.5 m/s ($\mu = 0.225$) and a climb speed of 3.96 m/s (779.5 ft/min). The noise is greatest in the plane of the rotor directly in front of the aircraft. This thickness noise contributes to this region. There is also a large region of high OASPL signals propagating between 15° and 45° below the plane of the rotor in front of the aircraft, shifted towards the advancing side of the main rotor. This band of higher noise levels is caused by the tail rotor. The OASPL signal that results only from the tail rotor is plotted for segments 1 and 2 in Figure 7.7. The maximum OASPL value emitted by the tail rotor is smaller than the main rotor, and it has a different directivity. The lowest noise levels are on the port side of the helicopter (retreating side of the main rotor). The tail rotor on this aircraft is canted by a 20° angle, which may be the result of this directivity pattern.

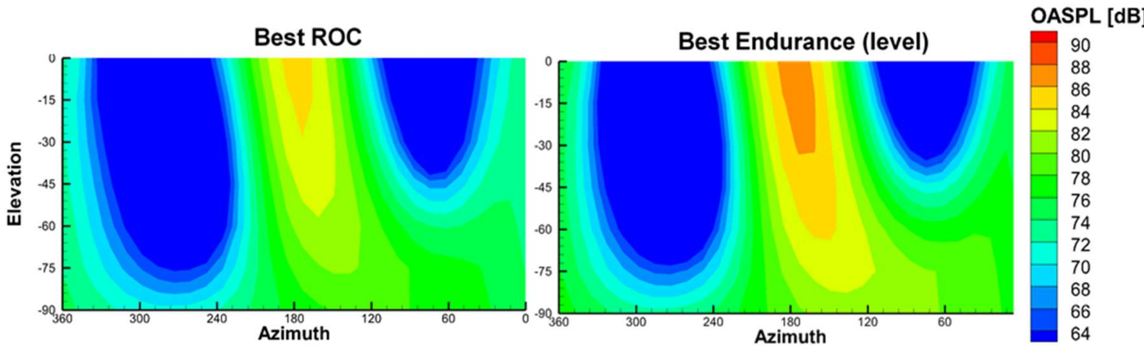

Figure 7.7: OASPL values from the helicopter tail rotor mapped for a hemisphere of observers (left Segment 1, right segment 2).

In segment 2 NDARC found the best endurance velocity to be 40.54 m/s ($\mu = 0.187$) for a level flight condition at this altitude. The results are similar to segment 1, however the region of the loudest noise signal is larger, extending further below the plane of the rotor. The noise signal below the rotor is larger everywhere directly below the helicopter, but it is lower on the port side of the helicopter between 30° and 75° below the rotor plane. The same band of noise created by the tail rotor is present in this segment as well.

Segments 3-4: Descent

In segment 3 a 6° descent is prescribed to induce a BVI condition. The forward speed in segment 3 was 25.7 m/s ($\mu = 0.119$) and the helicopter descent speed was 2.7 m/s (531.5 ft/min). There is a very large region of a high noise signal on the advancing side of the aircraft. Between 60° and 130° azimuth as far as 60° below the rotor there is an increase in the noise signal caused by the BVI condition. This increase in noise levels continues all the way down to 90° below the aircraft for a large portion of the advancing side of the main rotor (starboard side). This increase is caused by the unsteady loading due to the trailing wake. The tip-vortex trajectories are shown in Figure 7.8 where the aircraft is flying to the left while the blades rotate counterclockwise. The aircraft's main rotor has a 3° forward tilt, which is evident in the side view. In this segment, the blade is operating in its own wake. This can be seen in the side view of the tip-vortex geometry, as the trailing vortices travel above and below the rotor plane. Due to a lower advance ratio, there are more opportunities for the main rotor to interact with the wake. Many of the tip-vortices pass very close to the rotor. A parallel interaction is captured on the upper right blade in this figure. The resulting unsteady loading effects that occur for this segment are plotted around this rotor disk in Figure 7.9. These disks are oriented so the aircraft is flying towards the top of the page and the advancing blade is on the right half of the figure. The left plot shows distinct bands rapidly changing induced velocity across the rotor disk. These rapid changes in induced velocity directly impact the blade loads as seen in the right plot. The induced velocity seen on the rotor disk has a "scalloped" pattern. This leads to unsteady loading that has bands of choppy loading, rather than smooth bands of high loading. This is a numerical anomaly, and is not physical in nature. Further study is needed to determine the source of this numerical anomaly.

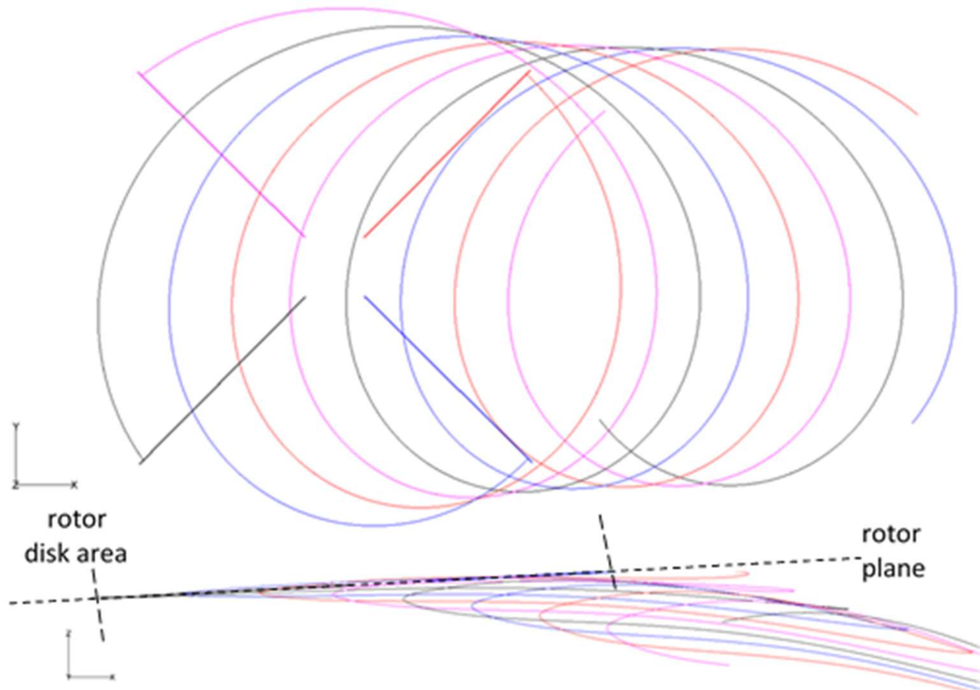

Figure 7.8: Top and side view of the wake generated for the helicopter in segment 3.

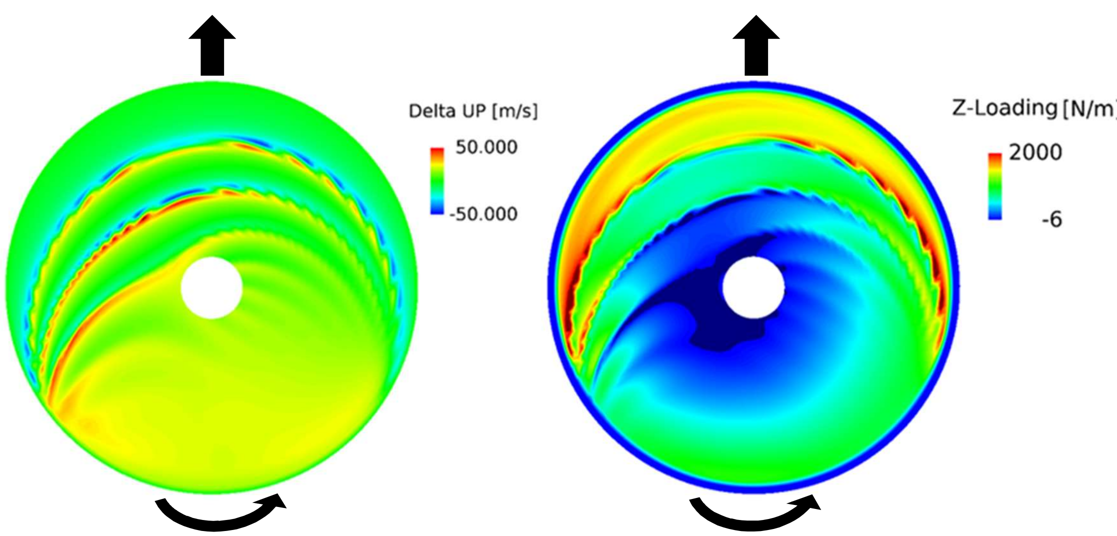

Figure 7.9: Disk plots for the helicopter configuration main rotor in segment 3 (left induced velocity profile, right loading perpendicular to the rotor disk).

Blade-vortex-interaction noise occurs at a specific range of frequencies. To highlight this range, the blade-vortex-interaction sound pressure level (BVISPL) is used. In this project, BVISPL is defined as all noise between the 7th and 40th harmonics of the main rotor's blade passage frequency [46]. For this helicopter, the resulting frequency range is approximately 125-715 Hz. The BVISPL for the helicopter main rotor in segment 3 is plotted in Figure 7.10 using identical mapping of the hemisphere that was used in the previous OASPL plots. Plotting the BVISPL helps isolate the directivity of the BVI noise.

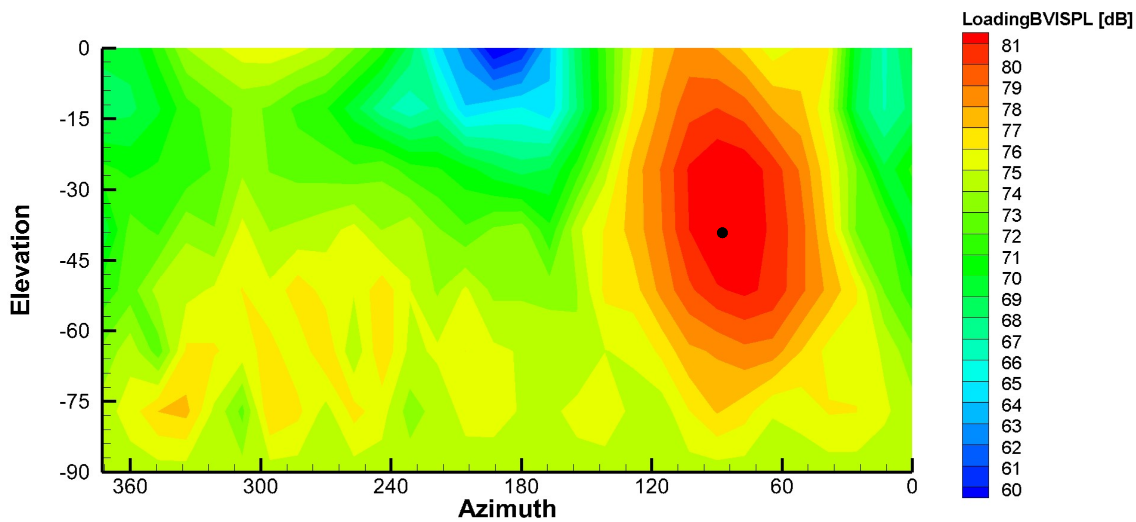

Figure 7.10: BVISPL for a hemisphere of observers located 10 rotor radii (76.2 m) away from the main rotor hub for helicopter segment 3.

When looking at BVISPL, it is much clearer where the strong BVI effects are occurring. There are strong BVI effects on the advancing side of the rotor. The maximum occurs between 75° and 100° azimuth for observers 20° to 50° out of the plane of the rotor. However, there are significant BVI effects extending from just below the rotor plane down to 75° below the plane of the rotor. There are also isolated BVI events on the retreating side of the rotor as well. These are lower in magnitude, but do make a noticeable difference over the baseline SPL signals. The acoustic pressure time history and spectrum data are studied for the observer that experiences the maximum BVISPL signal. This observer is located at an elevation angle of -39° and an azimuth angle of 87° and is indicated by a dot in Figure 7.10. The acoustic pressure time history and spectral data for the observer in the BVI hotspot are plotted in Figure 7.11 and Figure 7.12, respectively.

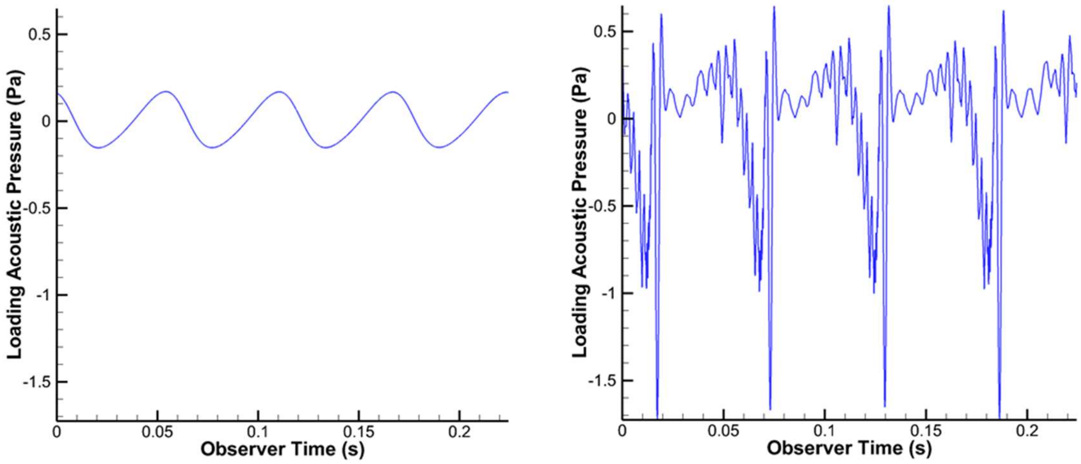

Figure 7.11: Acoustic pressure time history comparison for an observer in the BVI hotspot for segment 3 for the helicopter (left BVI effects ignored, right BVI effects included).

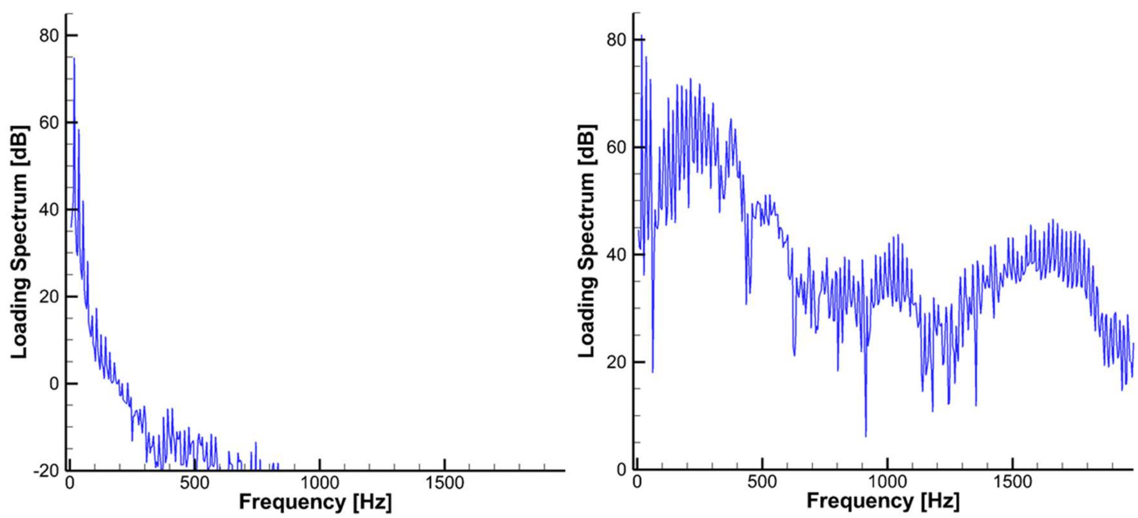

Figure 7.12: Spectrum comparison for an observer in the BVI hotspot for segment 3 for the helicopter (left BVI effects ignored, right BVI effects included).

The acoustic pressure time history and spectral data were also computed for the observer in the BVI hotspot with the BVI model turned off. This allows a direct comparison to see how the BVI model affects the loading noise time history and spectrum (see Figure 7.11 and Figure 7.12).

The acoustic pressure and spectrum data are significantly different when the BVI effects are included. The acoustic pressure time history without BVI effects shows 4 smooth peaks, one for each blade. When the unsteady effects are included, the acoustic pressure amplitude increases by an order of magnitude. The acoustic pressure signal shows clear BVI spikes. The rapid jump from positive amplitude to peak negative amplitude is indicative of a strong BVI event. When comparing the spectrum data, the dB levels across frequencies are significantly different as well. It is important to note that the scale on the vertical axis in Figure 7.12 is adjusted to show a comparison of the signal. When ignoring BVI effects, the dB levels for higher frequencies quickly become insignificant. When BVI effects are included, the peak dB level increases by about 6 dB, and many higher frequencies are significant. The BVISPL frequency range for this rotor was calculated to be 125-715 Hz. This band of frequencies produce significantly large dB levels. When the BVI model is turned off, this band of frequencies is practically nonexistent. The numerical anomaly that is present in the blade loading leads to the high frequency "hash" in the acoustic pressure time history and spectrum plots. This numerical "hash" leads to the presence of more high-frequency content in the signal than BVI alone. These high frequencies are in the BVISPL range, which means that the BVISPL plots may be exaggerated

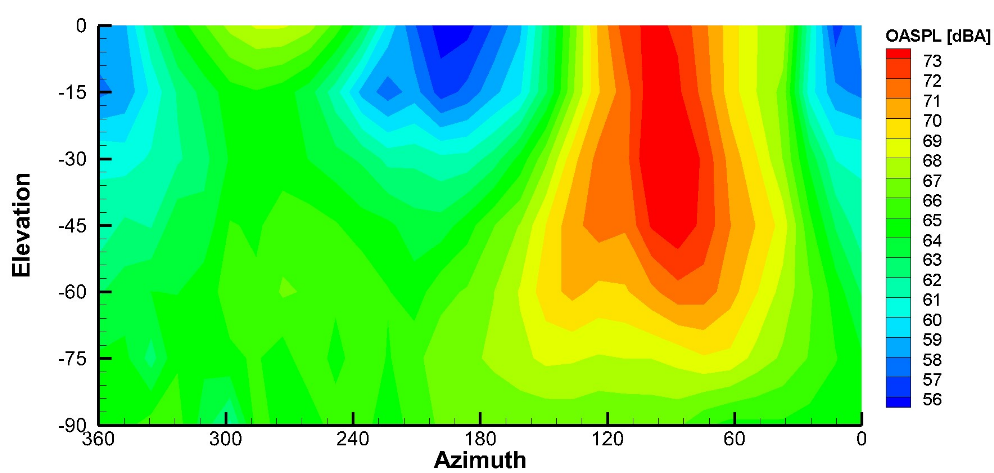

Figure 7.13: A-Weighted OASPL for a hemisphere of observers located 10 rotor radii (76.2 m) away from the main rotor hub for helicopter segment 3.

To study the effects that these higher frequencies have on a human observer, the A-weighted OASPL was plotted for the observer sphere in Figure 7.13. The A-weighting emphasizes the frequencies that the human ear is most sensitive to. The A-weighted OASPL plot is similar to the BVISPL plot. This demonstrates that BVI noise is in the range of human sensitivity. Observers on the advancing side from 0° to 45° below the plane of the rotor experience the maximum A-weighted noise signal. Many of the observers on the advancing side of the rotor experience an increased OASPL when including the A-weighting. This exemplifies the importance of accounting for BVI events when predicting the noise of a rotorcraft. It is worth noting that the high frequency numerical "hash" in the acoustic pressure signal may erroneously contribute to the A-weighting values. This would lead to an exaggeration of the A-weighted noise levels when compared to a smooth signal.

In segment 4 the helicopter was flown in a 1° descent where BVI effects are less significant. The forward velocity was 25.7 m/s ($\mu = 0.119$) and the descent speed was 0.51 m/s (100.4 ft/min). Figure 7.14 shows the wake that trails behind the rotor. The wake never travels above the rotor, and descends more quickly. This means that the rotor never experiences significant BVI like it did in segment 3. The wake is close enough to the rotor that there is some unsteady effect introduced on the blades, however it is not significant like the BVI case. This induced velocity is plotted in Figure 7.15 with the same scale as the induced velocity in segment 3. There is only one band of induced velocity, which has a maximum of 11 m/s – a much lower magnitude than the previous case. Figure 7.16 shows the BVISPL on the observer hemisphere using identical BVISPL levels as segment 3. The maximum BVISPL experienced by the observers in segment 4 is more than 10 dB lower than the maximum in segment 3.

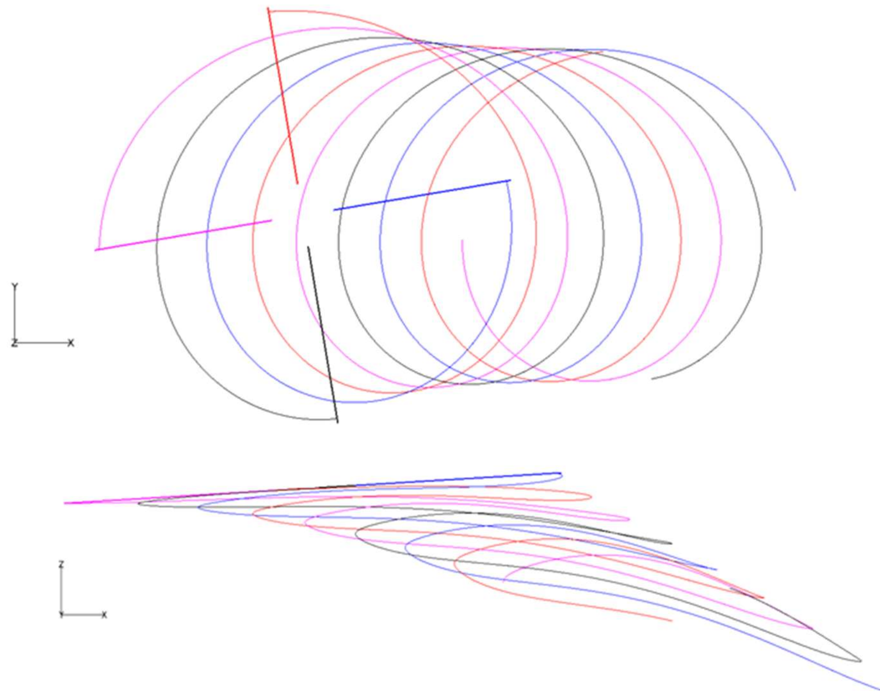

Figure 7.14: Top and side view of the wake generated for the helicopter in segment 4.

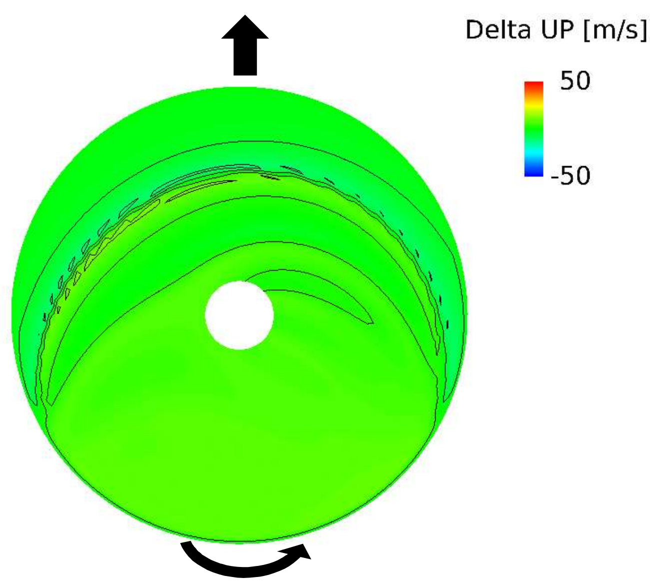

Figure 7.15: Induced velocity on the rotor disk for the helicopter in segment 4.

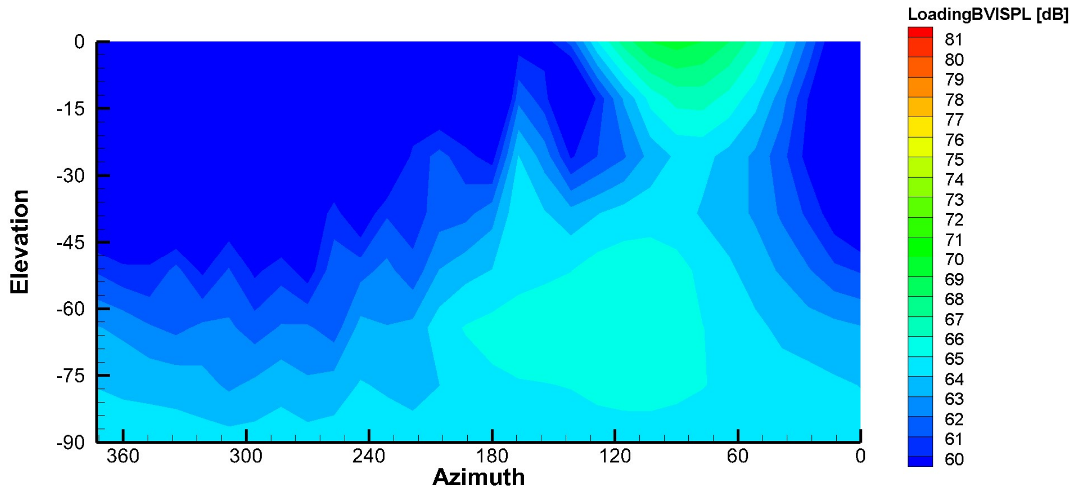

Figure 7.16: BVISPL for a hemisphere of observers located 10 rotor radii (76.2 m) away from the main rotor hub for helicopter segment 4.

Segment 5: Max Speed

Segment 5 operates the helicopter at its maximum speed. NDARC trimmed the aircraft to travel at a level flight speed of 82.8 m/s ($\mu = 0.388$). HSI effects become more significant here, so the acoustic pressure is amplified by the post-processing HSI model. The acoustic pressure time histories are plotted at five locations in front of the aircraft at varying elevation angles. These observer locations are positioned 10 rotor radii away from the main rotor hub at equally spaced elevation angles along the centerline of the aircraft. Figure 7.17 shows these observer positions. The acoustic pressure time history for each observer location is plotted in Figure 7.18. The current implementation of ShearIt does not allow the NPS to produce hemispherical plots because it adjusts the signal for each rotor one observer at a time. This is discussed further in chapter 8.

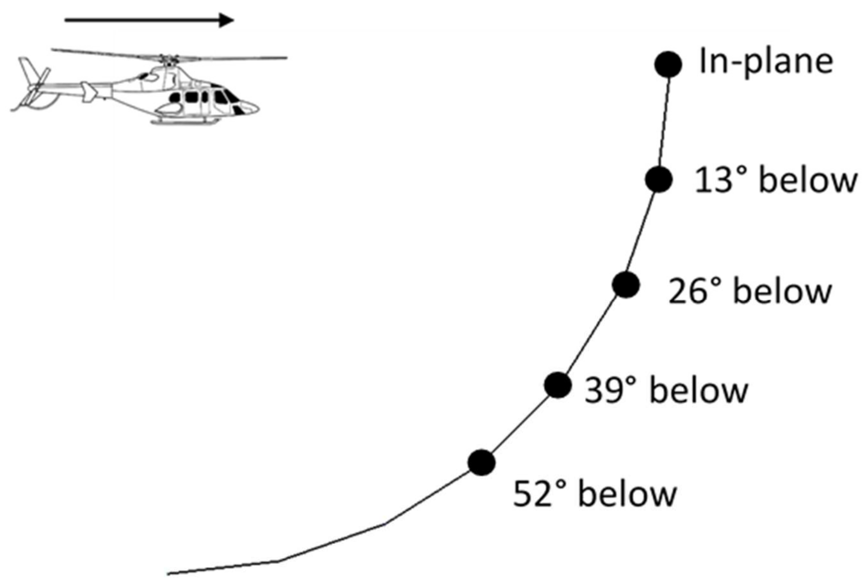

Figure 7.17: Observer locations for the HSI cases positioned 10 rotor radii away from the main rotor hub at equally spaced elevation angles (10R not to scale).

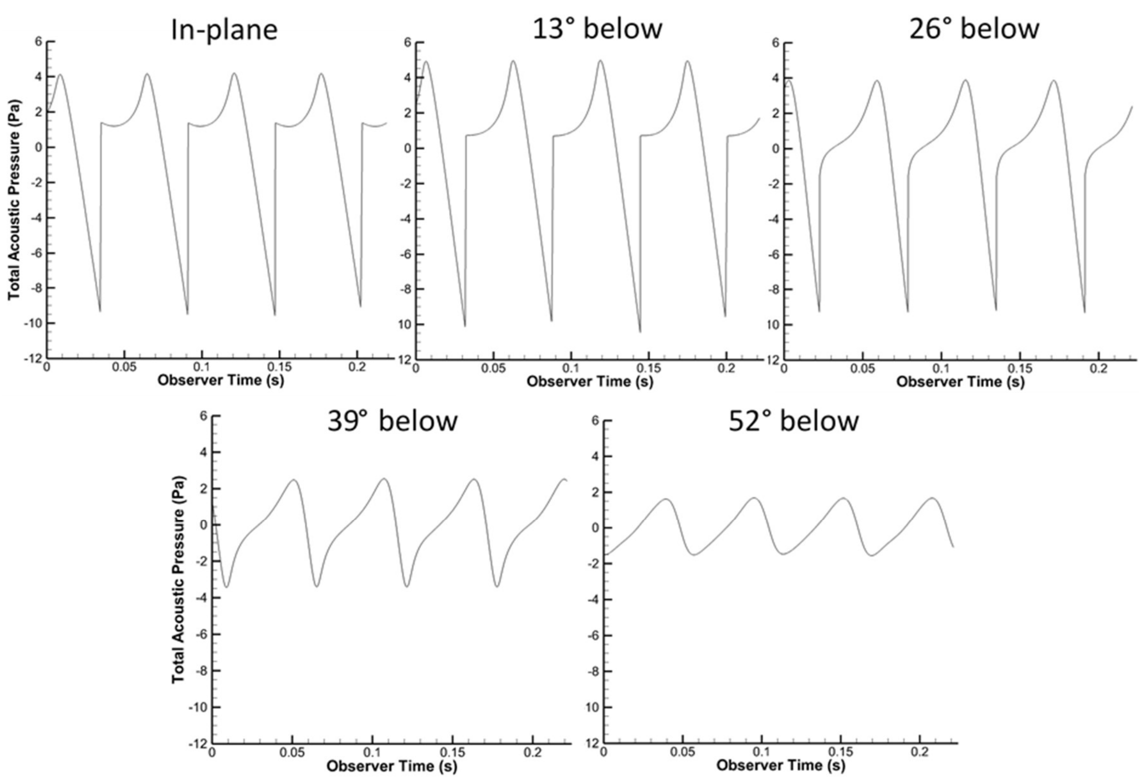

Figure 7.18: Acoustic pressure time history after HSI post-processing for an array of observers in front of the helicopter in segment 5.

The HSI model adjusts the acoustic pressure signal based on the maximum Mach number in the radiation direction (M_r) that an observer experiences as the blades complete one revolution. The observer in the plane of the rotor experiences the highest value of M_r, and therefore the acoustic pressure signal is sheared more than any other observer. For this observer, the M_r value is 0.88. When accounting for distance to the observer and the Mach number, clear shockwaves are formed. There are four pulses, one for each blade. Thickness noise is dominant in this region, so the pulses follow the general shape of a thickness noise signal. For the observers at 13° and 26° below the rotor plane the values of M_r are 0.87 and 0.83, respectively. When the acoustic pressure signal is sheared by a large enough angle, there is a loss in amplitude. For the observer 13° below the rotor plane, the signal is sheared slightly less than the in-plane observer. This slightly smaller shearing angle results in a slightly smaller reduction in amplitude when compared to the in-plane observer. In the data from Baeder et al. [30] (with which the HSI model was calibrated), the in-plane observer consistently had the highest amplitude. The empirical relations used for shearing depend on radiation distance and M_r. These relations may need to be tuned to limit the significant amplification loss at far distances and high Mach numbers. For the observer 26° below the rotor plane, the amplitude of the noise signal was smaller before the post processing, because out of plane the thickness noise, which dominates this case at high speeds, is less prevalent. This signal is sheared just enough to shock. The observer 39° below the rotor plane has a value of M_r of 0.77, while the observer 52° below the rotor plane has a value of 0.68. The signals at these locations are amplified and sheared significantly less than the observers that are closer to the plane of the rotor. The acoustic pressure at these locations have lower amplitudes and do not need shock fitting. In the cases that are further from the rotor plane, loading noise becomes more significant. This changes the overall shape of the pulses in the signal, and that shape is retained after being amplified and sheared.

Segment 6: High-Speed Descent

Segment 6 was designed as a high-speed descent to combine the effects of BVI and HSI for the system. The helicopter operated in a 5° descent with a forward flight speed of 77.17 m/s ($\mu = 0.363$) and a descent speed of 6.6 m/s (1300 ft/min). The resulting wake for this case is shown in Figure 7.19. From the top view it is clear that tip-vortices are spread farther apart due to the higher advance ratio in segment 6 (as compared to segment 3). This significantly decreases the number of interactions that the blade can have with its wake. After one rotation the wake is already far enough behind the rotor disk that it will have no significant impact on the rotor loading. From the side view, it is clear that the rotor does operate in its own wake as expected from a 6° descent. There is a small window of interaction that is possible for the rotor in this case. One parallel interaction can be seen on the lower right blade (retreating side) in the top view. The resulting induced velocity profile and unsteady blade loads are plotted for the rotor disk in Figure 7.20. There are a few clear bands in the induced velocity plot. These impulses do have an impact on the rotor loading, but they are less significant than those shown in the other cases. To help visualize them more clearly, 32 contour lines 57 N/m apart were placed on the loading plot.

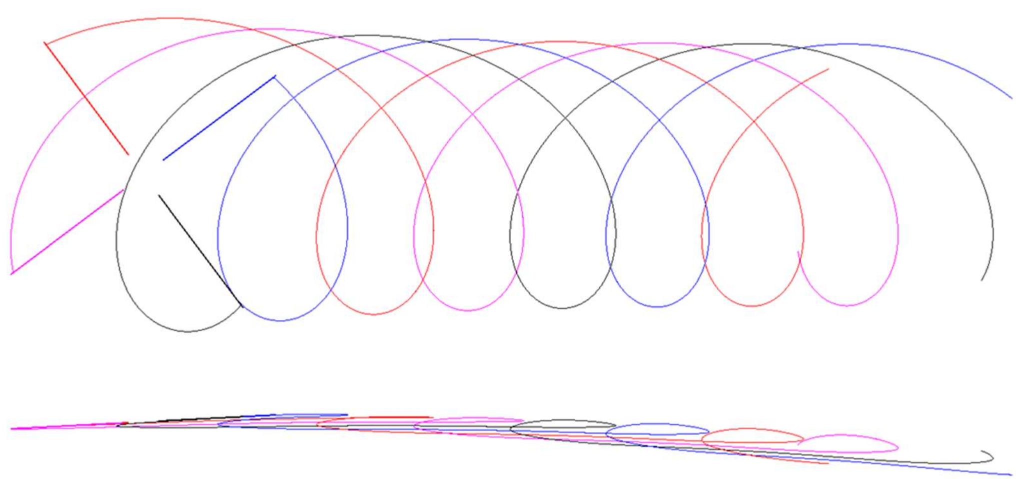

Figure 7.19: Top and side view of the wake generated for the helicopter in segment 6.

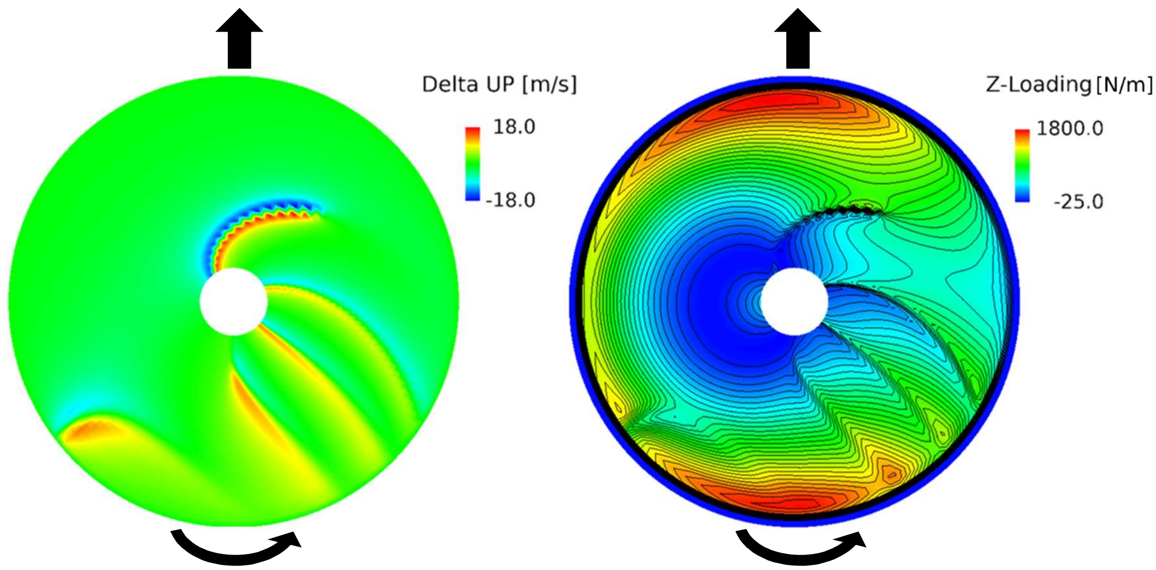

Figure 7.20: Disk plots for the helicopter main rotor in segment 6 (left induced velocity profile, right loading perpendicular to the blade with contour lines).

Five observers were placed at identical locations as shown for segment 5. The acoustic pressure time histories at each location are plotted in Figure 7.21. The BVI signals are not prevalent near the plane of the rotor, so the signals shown at these locations resemble the thickness noise pulses as they did for segment 5. There are small impulsive shapes on the signal that appear due to the unsteady loading. The maximum values of M_r calculated for the observers in plane, 13° below the rotor plane, and 26° below the rotor plane are $M_r = 0.855$, 0.85, and 0.83, respectively. The signals in all three cases needed shock fitting due to the high shear of the signal. Like the previous case, the in-plane observer experiences a slight loss in amplitude due to the higher shearing angle. The observers that are further from the rotor plane experience more BVI effects but are amplified and sheared less because HSI is less prevalent. The observers at 39° and 52° below the rotor plane have M_r values of 0.77 and 0.70, respectively. Neither of these signals are sheared enough to need shock fitting. The unsteady effects due to the tip-vortices are mild compared to the clear BVI case in segment 3. The observers used to study the HSI noise in segments 5 and 6 are placed directly in front of the rotor. These locations capture some BVI effects, but the directivity of BVI noise is not typically directly ahead of the aircraft.

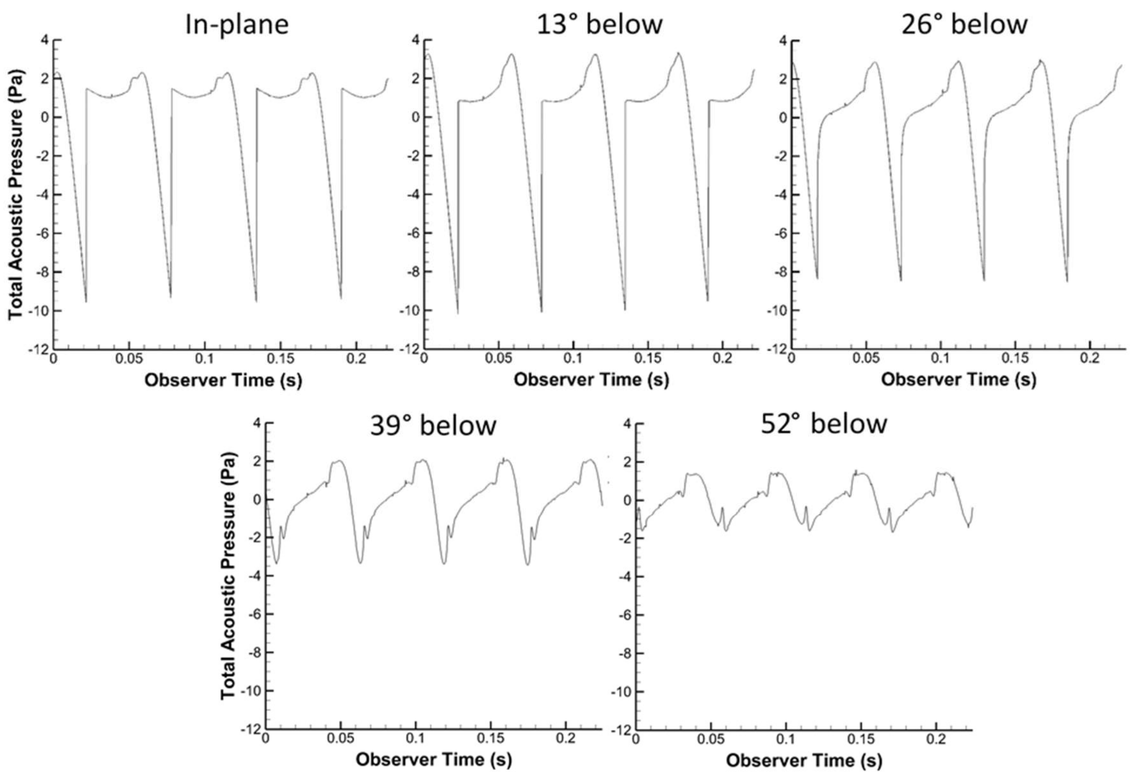

Figure 7.21: Acoustic pressure time history after HSI post-processing for an array of observers in front of the helicopter in segment 6.

Tandem Helicopter

This section studies the acoustic results for the tandem configuration for the same mission as the conventional helicopter. The OASPL values for segments 1-4 are plotted in Figure 7.22 for a hemisphere of observers 10 rotor radii (91.4 m) away using identical mapping that was used for the previous OASPL plots. Segment 1 trimmed the aircraft for best rate of climb. For the tandem configuration the resulting forward speed and climb speeds are 46.7 m/s ($\mu = 0.216$) and 4.3 m/s, respectively. For this segment, the loudest acoustic signal occurs in front of the aircraft from 0° elevation down to about 20° below the plane of the rotor. With counter rotating rotors, there is not one side of the aircraft that is advancing or retreating since each rotor's advancing sides are on opposite sides of the aircraft. The observers between 100° azimuth and 250° azimuth experience a significant OASPL signal as far as 40° below the rotor.

Segment 2 trimmed this aircraft's best endurance speed for a level flight condition. For the tandem configuration speed for best endurance is 46.4 m/s ($\mu = 0.215$). The OASPL signal for the level flight speed is louder than that of best rate of climb. The region of peak noise extends from 120° to 240° azimuth, between the plane of the rotor and 40° below the rotor plane.

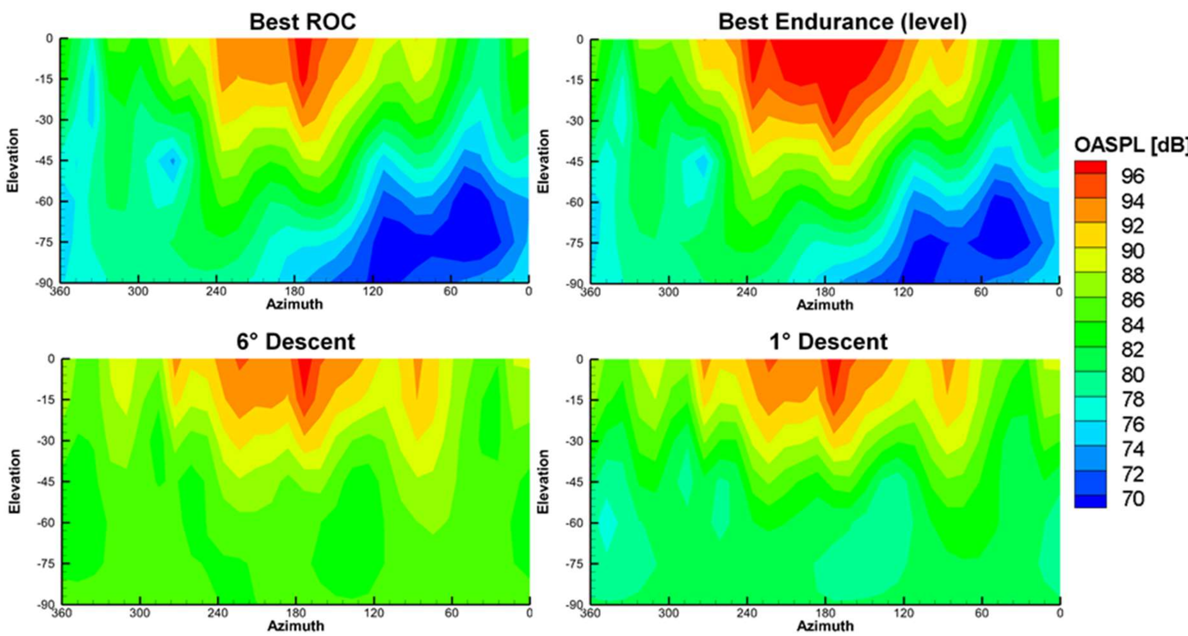

Figure 7.22: OASPL values mapped from a sphere of observers for the tandem configuration in segments 1-4.

Segments 3-4: Descent

Segment 3 prescribed the aircraft at a 6° descent. The forward speed in segment 3 was 25.7 m/s ($\mu = 0.121$) and the helicopter descent speed was 2.7 m/s (531.5 ft/min). The wake calculated for this case is shown for both rotors Figure 7.23. It is important to note that the BVI calculations for these cases are done individually for each rotor. The front rotor's wake is not deformed by the rear rotor, or the rear rotor's wake and vice-versa. The rear rotor is not influenced by the upstream wake. The wake for the rear rotor is closer to the rotor plane than the wake of the front rotor. To get a closer look at the tip-vortices that can interact with the blades, the wake trailing behind the rear rotor is shown in in Figure 7.24. For the rear rotor, the aircraft is flying to the left and the blades are rotating clockwise. There is a parallel BVI event captured on the lower right blade (advancing side) midway along the span. Because of the angle of the rotor shaft, the wake does not stay in the rotor plane as long as it did in the helicopter case. This results in a lower BVI influence at this prescribed mission segment. However, the wake does travel close enough to the rotor to influence the loading. The unsteady influence on the front rotor is shown in Figure 7.25 and the rear rotor is shown in Figure 7.26. The aircraft is flying towards the top of the page and the direction of rotation of the blades are labeled with arrows. On the front rotor there is one strong BVI interaction shown by the band of induced velocity across the disk. This is strongest on the retreating side, but does travel across the rotor disk. There are a few smaller interactions on the rotor disk that have a negligible induced velocity compared to the strong BVI event. In the disk loading plot, there is a clear jump due to the unsteady interaction induced by the wake. The rear rotor is affected more severely by BVI. The bands of induced velocity are in similar places, but at higher magnitudes. The "scalloped" pattern in induced velocity is present in this case as well. This can lead to extra "noise" in the BVISPL and acoustic pressure time history plots like the previous case.

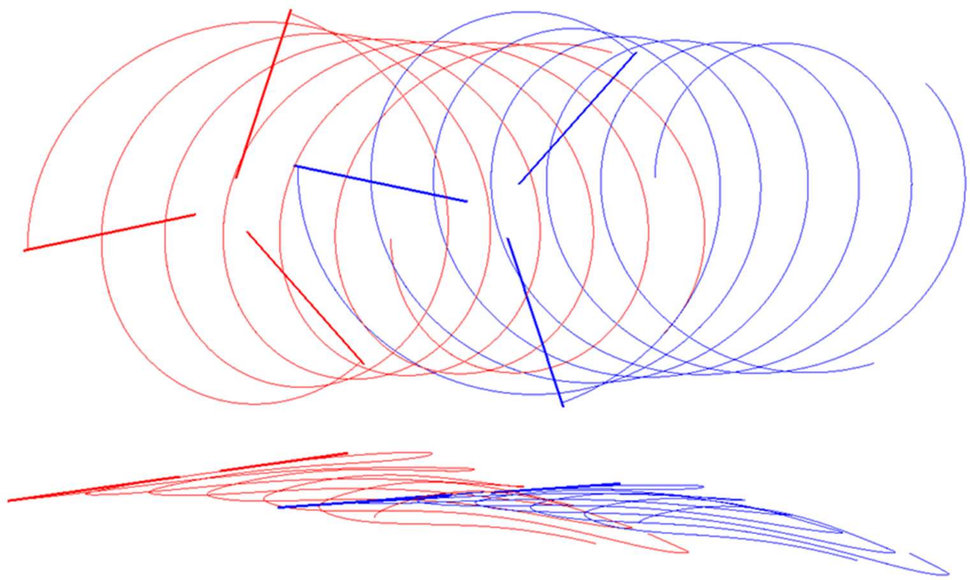

Figure 7.23: Top and side view of the wake generated for both rotors of the tandem configuration in segment 3.

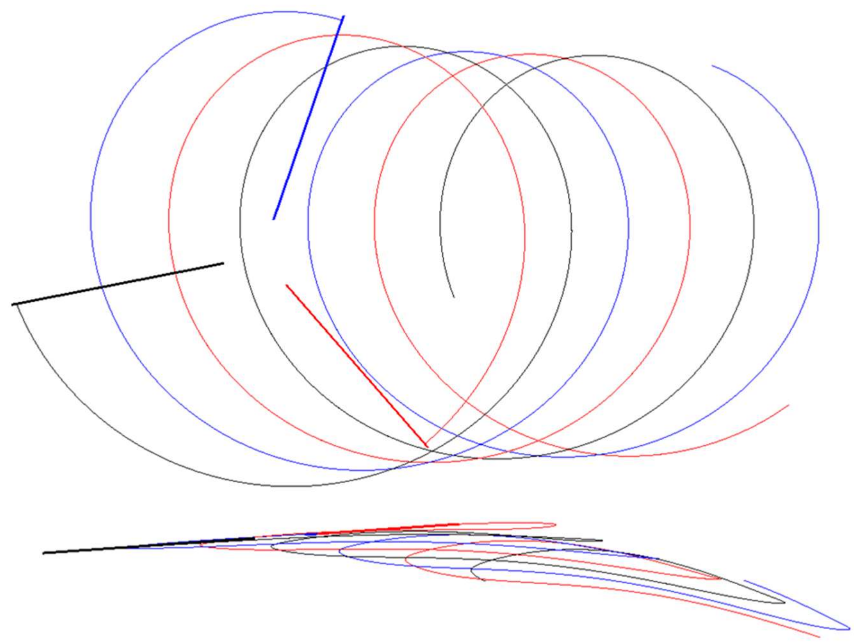

Figure 7.24: Top and side view of the wake generated for the tandem configuration's rear rotor in segment 3.

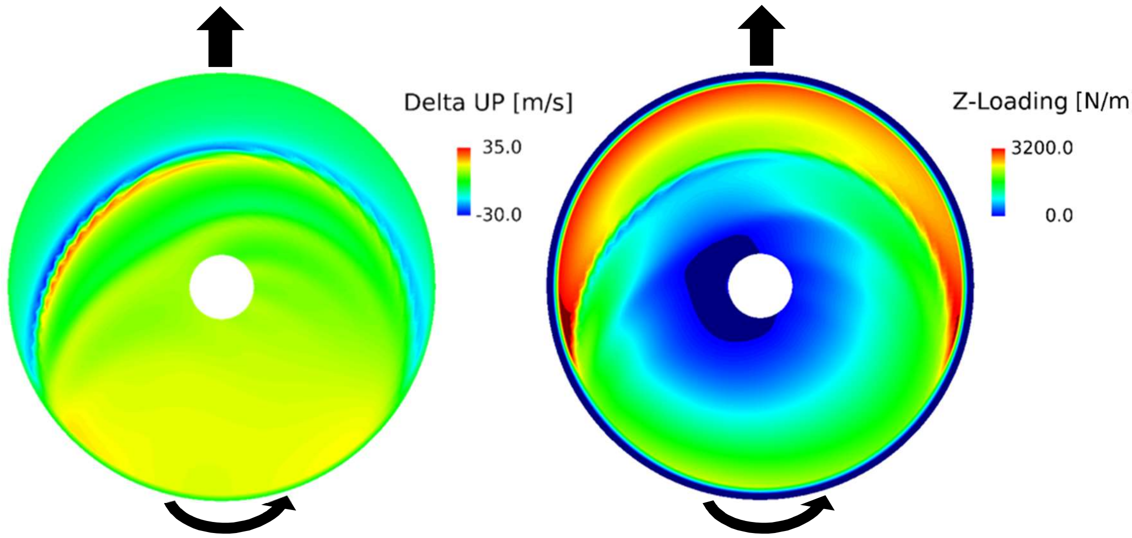

Figure 7.25: Disk plots for the tandem configuration front rotor in segment 3 (left induced velocity profile, right loading perpendicular to the blade).

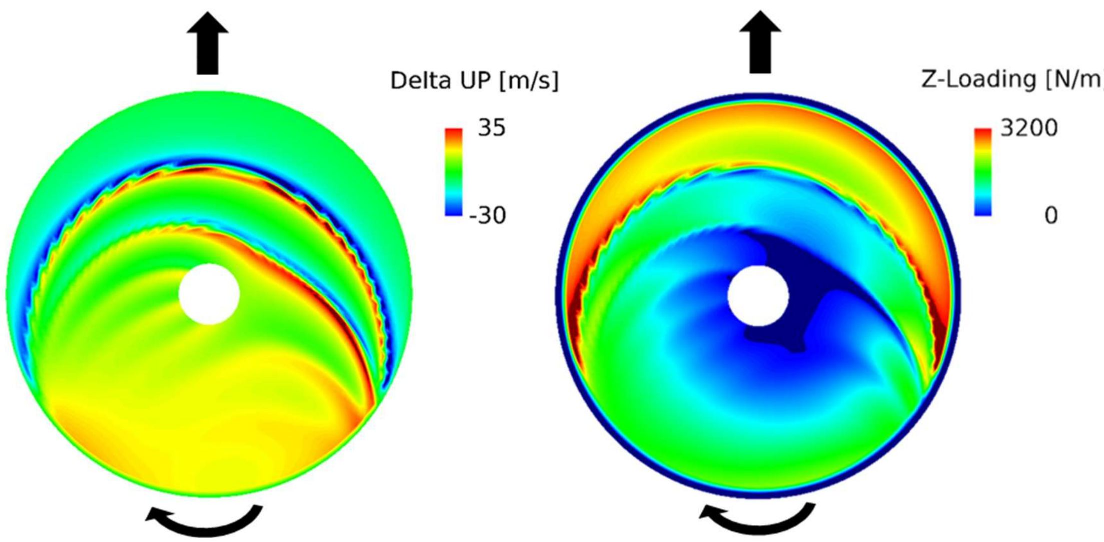

Figure 7.26: Disk plots for the tandem configuration rear rotor in segment 3 (left induced velocity profile, right loading perpendicular to the blade).

The loudest part of the signal is in the plane of the rotor, but the area below the plane of the rotor has significantly higher values of OASPL than the cases of climb or level flight. The BVI events increase the noise levels in this area of the plot. When looking at the OASPL for segment 3 in Figure 7.22, it is difficult so see any BVI effects for this segment. To study the BVI interactions more closely, BVISPL is plotted for both rotors in Figure 7.27. For this aircraft, the frequency range was calculated to be 78-445 Hz. The BVISPL frequency range is lower for the tandem than the helicopter case because the rotor only has three blades and the rotor is spinning at a slower angular rate (23.3 rad/s) than the helicopter main rotor (28 rad/s).

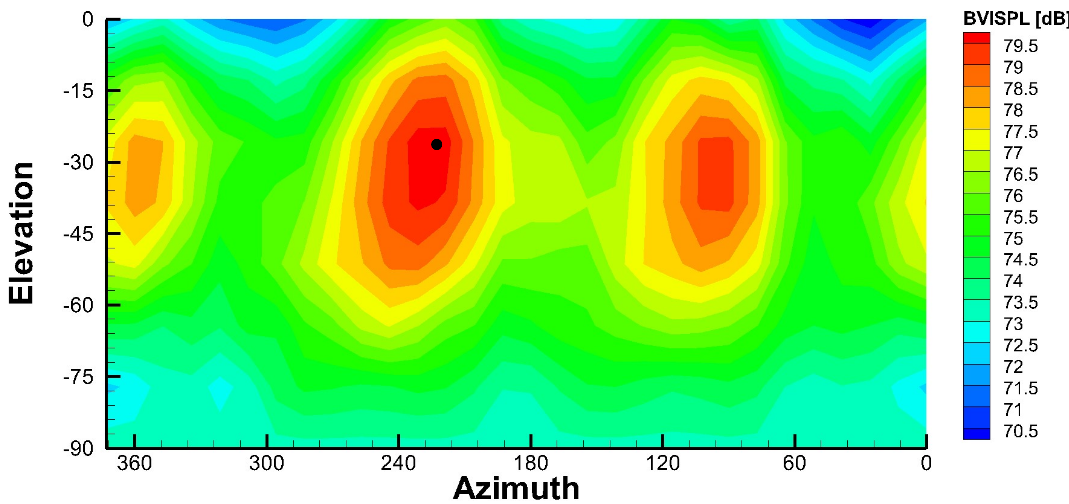

Figure 7.27: Loading BVISPL for a hemisphere of observers located 10 rotor radii (91.4 m) away from the front rotor hub for the tandem configuration in segment 3.

The BVISPL signal is highest on the rear rotor. When the BVISPL levels for each individual rotor are combined, the rear rotor dominates the total BVISPL signal. The highest signal occurs between 210° and 250° azimuth down to 45° below the plane of the rotor. This band of higher BVISPL extends more than 60° below the rotor. This occurs on the advancing side of the rear rotor. There is another significant region of BVISPL that occurs between 70° and 100° between 25° and 45° below the plane of the rotor. This occurs on the advancing side of the front rotor and the retreating side of the rear rotor.

An observer was placed in the location of maximum BVISPL. This observer is located at -26° elevation and 223° azimuth, and is indicated by a dot in Figure 7.27. The acoustic pressure time history and acoustic spectrum are plotted for this observer in Figure 7.28 and Figure 7.29. The acoustic pressure time history has high frequency jitters in the signal which are most likely numerical. The signal from both rotors interact at this location to result in a complex signal. There is a large peak in the acoustic pressure signal for this case. In the spectrum plot, the BVISPL frequency range (78-445 Hz) has significant dB levels.

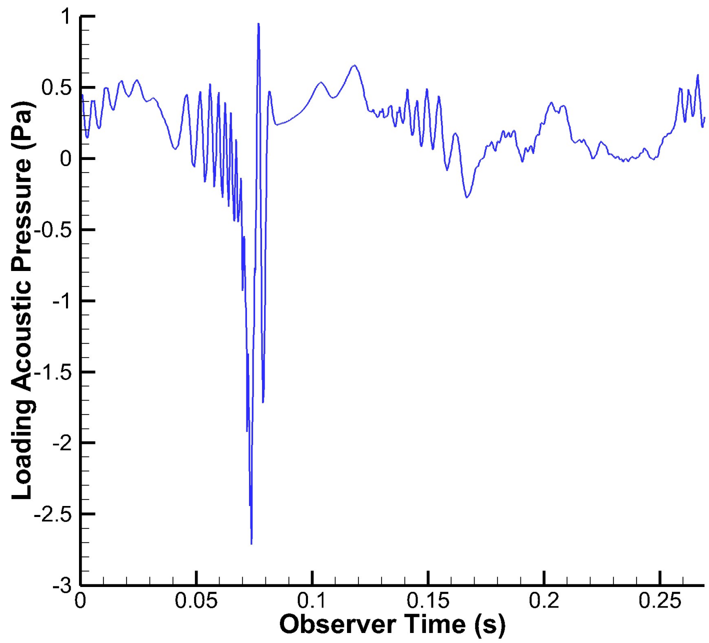

Figure 7.28: Acoustic pressure time history for observer located in the BVI hotspot for the tandem configuration in segment 3.

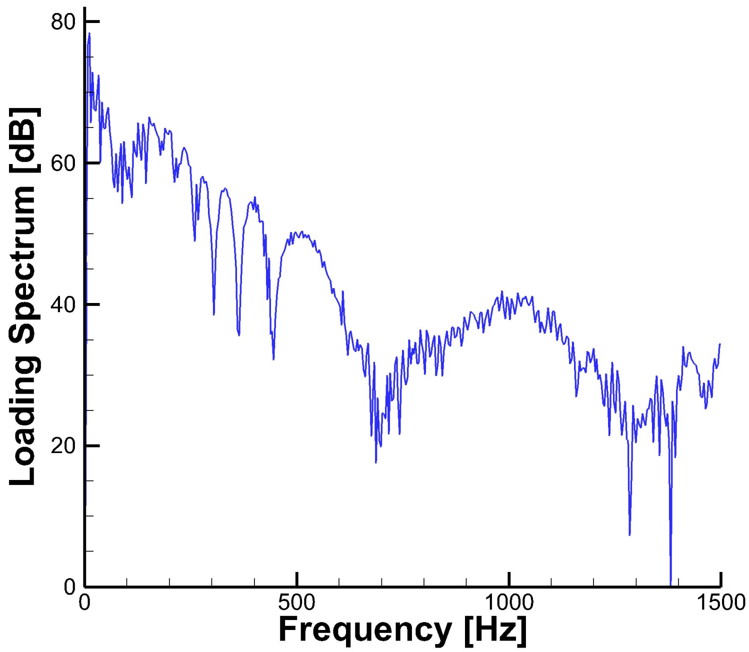

Figure 7.29: Acoustic spectrum for the observer located in the BVI hotspot for the tandem configuration in segment 3.

Segment 4 is a 1° descent for the tandem configuration. The forward velocity was 25.7 m/s ($\mu = 0.121$) and the descent speed was 0.51 m/s (100.4 ft/min). The wake trailing behind each rotor for segment 4 is shown in Figure 7.30. For a closer look at the potential blade-vortex interactions, the wake trailing behind the front rotor is shown in Figure 7.31. From the side view it is clear that the wake is farther away from the rotor plane than segment 3 because a 1° descent is not typically a BVI condition. There are not many segments of the wake close enough to the rotor to have significant BVI events. The induced velocity on the rotor disk with an identical scale to the previous case is shown in Figure 7.32. There are essentially no significant bands of induced velocity anywhere on the rotor disk when compared to segment 3. The BVISPL was calculated for the aircraft in this segment. The highest BVISPL level recorded for segment 4 is 66 dB. In comparison with the 6° descent, there is no practically significant BVISPL signal for any observer in the hemisphere. When plotted on an identical scale to segment 3, it would not register.

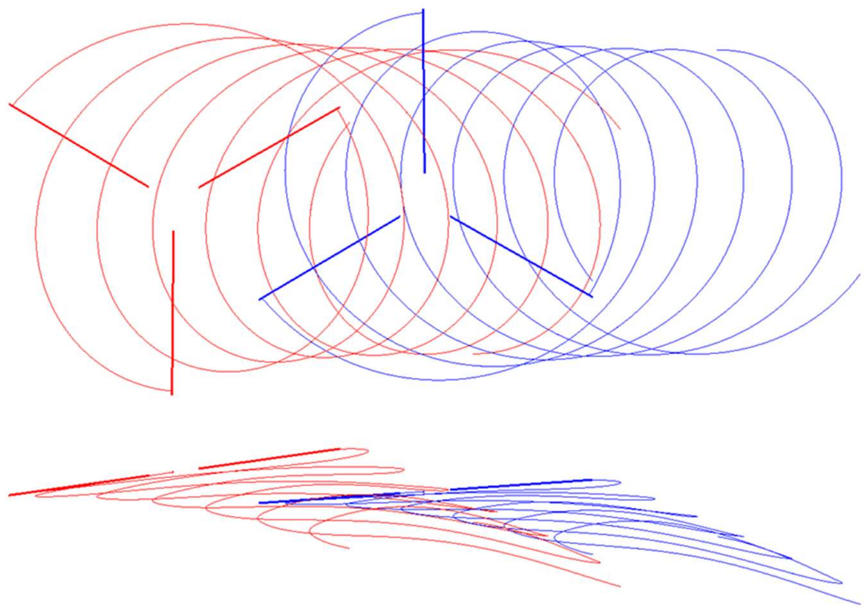

Figure 7.30: Top and side view of the wake generated for both rotors of the tandem configuration in segment 4.

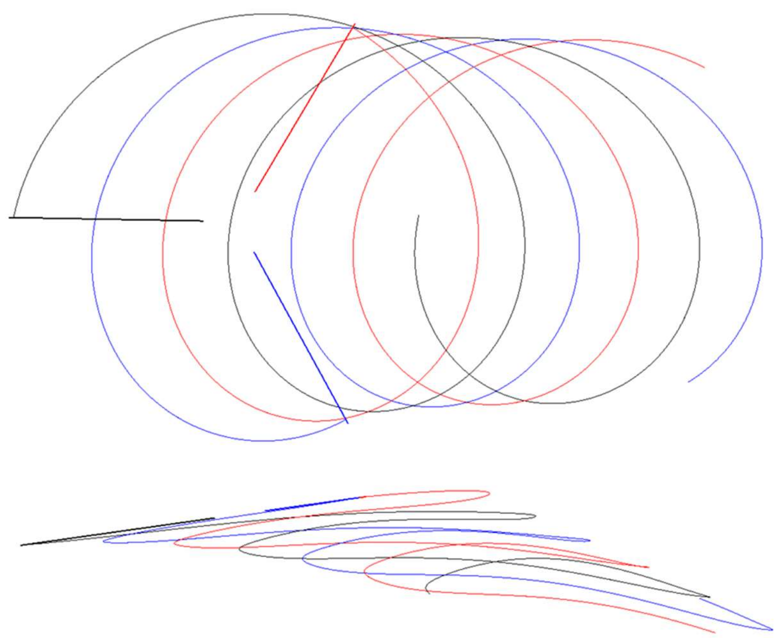

Figure 7.31: Top and side view of the wake generated for the tandem configuration's front rotor in segment 4.

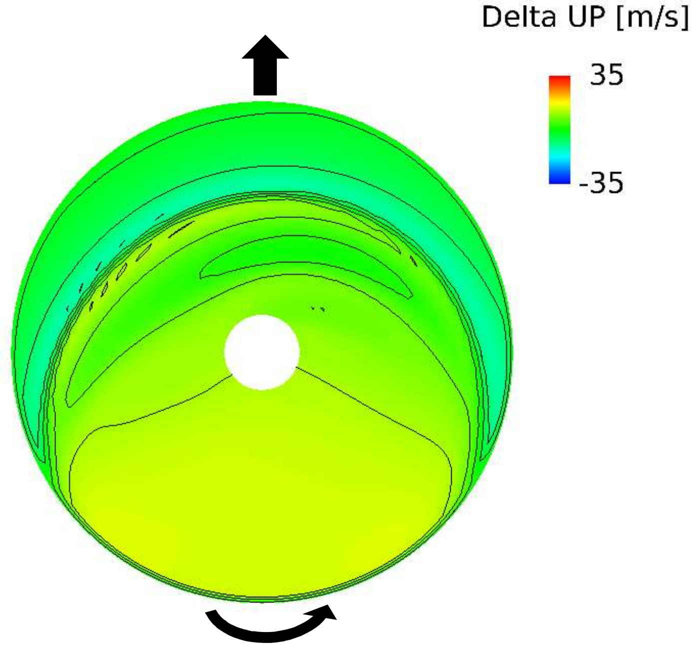

Figure 7.32: Induced velocity on the front rotor disk for the tandem configuration in segment 4.

Segment 5: Max Speed

In Segment 5 the tandem aircraft was operated at its top speed in level flight. For the tandem configuration, the maximum speed is 89 m/s ($\mu = 0.412$). Five observers were positioned in front of the aircraft 10 rotor radii (91.4 m) away from the center of the aircraft between the two rotor hubs at identical locations shown before in Figure 7.17. The acoustic pressure time history for the aircraft (both rotors) is plotted for each observer in Figure 7.33. The rotor radius is larger for the tandem than the conventional helicopter, so the observers are positioned farther away for this case. The increased radiation distance does increase the shearing effects that act on the signals in this case. The observers in plane, 13° below, and 26° below the rotor plane have M_r values of 0.90, 0.89, and 0.87, respectively. Each of these three signals experience a high shear that leads to shock fitting. As with the helicopter case, more shearing leads to slight amplitude loss for the observers in plane, 13° below the rotor plane, when compared to the observer 26° below the rotor plane. The effect that distance has on the HSI signal shear may be too extreme leading to shock fitting for observers with lower values of M_r. The model should be validated with HSI signals at long range so the empirical relations can be tuned. This is addressed again in chapter 8. The observers located 39° and 52° below the rotor plane have M_r values of 0.81 and 0.74, respectively. Neither of these signals require shock fitting. The signal at 39° below the rotor plane does show the signs of shearing the signal to mimic wave steepening. The amplitude of the signal decreases as the observers get farther from the plane of the rotor.

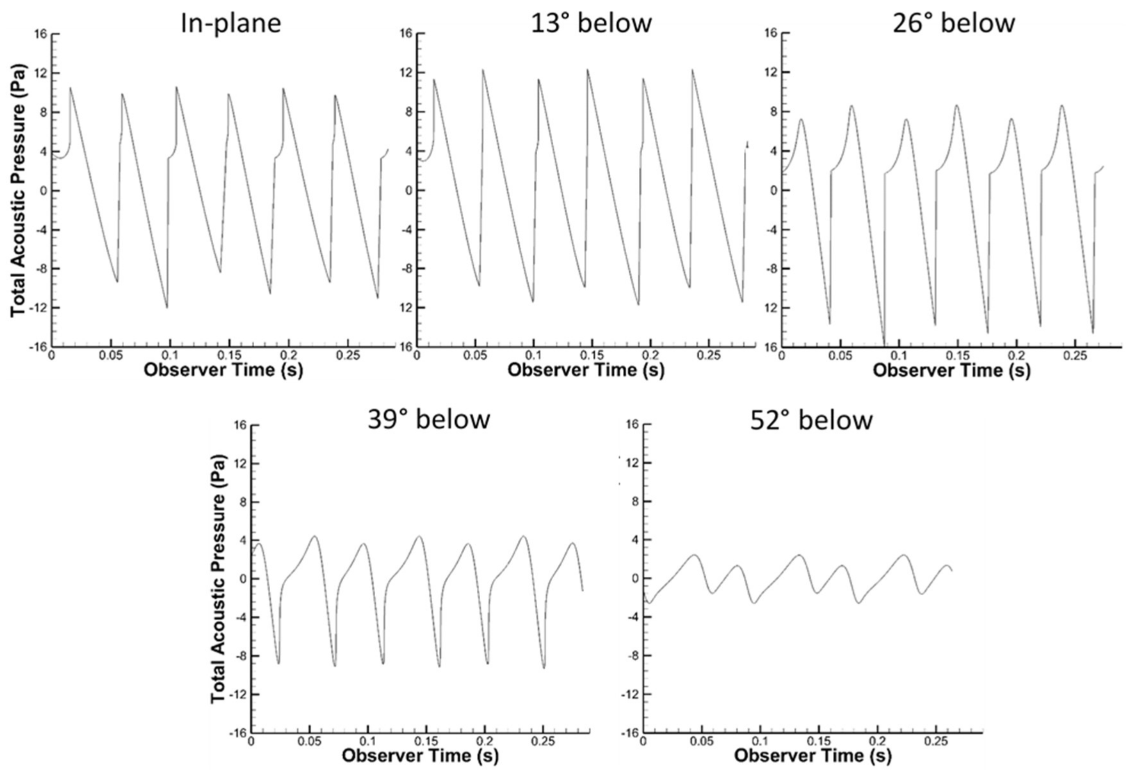

Figure 7.33: Acoustic pressure time history after HSI post-processing for an array of observers in front of the tandem aircraft in segment 5.

Segment 6: High-Speed Descent

In segment 6 the tandem operated the vehicle in high-speed descent. The aircraft flew with a forward flight speed of 77.17 m/s ($\mu = 0.362$) and a descent speed of 6.6 m/s (1300 ft/min). The trailing wake for this case is shown in Figure 7.34. Since the rotor is operating at a high advance ratio, the wake spreads out quickly. The trailing tip vortices from previous revolutions are sufficiently far enough from the rotor blades to induce a velocity, therefore the number of interactions are limited. This rotor also only has three blades, so there are less opportunities for trailing tip vortices to interact with subsequent blades over each rotor revolution. From the side view, it is clear that the tip vortices travel in the plane of the rotor. The rotor does interact with the part of the wake that has the lowest wake age. The induced velocity profile due to these interactions and the resulting blade loading are plotted across the rotor disk in Figure 7.35. There are a few clear bands of interaction on the rotor disk. These interaction have an effect on the overall blade loading, however they are not as severe as the BVI case in segment 3.

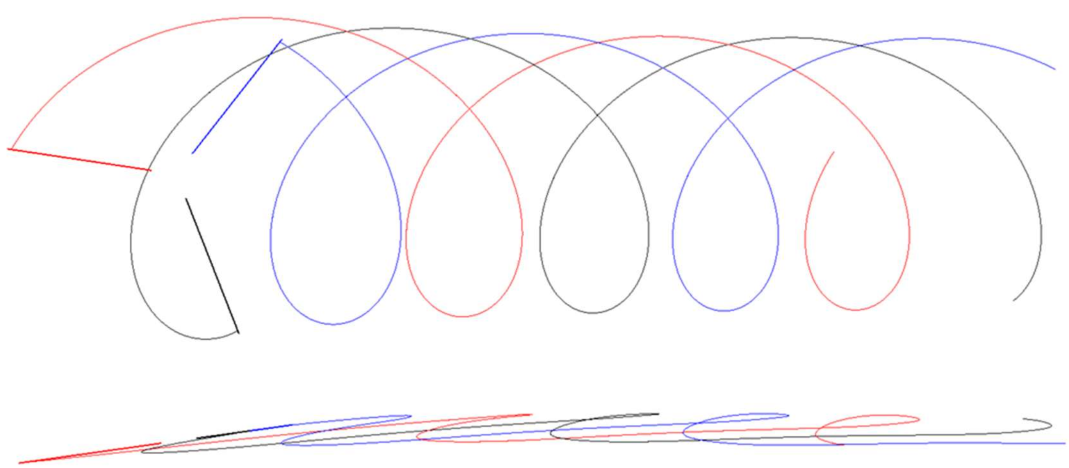

Figure 7.34: Top and side view of the wake generated for the tandem configuration's front rotor in segment 6.

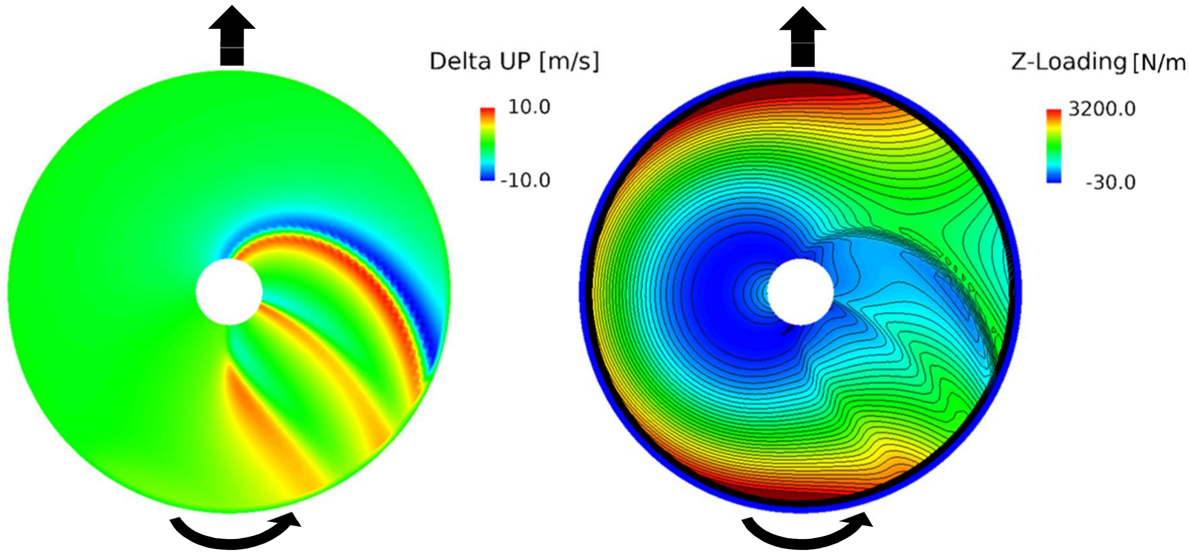

Figure 7.35: Disk plots for the tandem configuration front rotor in segment 6 (left induced velocity profile, right loading perpendicular to the blade with contours).

Five observers were placed at identical locations as to the previous HSI cases (shown in Figure 7.17), and the acoustic pressure time history for each observer is plotted in Figure 7.36. These observer locations are not ideal for BVI noise, but they were chosen to show the HSI effects interacting with BVI. The computed maximum M_r values for the in-plane observer and observer 13° below the rotor plane were 0.86 and 0.85, respectively. These cases shear and receive shock fitting. The effects of BVI become more apparent for observers further from the observer plane. The signal for the observer 26° below the rotor plane experiences some small BVI-like impulsive pressure spikes on top of the HSI dominated signal. These small impulses change the shape of the overall signal, but the pulse amplitude is largely unaffected. The observers located 39° and 52° below the rotor plane experience clear BVI patterns. There are clearly defined BVI impulses in the time history that dominate the signal at these locations. The maximum M_r on the rotor blade calculated for these observer positions are 0.77 and 0.69, respectively. These signals are amplified and sheared, but shock fitting is not necessary.

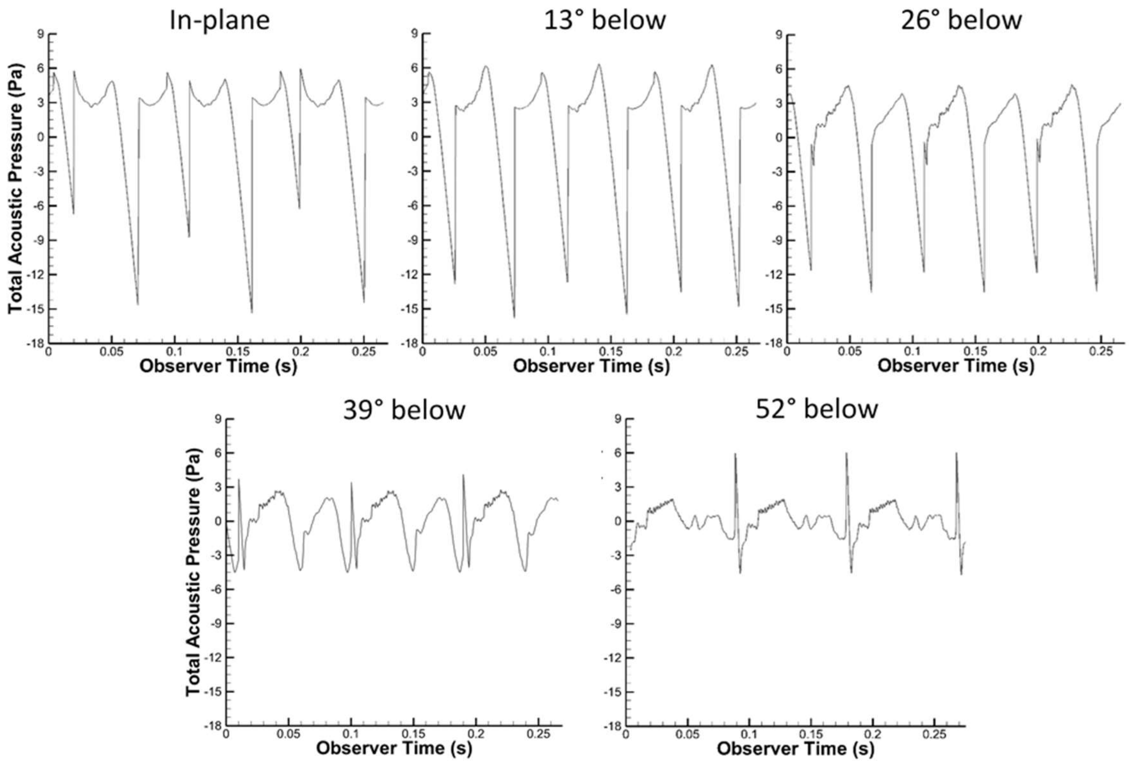

Figure 7.36: Acoustic pressure time history after HSI post-processing for an array of observers in front of the tandem aircraft in segment 6.

Coaxial Helicopter

This section studies the acoustic output for a coaxial configuration undergoing the same mission as the previous two aircraft. The OASPL values for a hemisphere of observers 10 rotor radii (61 m) away from the hub of the upper rotor in segments 1-4 are shown in Figure 7.37. The best rate of climb (segment 1) for the coaxial configuration was a forward flight speed of 40.6 m/s ($\mu = 0.204$) and a climb speed of 5 m/s (988 ft/min). For this segment, the maximum OASPL occurred between 200° and 220° azimuth down to 30° below the rotor plane. There is a similar smaller spike between 120° and 160° azimuth. Just like the tandem case, the advancing side of each rotor is on the opposite side of the aircraft due to the rotors counter-rotating.

Segment 2 represents the aircraft at its best endurance speed for level flight. For the coaxial configuration, this was a forward flight speed of 41.5 m/s ($\mu = 0.209$). The OASPL values for segment 2 are similar to those in segment 1 but a few dB higher. The area that contains the peak OASPL signal has expanded to cover a large portion of the observer hemisphere. Observers between 120° and 240° azimuth experience higher OASPL values than when the aircraft was in climb. This signal extends more than 40° below the plane of the rotor.

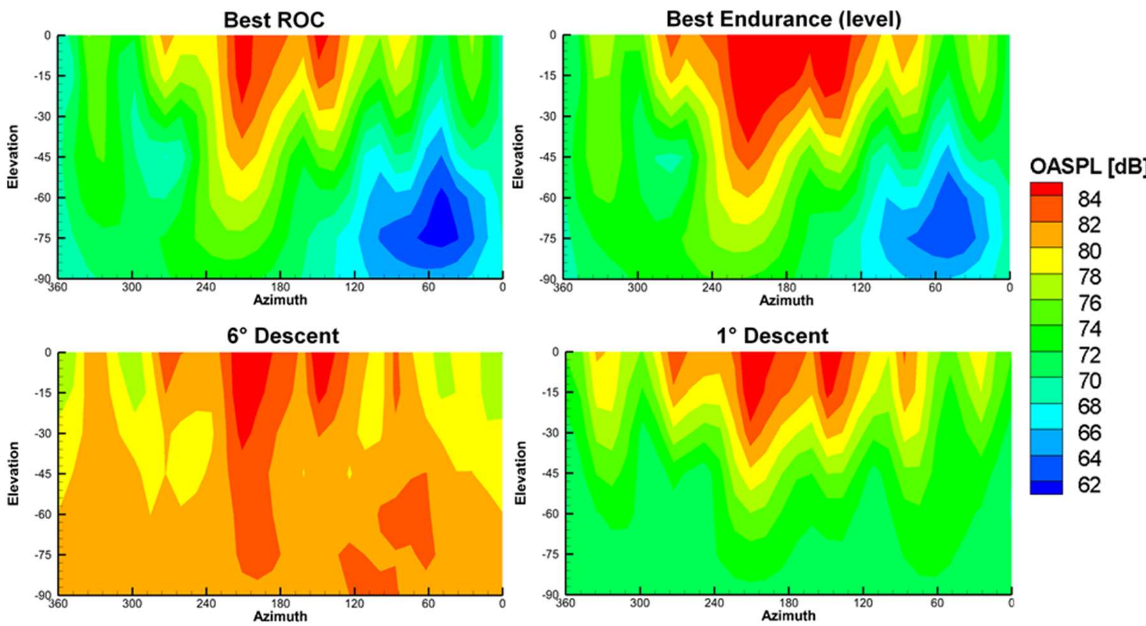

Figure 7.37: OASPL values mapped from a hemisphere of observers for the coaxial configuration in segments 1-4.

Segments 3-4: Descent

In segment 3 the aircraft operated in a prescribed 6° descent to highlight BVI. The forward speed in segment 3 was 25.7 m/s ($\mu = 0.130$) and the helicopter descent speed was 2.7 m/s (531.5 ft/min). It is clear upon examining the OASPL plot in Figure 7.37 that the noise levels have dramatically increased for observers in all directions. To study the BVI effects, the wakes trailing behind the aircraft are plotted in Figure 7.38. It is important to note that each wake is unaffected by the other rotor or the other rotor's wake. To get a closer look at the tip vortices that can induce a velocity on the rotor disk, the trailing tip vortex geometry is plotted for the lower rotor in 6° descent in Figure 7.39 using the same conventions as before. The snapshot in time used for the top view is capturing 2 parallel interactions at once. One is near the root of the advancing blade (top) and the other is more than halfway along the span of the retreating blade (bottom). In the side view it is clear that the rotor is operating in its own wake. The tip vortices travel above the rotor before dropping back below the rotor plane. This means that the tip vortices remain relatively close to the rotor plane over a larger part of the rotor disk. Multiple passes of the wake remain close enough to the blade to induce significant unsteady effects onto the rotor. The induced velocity profile and resulting blade loading are plotted across the rotor disk for the upper rotor in Figure 7.40 and lower rotor in Figure 7.41 using the same conventions used in previous figures. The induced velocity profile and rotor loading are very similar. On each disk, there are two strong BVI interactions on the upper half of the figure. There are also distinct smaller interactions on the advancing side of the rotor. It is evident in from the loading plots that all of these interactions clearly had a significant influence on the blade loading. These unsteady loads that impulsively jump up and down in loading indicate a strong BVI interaction. The "scalloping" pattern in each band of interaction is a numerical anomaly.

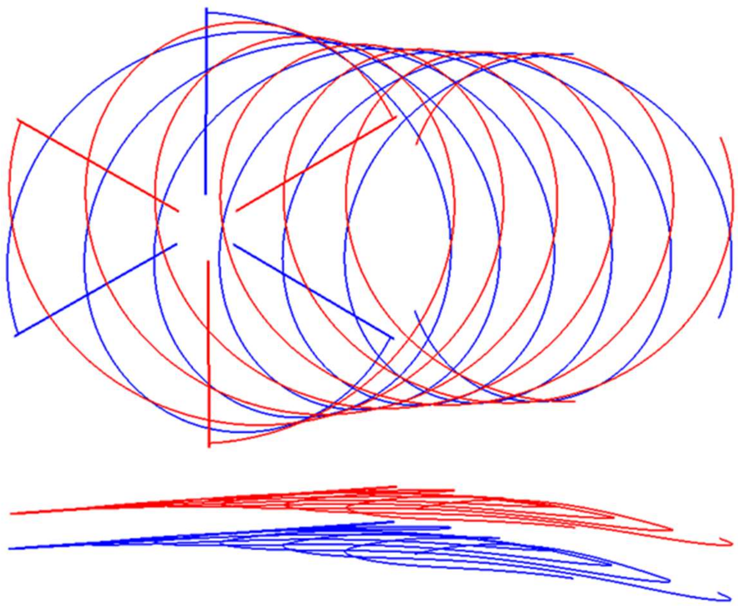

Figure 7.38: Top and side view of the wake generated for both rotors of the coaxial configuration in segment 3.

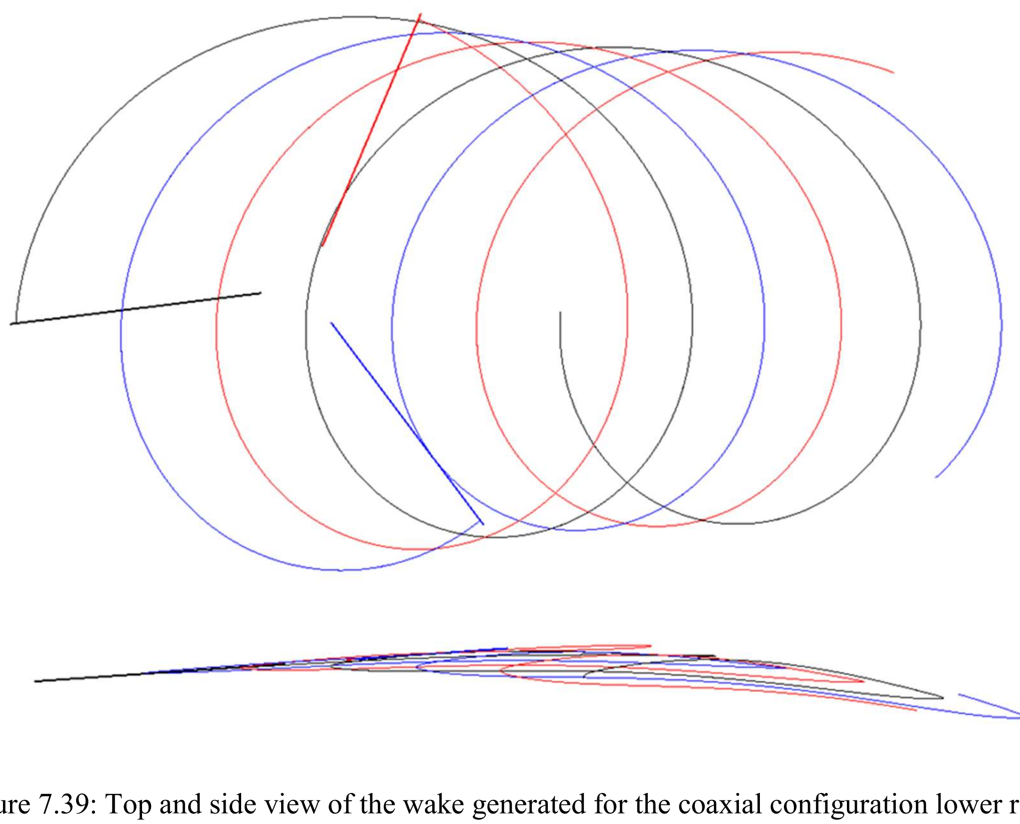

Figure 7.39: Top and side view of the wake generated for the coaxial configuration lower rotor in segment 3.

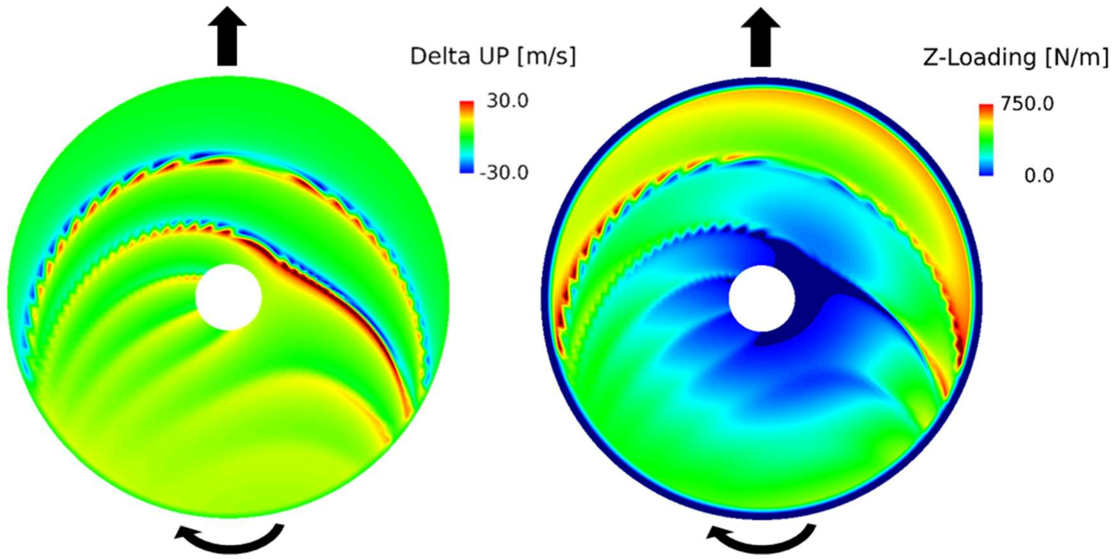

Figure 7.40: Disk plots for the coaxial configuration upper rotor in segment 3 (left induced velocity profile, right loading perpendicular to the blade).

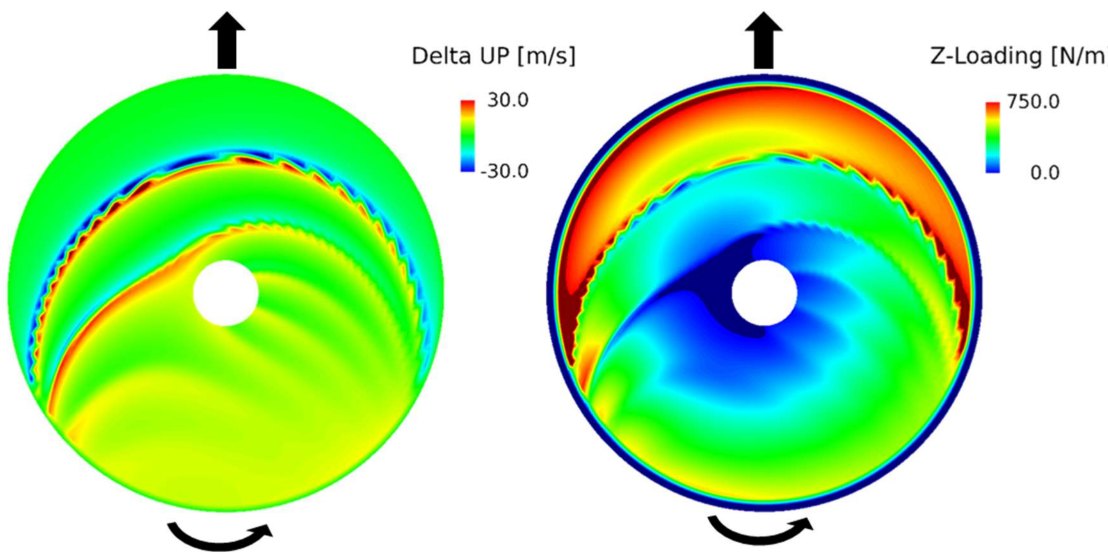

Figure 7.41: Disk plots for the coaxial configuration lower rotor in segment 3 (left induced velocity profile, right loading perpendicular to the blade).

To study BVI events more closely, the BVISPL is mapped for the hemisphere of observers in Figure 7.42. For this aircraft the BVISPL was computed with the 7th-40th harmonics – approximately 108-621 Hz. This BVISPL frequency range falls between that of the helicopter and tandem because it has a higher rotational speed and three blades. The BVISPL signals are strong below the plane of the rotor. High BVISPL levels occur for observers between 30° and 80° below the rotor plane in many directions. The complex directivity of the BVISPL signal is a result of signals from two rotors being combined. There are distinct regions that have high BVISPL signals. These regions correspond to the BVI events that occurred on the advancing and retreating sides of each rotor. The noise levels are high below the aircraft (elevation of -90° is the point directly below the rotor) for this segment. These BVI interactions explain the dramatic increase in OASPL levels for this segment.

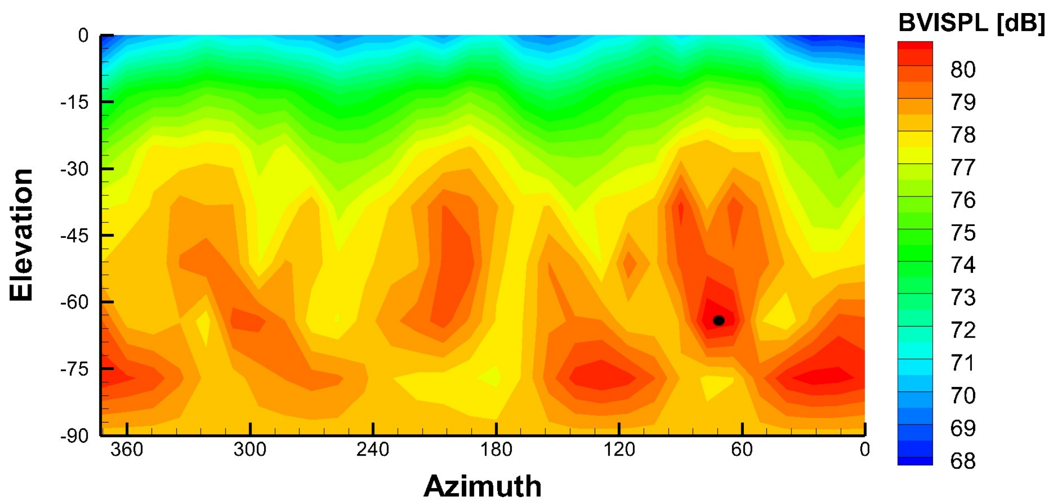

Figure 7.42: Loading BVISPL for a hemisphere of observers located 10 rotor radii (64 m) away from the upper rotor hub for the coaxial configuration in segment 3.

An observer was placed in the location that registered the highest BVISPL located at -64° elevation and 78° azimuth. This observer location is indicated by a dot in Figure 7.42. The acoustic pressure time history for this observer location is plotted in Figure 7.43, and the acoustic spectrum for this observer location is plotted in Figure 7.44. In the acoustic pressure time history it is clear that this is a BVI condition. There are three clear spikes that dominate the signal. The amplitude rapidly reaches its peak before dropping back towards the normal signal. This rapid jump shows a clear impulsive interaction. The spectrum plot shows high decibel values for a large frequency range. The BVISPL window (109-621 Hz) has a very high amplitude. It is clear that the coaxial configuration experiences a strong BVI interaction for this 6° descent case. The high frequency perturbations seen in these acoustic pressure time history plots are most likely numerical, and may result from the unsteady loading patterns. This should be studied further.

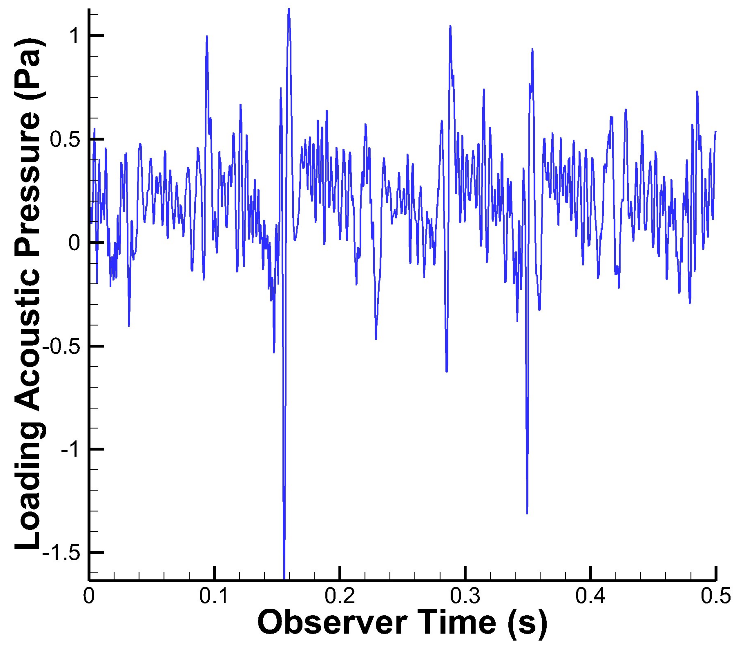

Figure 7.43: Acoustic pressure time history for an observer in the BVI hotspot for segment 3 for the coaxial configuration.

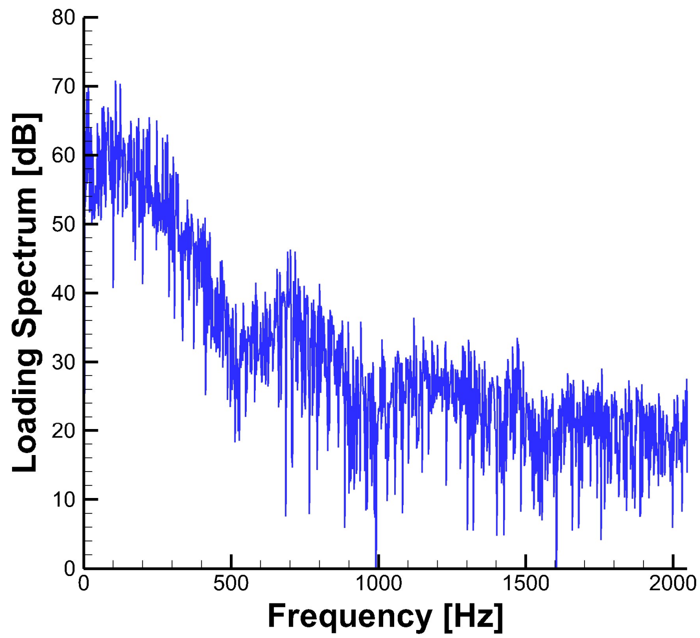

Figure 7.44: Spectrum for an observer in the BVI hotspot for segment for the coaxial configuration.

Segment 4 prescribed the aircraft fly a 1° descent. The forward velocity was 25.7 m/s ($\mu = 0.130$) and the descent speed was 0.51 m/s (100.4 ft/min). The wake calculated for this segment is shown in Figure 7.46. The wake drops off much more quickly for this segment. The rotor is rarely operating in its own wake which severely limits the potential interactions around the rotor disk. Looking at OASPL values, the 1° descent case is closer to the first two segments than it is to segment 3 (the 6° descent case). When the BVISPL results were calculated for segment 4, there wasn't a single observer in the hemisphere that registered a significant increase over the baseline noise level compared to those in segment 3. The maximum BVISPL value for segment for was 57 dB. This is more than 22 dB lower than maximum for segment 3, and when plotted on the same scale as Figure 7.42 it will not even register. It is clear that BVI is not a significant factor for the tandem in this 1° descent case.

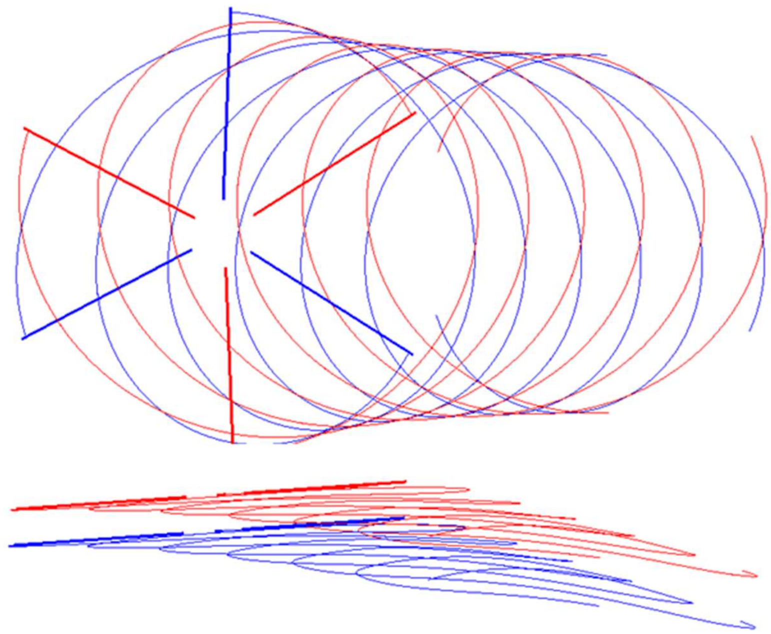

Figure 7.45: Top and side view of the wake generated for both rotors of the coaxial configuration in segment 4.

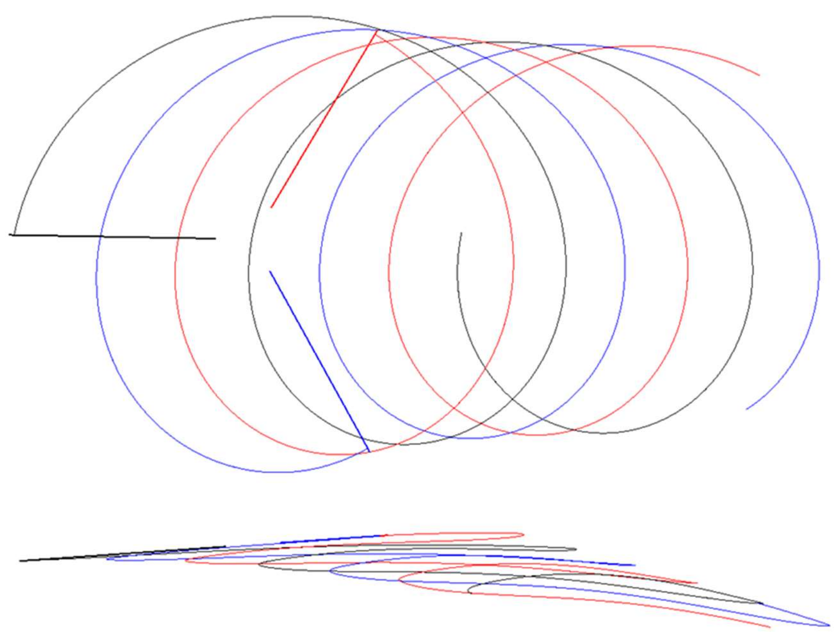

Figure 7.46: Top and side view of the wake generated for the coaxial configuration lower rotor in segment 4.

Segment 5: Max Speed

Segment 5 corresponds to the vehicle operated at its maximum speed in level flight. For the coaxial configuration, this speed is 84.8 m/s ($\mu = 0.425$). Observers were placed at the five locations in front of the aircraft previously shown in Figure 7.17. The acoustic pressure time history for the aircraft is plotted for each observer in Figure 7.47. Because the two rotors rotate about the same axis and the observers are along the centerline of the aircraft, there are only three pulses in the acoustic pressure time history. The rotor radius for the coaxial helicopter is smaller than the previous two aircraft so the observers are closer to this case ($10R = 61$ m), which does reduce the amount of shearing that the signal receives. The maximum M_r values calculated for an in-plane observer and observer located 13° below the rotor plane are 0.84 and 0.83, respectively. These signals are amplified and sheared accordingly, and the signals are shock fit where necessary. Observers at locations further from the plane of the rotor experience smaller pulse amplitudes. The observers located 26°, 39°, and 52° below the rotor plane correspond to M_r values of 0.81, 0.76, and 0.68, respectively. The lower amplitude combined with the smaller shearing applied results signals that do not need shock fitting.

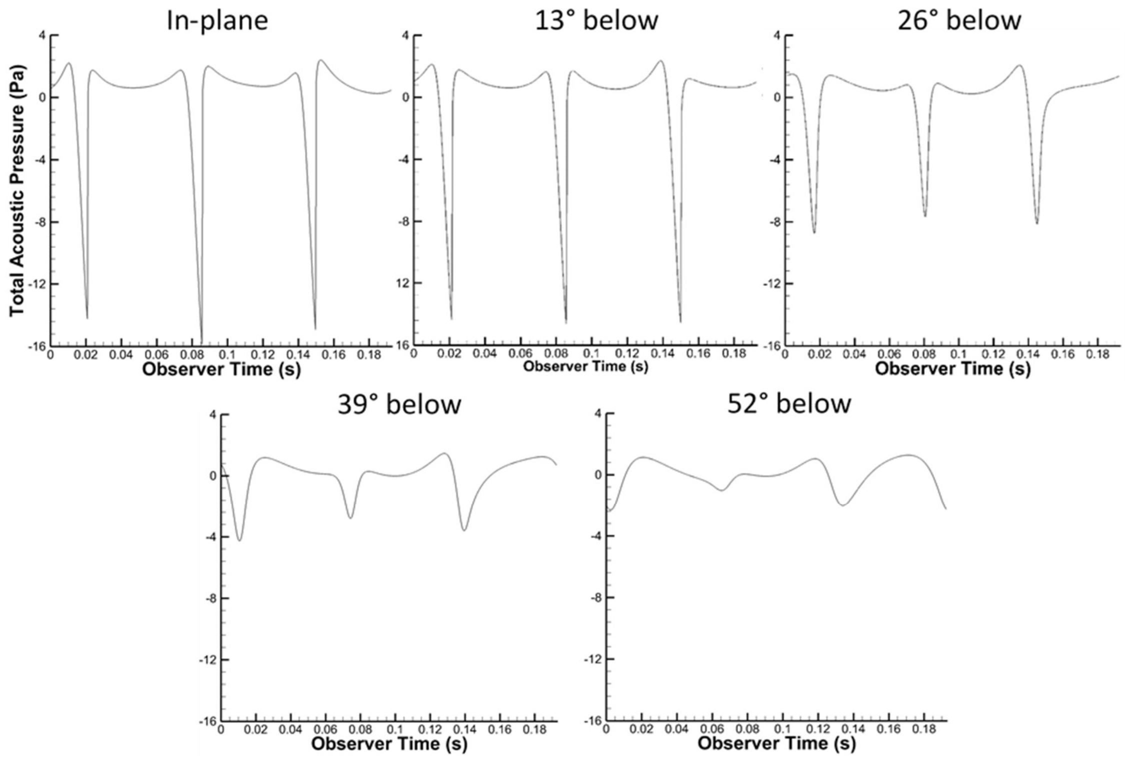

Figure 7.47: Acoustic pressure time history after HSI post-processing an array of observers in front of the coaxial aircraft in segment 5.

Segment 6: High-Speed Descent

In segment 6 the coaxial helicopter operated in a high-speed descent. The aircraft flew with a forward flight speed of 77.17 m/s ($\mu = 0.390$) and a descent speed of 6.6 m/s (1300 ft/min). The wake that trails behind this rotor is plotted in Figure 7.49. Due to the higher advance ratio, the wake spreads out quickly limiting the possible interactions. From the side view, it is clear that the wake will interact with the rotor for the early revolutions. The induced velocity caused by the wake and the resulting blade loading is plotted across the rotor disk in Figure 7.50. There are a few bands of interactions on the rotor disk. These interactions have less impact than the more intense BVI case in segment 3.

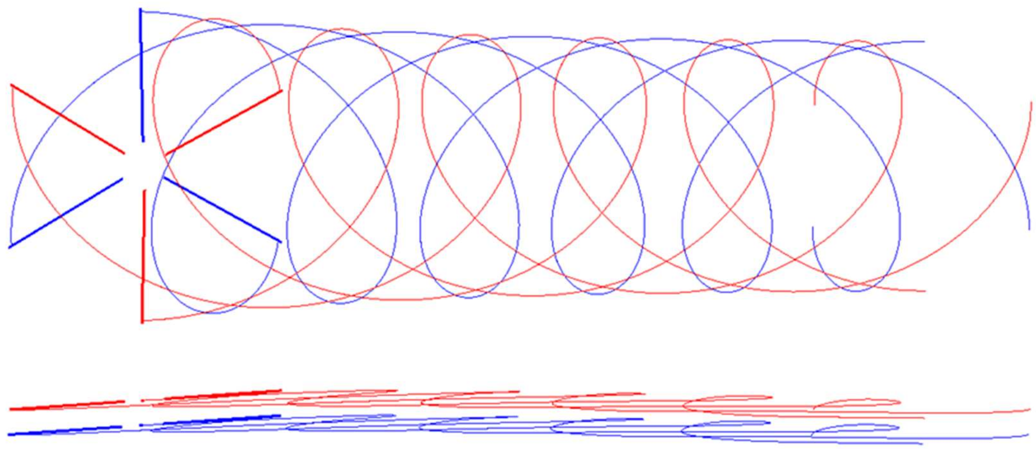

Figure 7.48: Top and side view of the wake generated for both rotors of the coaxial configuration in segment 6.

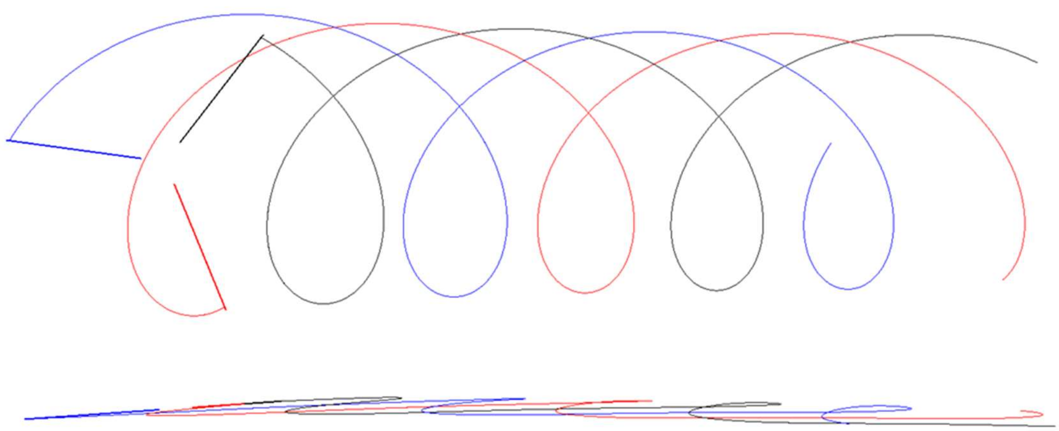

Figure 7.49: Top and side view of the wake generated for the coaxial configuration lower rotor in segment 6.

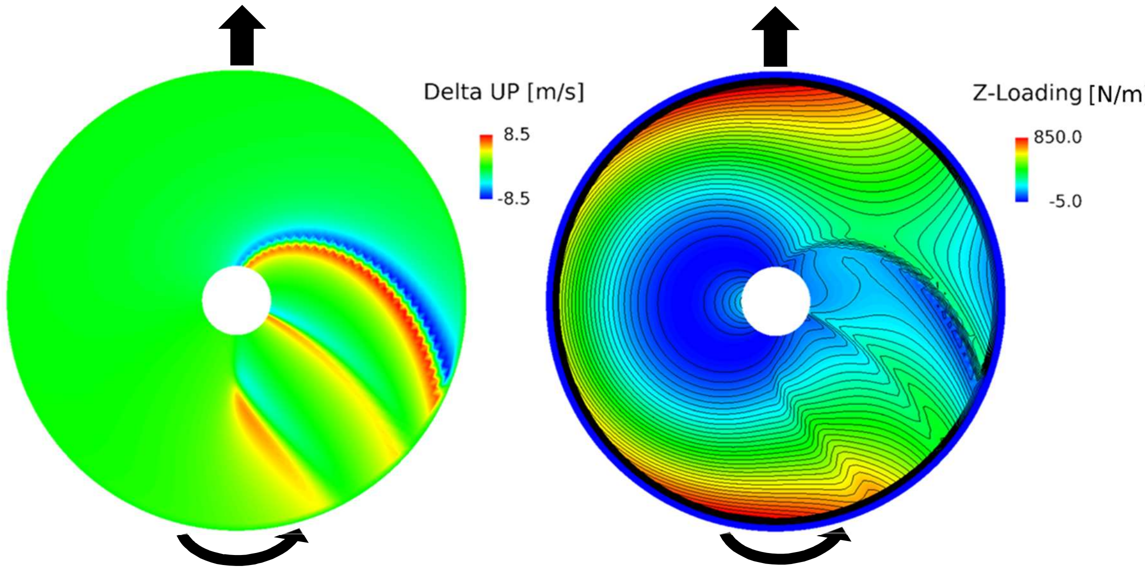

Figure 7.50: Disk plots for the coaxial configuration lower rotor in segment 6 (left induced velocity profile, right loading perpendicular to the blade with contours).

Observers are placed at the five locations shown in Figure 7.17. These acoustic pressure time histories are plotted for each observer location in Figure 7.51. The observer in the plane of the rotor has an M_r value of 0.81 for this case. This is comparable to the M_r calculated for the observer located 26° below the rotor in segment 5. The shearing associated with this Mach number does not result in shock fitting, which is similar to the previous segment. None of the observer locations have a high enough value of M_r to result in shock fitting for this aircraft. However, the effects of shearing can be seen in the signals for observers close to the rotor plane. The other four observers have M_r values of 0.8, 0.78, 0.74, and 0.66, respectively. The BVI impulses begin to become noticeable for the observer 26° below the rotor plane. There are small impulses that occur along the signal that change the shapes of the peaks and occur between peaks as well. There are much more significant BVI impulses for the observers located 39° and 52° below the rotor plane. These impulses are comparable to the overall pulse amplitude. It is clear that the unsteady interactions experienced for this flight condition are not as significant as the BVI effects like those shown in the 6° descent case (segment 3).

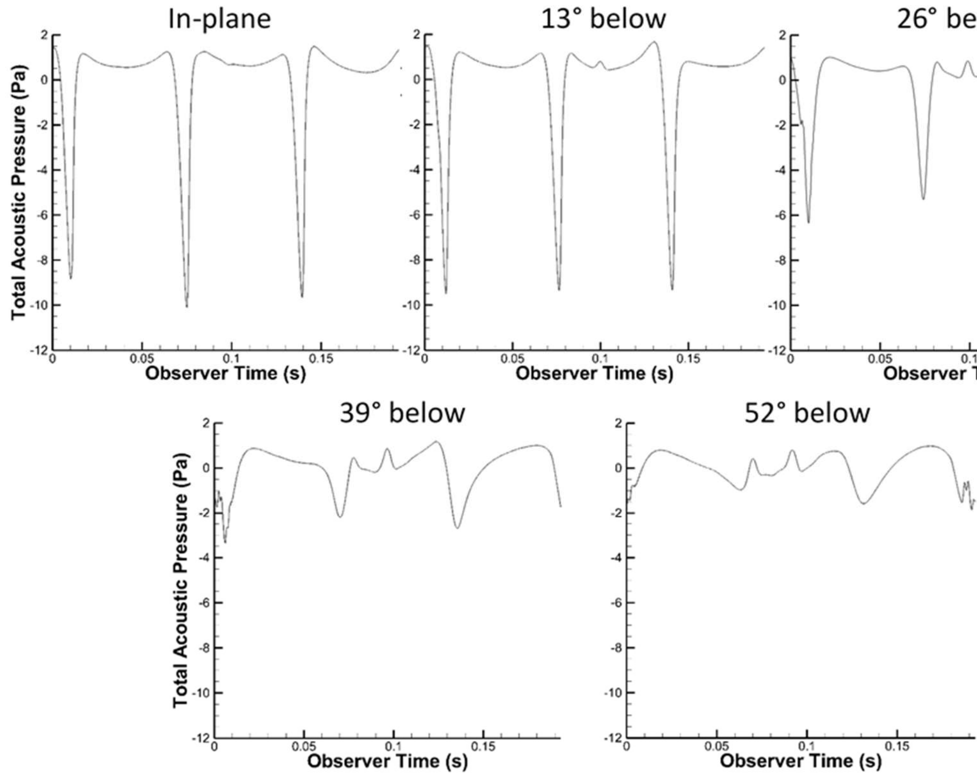

Figure 7.51: Acoustic pressure time history after HSI post-processing for an array of observers in front of the coaxial aircraft in segment 6.

Hexacopter

The hexacopter has six equally sized rotors. There are two rotors along the centerline of the aircraft, one in the front and one in the back. There are four more equally spaced rotors between the front and back rotor that are off the left and right of the aircraft. The OASPL is plotted Figure 7.52 for a hemisphere of observers 10 rotor radii (30.5 m) away from the center of the configuration for segments 1-4 . In segment 1 the aircraft is trimmed to its best rate of climb. For this aircraft, it was a forward velocity of 34.84 m/s ($\mu = 0.161$) and a climb velocity of 2.97 m/s (584.6 ft/min). The OASPL signal is greatest from 0° to 30° below the plane of the rotors. Segment 2 is when the aircraft was operated at its best endurance velocity. This velocity was 44 m/s ($\mu = 0.205$) for a level flight condition. The noise in level flight is significantly higher than the climb segment. In the plane of the rotor between 100° and 240° azimuth there is a high OASPL signal. This region of high OASPL extends as low as 60° below the rotor in directly in front of the aircraft. Having six rotors spread around the center of the observer sphere may contribute to the unique acoustic directivity for this aircraft. There are multiple bands of higher and lower OASPL signals. The level flight condition has the highest OASPL values. The descent cases have higher magnitudes than the best rate of climb case.

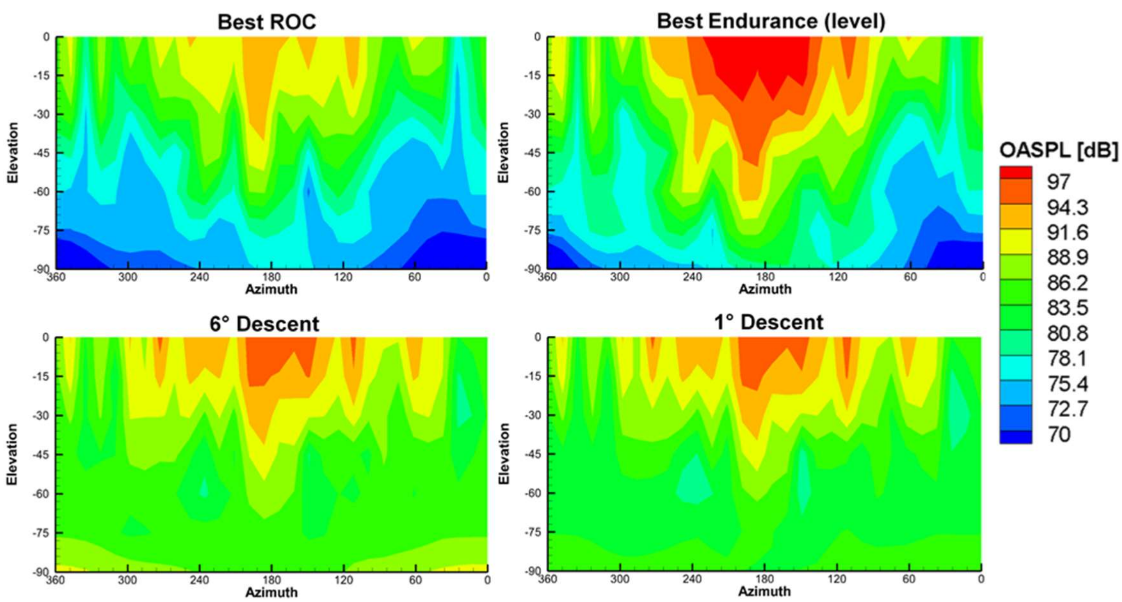

Figure 7.52: OASPL values mapped from a hemisphere of observers for the hexacopter configuration in segments 1-4.

Segments 3-4: Descent

Segment 3 was designed to check potential BVI conditions for the aircraft, while segment 4 was designed to show a descent case that would not be as affected by BVI. However, the trim for this aircraft does not result in a BVI condition for either of these descent cases. The control variables and pitch angle of the overall aircraft affect the values of μ_x and μ_z that are assigned by

NDARC for each individual rotor. Even though the vehicle is executing the 6° descent case, the rotor is experiencing flow velocities that are equivalent to a 1.5° descent. This may be due to the fact that the hexacopter is smaller, or that the speeds used in this mission are undesirable for this vehicle configuration. The wake trailing behind all six of the hexacopter's rotors in segment 3 is shown in Figure 7.53. To get a closer look at one rotor plane, the wakes shown for the hexacopter's front rotor in both segment 3 and 4 are shown in Figure 7.54. The wake drops off quickly, so there are little to no unsteady interactions added to the blade loading. Plotting BVISPL for this aircraft showed no significant BVI signals, and the disk plots for loading had no significant alterations from the BVI model. This also explains why the OASPL plots for segments 3 and 4 are nearly identical.

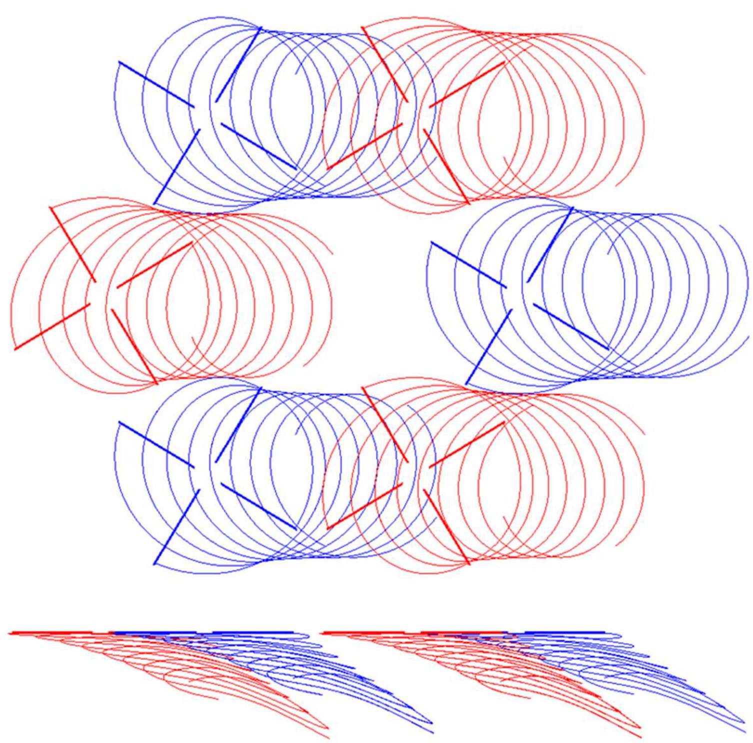

Figure 7.53: Top and side view of the wake generated for the six rotors of the hexacopter in segment 3.

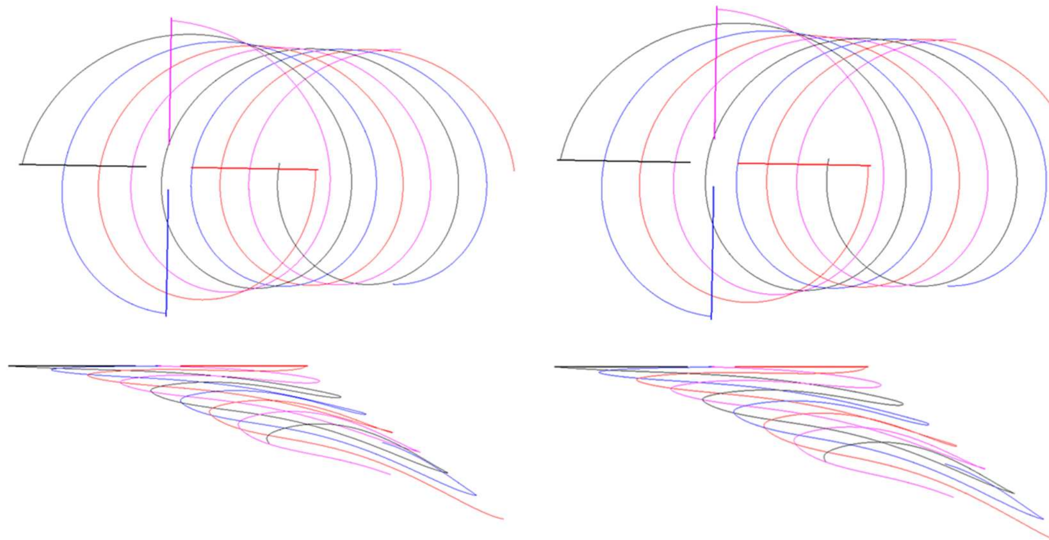

Figure 7.54: Top and side view of the wakes generated for the hexacopter configuration front rotor (left segment 3, right segment 4).

Segment 5: Max Speed

Segment 5 operated the aircraft at its maximum velocity. For this aircraft it was determined to be 79.6 m/s ($\mu = 0.355$) in level flight. Five observers were placed at the locations in front of the aircraft shown previously in Figure 7.17. The acoustic pressure time history for each rotor is post-processed individually based on the maximum M_r value and the radiation distance to the observer. Once the signal is calculated for each rotor, they are added together resulting in the acoustic pressure time history for the entire aircraft. The post-processed acoustic pressure time history for the aircraft is plotted for each observer in Figure 7.55. The signals for this aircraft have many more peaks than the previous aircrafts, because the signals from six different rotors are being combined into one. Each rotor has its own thickness and loading signal, and each rotor has a slightly different distance and directivity to the observer position. The observers are still positioned 10 rotor radii (30.5 m) from the aircraft, however since the hexacopter has a much smaller blade radius the observers are closer than any other configuration. The maximum value of M_r calculated for the in-plane observer is 0.86. The signal is sheared and results in shock fitting for several peaks. Due to the angle of the rotor, the observer 13° below the rotor has a slightly higher value of M_r. The maximum M_r calculated for this case is 0.87. The amplitude is highest for this observer, and the shearing and shock fitting are evident for the peaks in this signal. The observer 26° below the rotor plane has a maximum value of M_r of 0.85. The signal at this observer position is sheared and shock fit accordingly. The superposition of signals from six rotors interact constructively and destructively at different locations resulting in a very complex signal pattern. The two observers further from the rotor plane (39° and 52° below the rotor plane) have maximum M_r values of 0.80 and 0.76, respectively. The signals have much lower amplitudes here. In the signal for the observer 39° below the rotor the effects of shearing can be seen on some of these peaks, but no shock fitting is required. The amplitude for the observer furthest from the rotor plane (52°) is much smaller.

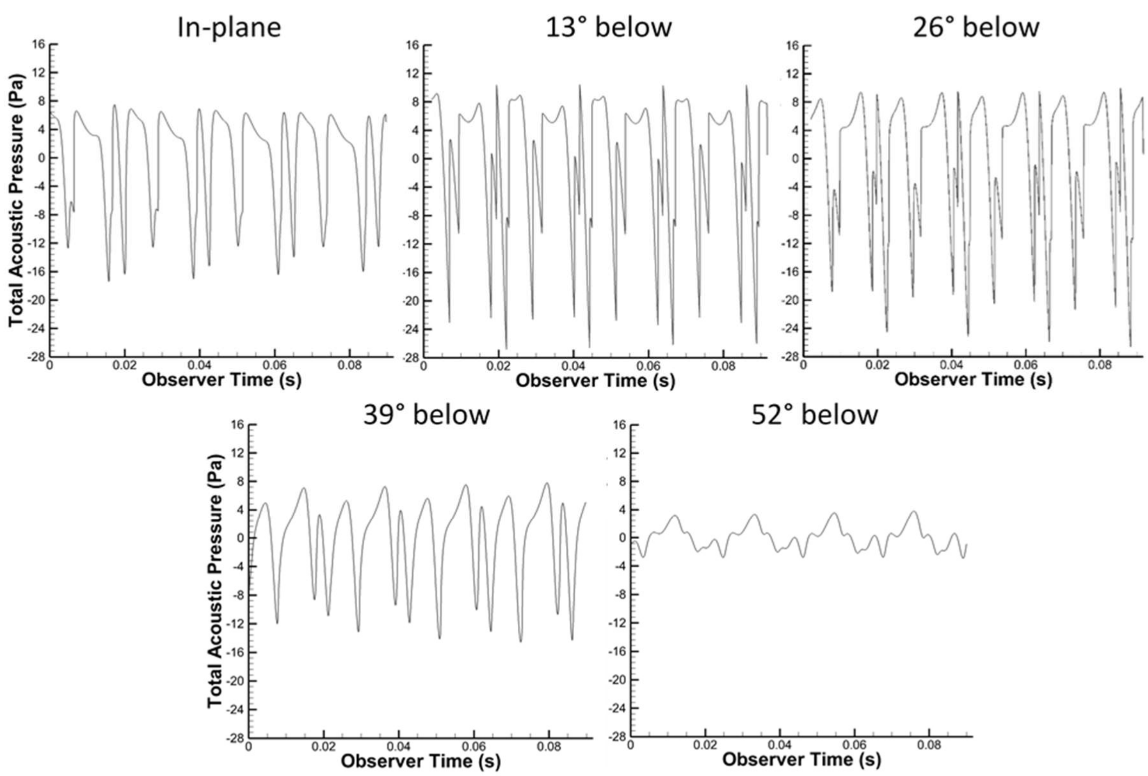

Figure 7.55: Acoustic pressure time history after HSI post-processing for an array of observers in front of the hexacopter in segment 5.

Segment 6: High-Speed Descent

In segment 6 the aircraft operates in a high-speed descent case identical to the other vehicles. The wake that trails behind the rotor is plotted in Figure 7.56. From the side view of the aircraft, it is clear that the wake drops below the rotor very quickly. Similar to segment 3, the trim of the rotors do not put this aircraft in a BVI condition for this specific flight condition. The wake is so far from the rotor that there will be no significant blade-vortex interactions.

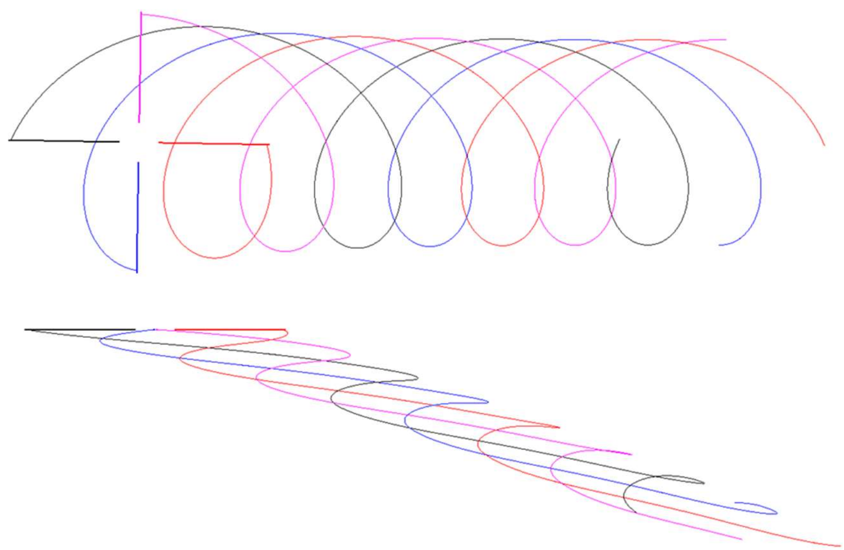

Figure 7.56: Top and side view of the wakes generated for the hexacopter configuration front rotor in segment 6.

Observers were placed at the 5 locations in front of the aircraft shown in Figure 7.17. The acoustic pressure time history is plotted for each observer in Figure 7.57. Since there are no significant BVI effects, the signals look very similar to the previous segment. In fact, segment 6 operates 6° descent with a forward flight speed of 77.2 m/s, which is very close to the top speed of 79.6 m/s in segment 5. The maximum M_r value for each rotor at every observer is extremely similar to the previous case. This explains why the results are so similar. The in-plane observer has an M_r value of 0.85. This shears the signal and results in shock fitting for multiple peaks.

Observers 13° and 26° below the plane of the rotors have M_r values of 0.86 and 0.85, respectively. The observer 13° below the rotor plane has the largest peak out of any observer for this segment. The observers 39° and 52° below the rotor plane have M_r values of 0.83 and 0.79, respectively. Thickness noise dominates the signal in the plane of the rotor, especially for high-tip-speed cases. Loading noise becomes more important for observers farther from the plane of the rotor. Because there are no unsteady effects from the wake for this aircraft, the amplitude of the signal is lower and there are no sharp peaks.

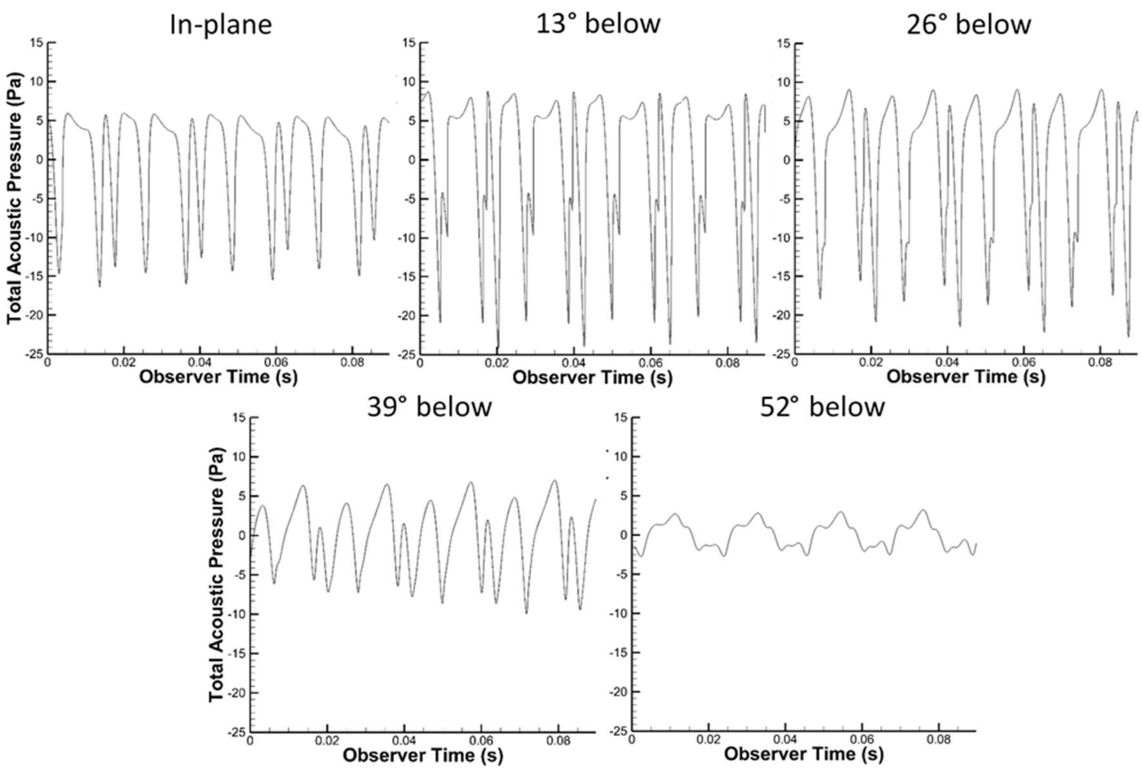

Figure 7.57: Acoustic pressure time history after HSI post-processing for an array of observers in front of the hexacopter in segment 6.

Chapter Summary

This chapter demonstrated the system as a whole. Four NDARC aircraft executed the same mission. These aircraft were not sized for the same mission, so direct comparisons between vehicles are not directly relevant; however, this chapter demonstrated the capability of the NPS to predict noise for multiple NDARC configurations and flight conditions. Each noise source model developed in this project was explored in this mission. Acoustic results were shown for each case. OASPL was plotted for a hemisphere of observers for each case. Acoustic pressure time history was explored to see BVI interactions. BVISPL is used to isolate the BVI incidents on the sphere. Post-processed acoustic pressure time histories were shown for observers in and out of the rotor plane to see the effects of HSI noise.

The results in this chapter demonstrate that each new model implemented into the NPS is compatible with NDARC configurations and can be used to provide acoustic predictions. When examining the results it is clear that more calibration and validation are desired. In the BVI model, there are "scalloped" patterns in the unsteady loading. These are seen in the disk plots, where one BVI event is broken up into smaller bands that have "skips" in them. This pattern is likely numerical and might be solved by adjusting resolutions and refining the method used to model BVI. The "scalloped" pattern may lead to the high frequency "noise" seen in the acoustic pressure time history plots, and may change the overall spectrum and OASPL data. In the HSI model, the relations used for amplifying and shearing should be validated at greater distances. If the signal is over-sheared, the signal may have a significant loss in amplitude. This may be undesirable, and lead to unexpected results. For example, an in-plane observer may be over-sheared, resulting in an amplitude loss. Then, for an observer with a lower M_r value the signal is sheared less, which could lead to a post-processed signal with a larger amplitude (due to less amplitude loss). The values for shearing and distance can be tuned to reduce these effects. Overall, these results demonstrate that the models implemented can be used to predict BVI and HSI effects. Tuning these models in the future could lead to more accurate predictions. These issues are addressed more in-depth in chapter 8.

Blade-vortex interaction was explored for each aircraft by examining the trailing tip-vortices, unsteady disk loading, and BVISPL. It was shown that the helicopter and coaxial configurations experienced strong BVI when operating in 6° descent (segment 3), and that BVI was much less significant when operating in a 1° descent condition (segment 4). The tandem configuration experienced BVI in this segment as well, but at a lesser severity.

Each aircraft was also examined in high-tip-speed cases that are important for HSI. Each rotor was post-processed based on the M_r value for five observers at varying elevation angles in front of the aircraft. The tandem configuration reached the highest tip-Mach number when operating at its maximum flight condition. This aircraft saw the most significant shock fitted signals. The coaxial configuration was affected the least by HSI effects. The signals were shock fit when necessary, but they were amplified and sheared by a lesser degree. Out of plane observers for this vehicle were amplified and sheared by much smaller factors. The hexacopter configuration had a complex pattern due to the signals from six different rotors.

Chapter 8

Concluding Remarks

This project demonstrates a noise prediction system (NPS) that can be used to predict noise for aircraft during conceptual design. While noise is important for rotorcraft missions, it is not often considered in conceptual design aircraft. In order to be consistent with conceptual design, this system was designed with the key goals of speed and accuracy. Simple models for blade loading, BVI, and HSI were implemented into the NPS. These models allow insight into complicated noise sources, while remaining simple enough be executed quickly. This provides a designer with details of acoustic predictions early in the design process without relying on prediction tools that have high computational cost.

The NPS is built using four separate tools to achieve the noise prediction. NDARC is used to provide aircraft and flight data. This tool can be used to size aircraft and study their performance in different mission conditions. The interface tool, WOPIt, performs the bulk of the modeling that is needed for acoustic prediction. WOPIt calculates blade loading, trims the rotor to match the mission specifications, models blade-vortex interactions, and provides all necessary input files to PSU-WOPWOP. WOPIt can also output plots that help the user visualize variables on the rotor disk, and view the trailing tip vortex geometry. PSU-WOPWOP uses the geometry, loading, and input files generated by WOPIt to predict the noise for the aircraft. PSU-WOPWOP is a well-validated tool that is used for its many acoustic prediction models. Finally, ShearIt is used to model HSI noise by post-processing the acoustic results provided by PSU-WOPWOP. The noise prediction system was built to give the user control over what rotors are analyzed, what calculations are performed for these rotors, and what outputs are produced. This is achieved while still maintaining simplicity; the user is not required to know every possible setting that NDARC or PSU-WOPWOP are capable of to execute the system.

The system is designed to predict various noise sources. These sources include loading, thickness, broadband, blade-vortex interaction, and high-speed-impulsive noise. Thickness noise and loading noise are predicted in PSU-WOPWOP using Farassat's formulation 1A. WOPIt provides the necessary geometry and loading. The compact loading and dual-compact thickness noise models are used for loading and thickness noise, respectively. By modeling the blade as a lifting line (or two lifting lines for dual compact thickness noise) there is a significant increase in speed while still maintaining accuracy. Blade element theory is used to calculate the blade loading for loading noise. These models have shown to be accurate and fast. The loading model allows for unsteady interactions to adjust the base loading at any point across the rotor disk. Beddoes wake model is used to calculate the trailing tip-vortex geometry for the rotor. This wake induces a velocity on the blade which is used to model blade-vortex interactions. This distorted, prescribed wake model provides accuracy that is appropriate for the conceptual design process at much lower computational costs than a free wake model. Finally, HSI noise is modeled using an ad hoc, post-processing method. Empirical models are used to amplify, shear, and shock fit the acoustic pressure time history signal for an aircraft.

Summary of Contributions

This project was designed to provide acoustic prediction capabilities for conceptual design aircraft. In 2016 Kalki Sharma designed the noise prediction system to couple NDARC to PSU-WOPWOP [9]. His implementation provided the files required by PSU-WOPWOP, along with the models for loading, thickness, and broadband noise. Sharma also implemented prototypes for HSI and interaction noise. This served as the basis for this project. The major contributions developed for the NPS are outlined below.

The blade loading model included by Sharma did not have high enough resolution and was not compatible with the unsteady loading required to predict BVI noise. The blade loading model was replaced with a blade element theory model. This model calculates the differential forces acting at each blade station for every azimuth station. The resulting forces are calculated by integrating the values over the discretized rotor disk. A trim model was implemented to ensure that the thrust and moments for each rotor match the information provided by NDARC.

Blade-vortex-interaction noise is an important noise source that was not included in the original NPS. Sharma recommended that BVI effects could be added in the future to make the NPS more accurate. Ignoring the effects of BVI can lead to a significant under-prediction of the noise output. A model was implemented to track the tip-vortex geometry that trails behind the rotor. BVI noise is modeled by adjusting the blade loading due to unsteady effects caused by the wake. This important addition expanded the prediction capabilities of the NPS.

HSI modeling was prototyped by Sharma. The same post-processing method of amplifying, shearing, and shock fitting was proposed. This prototype was external to the NPS, and only worked for a single rotor for observers in the plane of that rotor. The HSI model was completely replaced and built into the NPS. This implementation of the HSI model allows for acoustic prediction for any observer location, with more robust empirical equations that depend on the Mach number in the radiation direction of the observer to amplify and shear the signal accordingly. ShearIt post-processes the signal for each individual rotor before combining the signals into one file. WOPIt now generates all of the input files needed for PSU-WOPWOP to read in the post-processed signals to provide further acoustic prediction.

Recommendation for Future Work

This section explains the limitations of the system and proposes work that could be completed in the future to expand the usefulness of the NPS. Limited validation for this project was completed for each model as they were developed. However, more validation could be useful to determine the scope in which these models are valid, and find any important limitations of the system. This is especially true for the BVI and HSI models. Comparison with experimental data would be useful. These models could be adjusted as necessary depending on the validation results. More configurations and flight conditions could also be tested in the future as well. These comparisons would be beneficial to the overall usefulness of the NPS.

Blade-Vortex Interaction

The BVI model uses Beddoes wake model [33] to map the tip vortices that trail behind the rotor. Comparison of the resulting tip-vortex geometry with wakes from experiments, or other prescribed wake models would help further tune the parameters that change the wake shape. The z-location of the tip vortex geometry once passed the rotor disk is important, especially if modeling interactions between blades. When inducing a velocity on the blades, and calculating unsteady loading in some conditions, there are “scalloped” patterns in the loading. The jittery nature of these plots look numerical rather than physical, and may lead to changes in the acoustic prediction. These patterns may be able to be addressed by changing resolution ratios, and or modifying the BVI models slightly.

Unsteady Interactions

This project introduced blade-vortex-interaction noise capabilities to the noise prediction system. Currently, the system predicts the noise results for a rotor operating in its own wake. However, this should be expanded to include interactions for configurations that have multiple rotors that could influence each other. The models that are already used to predict the induced velocity on the rotor disk could be used to adjust another rotor's loading. However, currently the wake geometry is not influenced by other aircraft components. A model would need to be implemented and validated to achieve the correct distortion to wake geometry. This model would allow the NPS to calculate rotor-rotor interaction effects. Depending on the configuration, these could be very prevalent in many varying flight conditions.

Other components that are upstream of a rotor can also cause significant unsteady interactions. Both lifting and non-lifting aircraft components can influence a rotor's performance. Examples of upstream interaction include propellers mounted on wings, tail rotors operating in the wake of the fuselage, or a rotor operating in the wake of a strut. All of these could cause a velocity deficit that create unsteady blade loading. This project proposes a method to account for these interactions. If the geometry of a component is known in NDARC, WOPIt could project a "region of influence" in the direction opposite of the flight direction. As blades enter this region the blade loads can be adjusted at the corresponding stations of the discretized rotor disk in an identical manner to the BVI model. Data on how this region shrinks or expands as it propagates backwards would be needed to correctly implement this model. The strength of the velocity deficit imposed on the downstream rotor would also need to be calibrated. Implementing the capability to predict aerodynamic interaction noise for any general configuration would be beneficial to the NPS.

HSI Noise

The high-speed-impulsive noise model was reworked and implemented into the NPS. While this allows the user to predict HSI noise for any configuration at any observer position, it still has its limitations as a post-processing algorithm. Ultimately, the capabilities of ShearIt should be implemented into PSU-WOPWOP. This would simplify the NPS algorithm and cut down on the total number of input files that are passed around by the individual programs. Currently ShearIt runs after PSU-WOPWOP and then if further acoustic prediction is desired PSU-WOPWOP is executed after ShearIt to read in the post-processed files. If these capabilities were inside PSU-WOPWOP, there would be no need for these extra steps. To incorporate ShearIt in the NPS, slight modifications to PSU-WOPWOP were made. These changes did not affect any of the acoustic models, or change any capabilities of the program. This change allows PSU-WOPWOP to add M_r and r_{obs} to rotor namelists (created by WOPIt) that are used in ShearIt. While this change is not significant, it is worth noting that to use the HSI model, a specific version of PSU-WOPWOP is required. Obviously this requirement would no longer be relevant if ShearIt was added to PSU-WOPWOP.

Adding ShearIt into PSU-WOPWOP would also expand the acoustic prediction capabilities of the system. Currently, ShearIt reads the acoustic pressure time history that is generated for a single observer in PSU-WOPWOP and applies the post-processing to that signal. However if it were implemented into PSU-WOPWOP, acoustic results could be computed for any number of observers. This would allow plots like the hemispherical OASPL plots used in chapter 7 to be produced for an HSI case. Implementation into PSU-WOPWOP would expand the prediction capabilities, simplify the algorithm, and cut down on total computation time.

The HSI model uses empirical method to scale and shear the signal. The scaling and shearing algorithms were created by comparing results with CFD data from Baeder et al. The CFD mesh was designed to focus in the plane of the rotor, and was coarser out-of-plane. Comparison with other models could provide important validation for these empirical models. Data from Baeder et al. was taken at 3.09 rotor radii away from the blades. The empirical models may be different in the acoustic far-field, so this could be addressed.

The shearing algorithm is dependent on both M_r and radiation distance. This mimics nonlinear propagation so that over a large enough distance a signal will shock even at lower tip Mach numbers. Data on the shock-formation distance of a general wave could be explored to make the empirical model more accurate. The distance effects applied to shearing the signal in this model could be adjusted based on these validation comparisons. If a signal is over-sheared, there is a loss in amplitude. If this loss in amplitude is too great, it may lead to some results that are not consistent with the data that was used to calibrate the model. When the shearing angle is so high that there is significant amplitude loss, an observer with a smaller M_r value may have a larger amplitude. Tuning the shearing relation (especially with radiation distance) may lead to more robust results.

Once HSI capabilities are introduced into PSU-WOPWOP, the effects of atmospheric attenuation can be applied to the signal. As the pressure wave propagates the amplitude decreases. This opposes the shearing effects that occur over long distances. These results could be explored for observers at long range.

References

[1] Leishman, J. G., *Principles of Helicopter Aerodynamics*. New York, NY: Cambridge University Press. 2010.

[2] "Helicopter Rotor Systems Configuration - SKYbrary Aviation Safety." *Skybrary*, 16 June 2018. Retrieved from www.skybrary.aero/index.php/Helicopter_Rotor_Systems_Configuration#Tandem_rotor_.28or_dual_rotor.29 (accessed 11/9/2020).

[3] Uber, "Uber Elevate: Fast-Forwarding to a Future of On-Demand Urban Air Transportation," Uber, 2016 https://www.uber.com/elevate.pdf.

[4] Brentner, K. S., and Farassat, F., "Modeling aerodynamically generated sound of helicopter rotors," *Progress in Aerospace Sciences*, Vol. 39, No. 2-3, pp. 83-120, February 2003.

[5] Fly Neighborly Guide. 3rd Edition. Helicopter Association International. Retrieved from http://www.aia.org.nz/site/aianz/files/Aircare/Fly% 20Neighbourly%20Guide.pdf (accessed 11/9/2020).

[6] "Lawmakers Cite Noise, Emissions in Bid to Ban Helicopters over NYC." *Evtol.Com*, MHM Publishing, 27 Oct. 2019. retrieved from evtol.com/news/lawmakers-cite-noise-emissions-nyc-helicopter-ban/ (accessed 11/9/2020).

[7] Sarsfield, K. "London Moves to Clamp down on Helicopter Noise after Local Government Report Slams Rotary Wing Nuisance." *FlightGlobal*, DVV Media International Ltd, 7 Nov. 2006. (accessed 11/9/2020).

[8] Sharma, K., and Brentner, K.S., "Acoustic Assessment for Design and Analysis of Rotorcraft," Proceedings of the AHS 72nd Annual Forum, West Palm Beach, FL, May 17, 2016.

[9] Sharma, K. *Incorporating Acoustic Assessment into the Design and Analysis of Rotorcraft*. M.S. Thesis, Department of Aerospace Engineering, The Pennsylvania State University, 2016.

[10] Johnson, W., *NDARC NASA Design and Analysis of Rotorcraft Theory Release 1.15*, NASA Ames Research Center, Moffen Field, CA, October 2020.

[11] Hennes, C.C, Lopes, L.V., Shirey, J., Cheng, R., Erwin, J., Lee, S., Goldman, B.A., Botre, M., and Brentner, K.S., PSU-WOPWOP 3.4.3 User's Guide, The Pennsylvania State University, University Park PA, May 12, 2020

[12] M.J. Lighthill. "On Sound Generated Aerodynamically, I: General Theory". In: *Proceedings of the Royal Society* A211 (1952), pp. 564–587.

[13] S. N. Curle. "The influence of solid boundaries upon aerodynamic sound". *Proceedings of the Royal Society* A231 (1955), pp. 505–514.

[14] J. E. Ffowcs Williams and D. L. Hawkings. "Sound generation by turbulence and surfaces in arbitrary motion". In: *Philosophical Transactions of the Royal Society of London. Series A, Mathematical and Physical Sciences* 264.1151 (May 1969), pp. 321–342.

[15] Farassat, F. and Succi, G. P., "The Prediction of Helicopter Discrete Frequency Noise," Vertica, 1983; 7(4):309-320.

[16] Farassat, F. The sound from rigid bodies in arbitrary motion, Ph.D. thesis, Cornell University, 1973.

[17] Farassat, F. Theory of noise generation from moving bodies with an application to helicopter rotors, NASA TR R-451, 1975.

[18] Farassat F, Pegg RJ, Hilton DA. Thickness noise of helicopter rotors at high tip speeds, AIAA Paper 75-453, 1975.

[19] Farassat, F., Morris, C. E. K., and Nystrom, P. A., "A comparison of linear acoustic theory with experimental noise data for a small-scale hovering rotor", in *American Institute of Aeronautics and Astronautics Conference,* 1979.

[20] Currie, I.G. *Fundamental Mechanics of Fluids*. 4th ed., Boca Raton, FL, Crc Press, Taylor and Francis Group, 2013.

[21] Greenwood, E., *Fundamental Rotorcraft Acoustic Modeling from Experiments (FRAME)*. PhD thesis. Department of Aerospace Engineering, University of Maryland, 2011.

[22] Brentner, K.S. An Efficient and Robust Method for Predicting Helicopter Rotor High-Speed Impulsive Noise. *Journal of Sound and Vibration,* Vol. 203, No. 1, pp. 87-100, May 29 1997.

[23] Brooks, T. F., Burley, C. L., "Rotor Broadband Noise Prediction with Comparison to Model Data," *Journal of the American Helicopter Society*, Vol. 49, No. 1, January 2004.

[24] Kinsler, L., Frey, A., Coppens, A., and Sanfers, J., *Fundamentals of Acoustics*. 4th ed., New York, John Wiley & Sons, 2000.

[25] Casper J., Farassat F., A New Time Domain Formulation for Broadband Noise Predictions. *International Journal of Aeroacoustics*, pp. 207-240, 2002.

[26] Pegg, R. J., "A Summary and Evaluation of Semi-Empirical Methods for the Prediction of Helicopter Rotor Noise," NASA Technical Memorandum 80200, December 1979.

[27] Brès, G.A., Brentner, K.S., Perez, G., and Jones, H.E.: Maneuvering Rotorcraft Noise Prediction. *Journal of Sound and Vibration*, Vol. 275, No.3-5, August 2003, pp. 719-738.

[28] Yang, T., Brentner, K. S., & Walsh, G. D., "A Dual Compact Model for Rotor Thickness Noise Prediction," *Journal of the American Helicopter Society*, 63(1), 12 pages. DOI: 10.4050/JAHS.63.022000, 2018.

[29] Snider, R., Samuels, T., Goldman, B., Brentner, K., "Full-Scale Rotorcraft Broadband Prediction and its Relevance to Civil Noise Certification Criteria," Presented at the American Helicopter Society 69th Annual Forum, Phoenix, Arizona, May 21-23, 2013, 15 pages.

[30] Baeder, J.D., Gallman, J.M., and Yu, Y.H., "A Computational Study of the Aeroacoustics of Rotors in Hover." Presented at the American Helicopter Society 49th Annual Forum, St. Louis, Missouri, May 19-21, 1993.

[31] Yaakub, M.F., Wahab, A.A., Abdulluah, A., Nik Mohn, N.A.R., and Shamsuddin, S.S., "Aerodynamic Prediction of Helicopter Rotor in Forward Flight Using Blade Element Theory." *Journal of Mechanical Engineering and Sciences*, vol. 11, no. 2, June 2017, pp. 2711–2722.

[32] Prouty, R.W. *Helicopter Performance, Stability, and Control*. Krieger Pub., PWS Engineering Boston, 2005.

[33] Beddoes, T.S., "A Wake Model for High Resolution Airloads," in International Conference on Rotorcraft Basic Research, (Research Triangle Park, NC), February 1985.

[34] B. G. van der Wall, "The effect of HHC on the vortex convection in the wake of a helicopter rotor," *Aerospace Science and Technology*, vol. 4, no. 5, pp. 321–336, 2000.

[35] J. M. Drees, "A theory of airflow through rotors and its application to some helicopter problems," *Journal of Helicopter Association of Great Britain*, vol. 3, no. 2, 1949.

[36] A. J. Landgrebe, "The wake geometry of a hovering helicopter rotor and its influence on rotor performance," *Journal of the American Helicopter Society*, vol. 17, no. 4, 1972.

[37] *Fluids 3-D Vortex Filaments*. Massachusetts Institute of Technology, 2008 (accessed 11/9/2020).

[38] Sickenberger, R. *Modeling Helicopter Near-Horizon Harmonic Noise Due to Transient Maneuvers*. PhD thesis. Department of Aerospace Engineering, University of Maryland, 2013

[39] Vatistas, G.H., Kozel, V., and Mih, W.C., "A Simpler Model for Concentrated Vortices." *Experiments in Fluids*, vol. 11, no. 1, 1 Apr. 1991.

[40] Katopodes, Nikolaos D. Chapter 7 - Vorticity Dynamics. edited by Nikolaos D Katopodes, Butterworth-Heinemann, 2019, pp. 516–565.

[41] L.A. Young, "Vortex core size in the rotor near wake," NASA TM-2003- 212275, 2003.

[42] Lim, J.W., Tung, C., Yu, Y.H., Burley, C.L., Brooks, T., Boyd, D., van der Waal, B., Schneider, O., Richard, H., Raffel, M., Beaumier, P., Bailly, J., Delrieux, Y., Pengel, K., and Mercker, E., "HART-II: Prediction of Blade-Vortex Interaction Loading." *29th European Rotorcraft Forum*, Friedrichshafen, Germany, Sept. 2003.

[43] Schmitz, F.H., Chapter 2: Rotor Noise, in Aeroacoustics of Flight Vehicles: Theory and Practice. edited by Hubbard, H.H., vol. 1: Noise Sources, NASA Reference Publication 1258, Aug. 1991.

[44] Whitham, G. B., *Linear and Nonlinear Waves*, New York, NY: Wiley-Interscience, 1974.

[45] Johnson, W., "NDARC-NASA Design and Analysis of Rotorcraft Validation and Demonstration," American Helicopter Society Aeromechanics Specialists' Conference, San Francisco, CA, January 20-22, 2010.

[46] Burley, C.L., and R.M. Martin. "Tip-Path-Plane Angle Effects on Rotor Blade-Vortex Interaction Noise Levels and Directivity." Presented at the 44th Annual Forum of the American Helicopter Society, Washington D.C., June 1988.